

OPTICAL TRACKING AND SPECTRAL  
CHARACTERIZATION OF CUBESATS FOR OPERATIONAL  
MISSIONS

by  
Forrest Gasdia

A Thesis Submitted to the College of Arts and Sciences  
Physical Sciences Department  
in Partial Fulfillment of the Requirements for the Degree of  
Master of Science in Engineering Physics

Embry-Riddle Aeronautical University  
Daytona Beach, Florida  
May 2016

© Copyright 2016  
Forrest Gasdia

All Rights Reserved

**OPTICAL TRACKING AND SPECTRAL CHARACTERIZATION OF CUBESATS FOR  
OPERATIONAL MISSIONS**

by  
Forrest Gasdia

This thesis was prepared under the direction of the candidate's Thesis Committee Chair, Dr. Aroh Barjatya, and has been approved by the members of the thesis committee. It was submitted to the Department of Physical Sciences, Daytona Beach campus, and was accepted in partial fulfillment of the requirements for the degree of Master of Science in Engineering Physics.

**Thesis Review Committee:**

---

Dr. Aroh Barjatya  
Committee Chair

---

Dr. Ted von Hippel  
Committee Member

---

Dr. Jason Aufdenberg  
Committee Member

---

Dr. Alan Liu  
MSEP Graduate Program Coordinator

---

Dr. Terry Oswalt  
Department Chair, Physical Sciences

---

Dr. William Grams  
Dean, College of Arts & Sciences

---

Dr. Chris Grant  
Vice Chancellor, Academic Support

April, 2016

## Abstract

Orbital debris in low Earth orbit is of growing concern to operational satellites from the government and commercial sector. With an uptick in worldwide satellite launches and the growing adoption of the CubeSat standard, the number of small objects in orbit are increasing at a faster pace than ever. As a result, a cascading collision event seems inevitable in the near future.

The United States Strategic Command tracks and determines the orbit of resident space objects using a worldwide network of radar and optical sensors. However, in order to better protect space assets, there has been increased interest in not just knowing *where* a space object is, but *what* the object is. The optical and spectral characteristics of solar light reflected off of satellites or debris can provide information on the physical state or identity of the object. These same optical signatures can be used for mission support of operational satellite missions—down to satellites as small as CubeSats. Optical observation of CubeSats could provide independent monitoring of spin rate, deployable status, identification of individual CubeSats in a swarm, or possibly attitude information.

This thesis first introduces the reader to a review of available observation techniques followed by the basics of observational astronomy relevant to satellite tracking. The thesis then presents the OSCOM system—a system for Optical tracking and Spectral characterization of CubeSats for Operational Missions. OSCOM is a ground-based system capable of observing and characterizing small debris and CubeSats with commercially available optical telescopes and detectors. The system is just as applicable for larger satellites which have higher signal to noise ratio. The OSCOM system has been used to successfully collect time-series photometry of more than 60 unique satellites of all sizes. Selected photometry results are presented along with a discussion of the technical details required for optical observation of small satellites.

## Acknowledgements

Foremost, I would like to thank my thesis advisor, Dr. Aroh Barjatya, for his enthusiasm and support of the creation of OSCOM. I would also like to thank my thesis committee members Dr. Ted von Hippel and Dr. Jason Aufdenberg for their insight and guidance throughout my design of a satellite tracking system and in the writing of this thesis. Finally, I thank Sergei Bilardi for his assistance with several OSCOM observations and for testing a portion of the osat Python package.

This work was partially supported by NSF RAPID (#AGS-1450999) and ERAU Spark funding. It builds upon the ERAU Internal Student Research Award *An Aerospace Tracking System for Embry-Riddle's Astronomical Telescopes* (2013–2014).

# Contents

<b>List of Figures</b>	<b>viii</b>
<b>1 Introduction</b>	<b>1</b>
1.1 Review of Satellite Observation Techniques . . . . .	3
1.2 OSCOM's Role . . . . .	10
1.3 Thesis Overview . . . . .	13
<b>2 Satellite Visibility Basics</b>	<b>14</b>
2.1 The Magnitude System . . . . .	16
2.2 Estimating Satellite Brightness . . . . .	17
2.3 Satellite Color . . . . .	27
<b>3 OSCOM Design Overview</b>	<b>29</b>
3.1 Signal Flow . . . . .	29
3.2 Tracking System . . . . .	36
3.3 Tracking Logic and Control . . . . .	41
<b>4 Instrumentation</b>	<b>49</b>
4.1 Telescopes . . . . .	49
4.2 Detectors . . . . .	59
4.3 Electro-Optics for Satellite Observation . . . . .	65
4.4 Optical filters . . . . .	75

4.5	Telescope Mounts . . . . .	77
<b>5</b>	<b>Data Reduction and Analysis</b>	<b>82</b>
5.1	Image Reduction . . . . .	82
5.2	Photometry . . . . .	85
5.3	Photometry Corrections . . . . .	90
5.4	Photometry Analysis . . . . .	94
5.5	Processing Resolved Images . . . . .	98
<b>6</b>	<b>Observations</b>	<b>101</b>
6.1	Large Satellites . . . . .	102
6.2	Small Satellites . . . . .	108
6.3	Microsatellites . . . . .	110
6.4	Nanosatellites and CubeSats . . . . .	114
<b>7</b>	<b>Future Efforts and Conclusions</b>	<b>123</b>
	<b>Bibliography</b>	<b>125</b>

# List of Figures

1.1	Mount track modes	5
1.2	Baker Nunn camera	6
1.3	Falcon Telescope	9
1.4	Celestron RASA	10
2.1	Satellite visibility	15
2.2	Solar phase angle	18
2.3	Satellite illumination geometry	19
2.4	Diffuse and specular reflection	21
2.5	SpinSat R band	22
2.6	Phase functions	23
2.7	Cube facets	24
2.8	Satellite magnitude vs. area	25
2.9	Phase angle bisector	26
3.1	Signal flow	30
3.2	Airmass	32
3.3	POPACS-2 image	34
3.4	Tracking setups	37
3.5	Tracking process	39
3.6	Mount calibration	45

3.7	Pixel grid . . . . .	46
4.1	Telescope optics . . . . .	51
4.2	Airy disk . . . . .	56
4.3	MTF . . . . .	58
4.4	Telescope types . . . . .	59
4.5	Manta G-235 gain curve . . . . .	63
4.6	QE curve . . . . .	64
4.7	EO system design drivers . . . . .	69
4.8	RASA optical design . . . . .	71
4.9	FOV comparison . . . . .	72
4.10	1 m DFM telescope . . . . .	74
4.11	Filter transmission curves . . . . .	76
4.12	Satellite rates . . . . .	78
4.13	Mount types . . . . .	80
5.1	Dark frame . . . . .	83
5.2	Flat field . . . . .	85
5.3	Photometric aperture . . . . .	86
5.4	Image segmentation . . . . .	88
5.5	Background map extraction . . . . .	89
5.6	OPAL photometric corrections . . . . .	93
5.7	OPAL az/el and range . . . . .	93
5.8	Light curve filtering . . . . .	96
5.9	MAD rejection criteria . . . . .	96
5.10	DICE-2 noisy light curve . . . . .	98
5.11	DICE-2 periodogram . . . . .	99
5.12	ISS deconvolution . . . . .	100

6.1	DMSP-5D2 F7 . . . . .	103
6.2	DMSP-5D2 F12 . . . . .	103
6.5	Hitomi . . . . .	105
6.7	Hitomi deb L . . . . .	106
6.13	KMS 3-2 . . . . .	109
6.14	OPAL . . . . .	111
6.15	DANDE . . . . .	112
6.17	SpinSat . . . . .	113
6.19	AISSat-2 . . . . .	115
6.21	CanX-3a . . . . .	116
6.22	DICE-1 . . . . .	117
6.26	POPACS-1 . . . . .	119
6.28	POPACS-2 . . . . .	120
6.31	POPACS-3 . . . . .	121

# Chapter 1

## Introduction

The United States Strategic Command Joint Space Operations Center (JSpOC), charged with tracking satellites and debris in Earth orbit, currently monitors more than 17,500 objects [JSpOC, 2016]. Of these objects, about 16,000 are debris from launches or broken and damaged satellites, over 1300 are operational satellites, and a growing number fall somewhere in between these categories—CubeSats [Swartwout, 2014; UCS, 2015]. To keep track of the orbits of all of these resident space objects (RSOs) and watch for potential collisions between them, JSpOC commands the worldwide Space Surveillance Network (SSN) of 30 radar and optical observatories to make several hundred thousand spot observations daily [USSTRATCOM, 2014]. These spot observations provide orbit predictions for most satellite operators, but the current system has difficulty tracking satellites in the 10 cm size range or smaller and does little to characterize them. Additionally, the number of objects that need to be tracked limit the availability of the system to observe small, low-priority satellites.

CubeSats are a unique class of satellite that often have older or less accurate orbital elements than large commercial satellites. They are nanosatellites with a standardized form factor originated by Professor Robert Twiggs of the Department of Aeronautics and Astronautics at Stanford University and further developed by Professor Jordi Puig-

Suari by Cal Poly in San Luis Obispo [CubeSat, 2016]. CubeSats are measured in “units” or U where a 1U CubeSat is a 10 cm cube, plus the length of any antennae or instruments that may be deployed on orbit. Their mass must be no more than 1.33 kg. CubeSats may be made larger by stacking 1U sections, e.g. a 3U CubeSat has dimensions of  $10 \times 10 \times 30$  cm. By utilizing a common form factor, CubeSat projects can deploy their satellites using standardized deployment mechanisms such as the Poly Picosatellite Orbital Deployer (P-POD), the NanoRacks CubeSat Deployer, or other devices [NanoRacks, 2013; The CubeSat Program, 2014]. These deployers allow CubeSats to be deployed from the International Space Station or launch vehicles such as the Atlas V where CubeSats ride as secondary payloads alongside a larger satellite. Because of their small size, relatively low launch costs, and rapid development cycle, CubeSats are especially popular projects for universities looking to develop new space technology or deploy instruments for the in situ observation of the near-Earth space environment or other studies. Given the demonstrated potential of CubeSats as a tool for testing new technology at low cost, an increasing number of CubeSat launches have been by government or commercial operators, who made up 80% of CubeSat launches in 2015 [Swartwout, 2016].

Despite their potential for success, nearly 50% of CubeSats have had mission failure with primary causes being no contact or power or communication loss [Swartwout, 2013]. Failure is especially common among universities and first-time CubeSat designers—a group that remains large as new universities around the globe compete for CubeSat funding and launch spots yearly. After failure, CubeSats endanger other satellites that we rely on in daily life<sup>1</sup>. Their small size makes consistent and accurate orbit determination by the SSN a difficult task, and CubeSat operators often have little knowledge of what systems have failed or what the cause of failure was. These CubeSats and the thousands of pieces of debris in orbit make up the current Space Situational

---

<sup>1</sup>Small, uncontrolled “beep sats” that perform only very basic functions such as transmitting an identification in Morse code are also often considered debris by large satellite operators, even if they are technically functional. More generally, the inability of most CubeSats to maneuver in space makes them a liability for collisions.

Awareness (SSA) issue.

This thesis details the creation of the OSCOM system, which provides Optical tracking and Spectral characterization of CubeSats for Operational Mission support. OSCOM addresses several components to solving the SSA problem, including electro-optics and tracking, reduction, and analysis of spatial and photometric data, but it specializes in the targeted optical observation and characterization of CubeSats and other small satellites. These observations provide independent verification of spacecraft operation and help identify unknown RSOs. Much work has been conducted to optically observe satellites since the beginning of the space program, so this introduction will review previous work and discuss how OSCOM satellite observations can aid satellite missions.

## 1.1 Review of Satellite Observation Techniques

Before Sputnik had even launched, people were thinking about how satellites could be observed from the ground. As early as 1954, O'Keefe suggested covering satellites with retro-reflectors and illuminating them using spotlights [O'Keefe, 1955], while others imagined satellites could carry bright strobe lights into orbit [Veis, 1963]. Additional work estimated the expected intensity of reflected sunlight from satellites to observers on earth [Zirker, Whipple, & Davis, 1956] and showed that although the intensity varied greatly with the size of the satellite, many would be visible by eye. The launch of Sputnik-1 in 1957 proved that even a half-meter polished sphere in low Earth orbit would be visible to the naked eye, although just only, being at around magnitude five<sup>2</sup> (see section 2.1 for an explanation of the magnitude system).

The late 1950s and 1960s brought a tremendous effort by the US military, civilian scientists, and even amateurs participating in the Project Moonwatch program to develop tracking systems and record observations of artificial satellites for precision orbit

---

<sup>2</sup>Many casual observers trying to glimpse Earth's first artificial satellite likely saw the first magnitude 26 m long upper stage rocket that brought Sputnik to orbit rather than the satellite itself [NSSDCA, 2016].

determination [Whipple & Hynek, 1958]. As early as January 1960, Hoffmann, Krotkov, and Dicke published a paper [Hoffmann et al., 1960] discussing the instrumentation requirements for precision optical tracking of artificial satellites that might allow the detection of minute variations in Earth's gravitational field. However, it was George Veis's 47-page paper "Optical tracking of artificial satellites" that provided a complete outline of optical satellite tracking up to that time [Veis, 1963].

## Tracking modes

Included in "Optical tracking of artificial satellites" is a discussion of the three common modes of photographic satellite tracking: recording with the telescope in a fixed staring mode, with the telescope mount moving at sidereal rate, or with the telescope tracking at the satellite rate. Each of these modes provide unique advantages and disadvantages, as shown in Figure 1.1. The staring mode is very simple to implement because the telescope mount is fixed, but both background stars and the satellite will trail across the focal plane array for the duration of the exposure. A staring mode is useful for geostationary satellites, however, because they have a roughly fixed position in the sky. The second mode, moving at sidereal rate, is also commonly achievable because nearly all astronomical telescope mounts are capable of moving at this rate, which compensates for Earth's rotation. Although this allows the detection of dimmer background stars, satellites will be trailed across the image. Finally, the satellite rate track mode allows detection of dimmer satellites than the other modes, but may require a special telescope control system or a priori knowledge on the orbit of the satellite. Pointing the telescope to a geostationary satellite and turning the mount track rates to 0 is effectively the rate track mode for geostationary satellites.

Veis also reviews several camera systems that operate in each of the track modes. The Ballistic Camera BC-4 uses a 117 mm aperture lens with a 215 × 190 mm glass plate providing a  $30^\circ \times 50^\circ$  field of view and is used in a staring mode. The larger Astrogeodetic

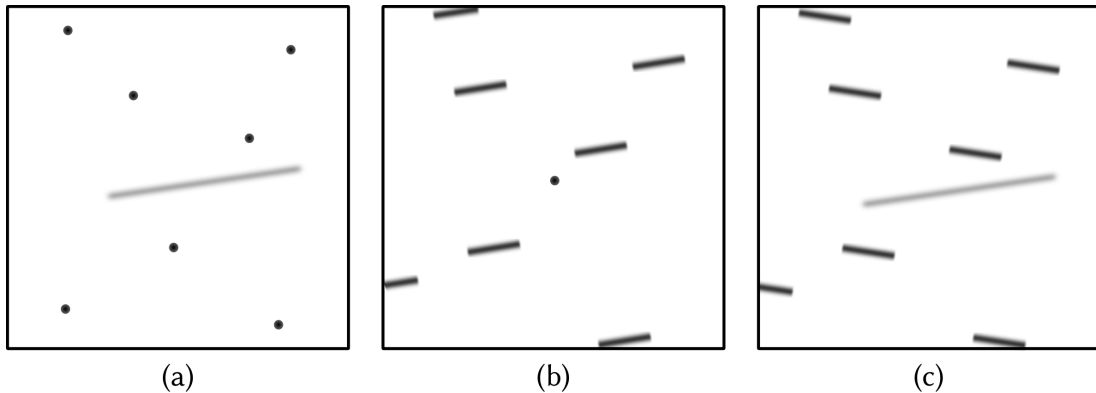


**Figure 1.1:** Satellites and background stars appear different depending on the track mode of the telescope mount. Image (a) demonstrates a mount tracking at sidereal rate so that the satellite forms a streak over the exposure. Image (b) shows either a geostationary satellite with the mount motors off or a satellite with the telescope mount tracking it across the sky in a rate track mode. A mount in a fixed staring mode would see both background stars and the satellite trail across the image, as shown in (c).

Stellar Camera PC-1000 is a modified aerial reconnaissance camera on an azimuth-elevation mounting, also used as a staring camera. It has an 8 inch aperture, but higher focal ratio, so that it only provides a  $10^\circ \times 10^\circ$  field of view with the same size plate. Although glass plates lack the quantum efficiency of modern semiconductor detectors, they could be easily made in large sizes, producing a very large field of view. Choice of modern detectors for satellite observation will be discussed in section 4.2.

The best known tracking camera discussed by Veis is the Baker-Nunn Camera, which was purpose designed for satellite observation (shown in Figure 1.2). The 0.5 m  $f/1$  optic produces a curved focal surface where a strip of film is stretched. This instrument is capable of photographing 14.5 mag stars in a 20 s exposure [Veis, 1963]; a specification that is now beat by more sensitive detectors. Nonetheless, the Baker-Nunn Cameras were deployed as a global network by the Smithsonian Astrophysical Observatory and provided satellite orbit determination and geodetic science into the mid-1970s.

After the invention of the laser in 1960, it did not take long for satellite observers to implement active optical observation techniques. In 1964, Snyder, Hurst, Grafinger, and Halsey reported on laser ranging observations of the Beacon Explorer B satellite



**Figure 1.2:** The Baker Nunn camera for satellite tracking with Joseph Nunn and manufacturers Clyde Chivens and Harry Boller. FROM BOLLER AND CHIVENS [2011].

with NASA Goddard Space Flight Center [Snyder et al., 1965]. The tracking method was primitive; the telescope was pointed at locations predicted by the satellite ephemeris at one minute intervals and the laser was manually fired when the satellite passed through the cross hairs of a sighting telescope. Despite the simplicity, laser signal returns from the satellite were measured and the technique was later refined to achieve high precision orbit determination and geodetics. Although laser ranging is not possible at many small observatories because of safety concerns and lack of necessary equipment, the International Laser Ranging Service<sup>3</sup> operates a network of satellite laser ranging observatories capable of centimeter accuracy orbit determination. Precision spin rates are similarly possible, but both measurements are usually only performed on satellites designed to reflect laser pulses.

Also beginning in 1964, the United States Air Force began investigating the use of reflected light to determine a satellite's physical or dynamic characteristics. Previ-

---

<sup>3</sup><http://ilrs.gsfc.nasa.gov/>

ously, nearly all observations had been concerned with orbit determination. Lambert [1971] described the development of equipment and procedures to measure the reflectance spectra of orbiting spacecraft with the Air Force Aerospace Research Lab's satellite tracking telescope. Lambert showed that the reflectance spectra produced using a low resolution scanning spectrometer could be used to identify the presence of aluminum and white paint. That two of the satellites were of Soviet and Chinese origin also demonstrated the capability of passive satellite observation for identifying unknown resident space objects.

By the year 2000, Air Force Research Laboratory (AFRL) and Boeing, Rocketdyne Technical Services demonstrated the feasibility of using small aperture commercial-off-the-shelf (COTS) telescopes and detectors for asteroid and satellite surveillance [P. W. Kervin et al., 1998]. Sensor and computer technology had increased sufficiently to allow an inexpensive, rapidly deployed system with the sensitivity and capability to track and observe satellites. Such a system, usually employing telescopes of between 12 and 16 inch aperture, is known as a Raven system. Raven is not a specific collection of components, but a design paradigm that leverages tools available to the amateur astronomer [Sydney et al., 2000]. Often, a Raven system consists of a standalone telescope, detector, dome, and control system to obtain and reduce data remotely. These versatile systems continue to be deployed in up-to-date variations because of the ease with which they can be purchased and assembled.

Raven-class telescopes have proven their capability in many observation campaigns. Linares et al. [2013] used the Raven telescope at Los Alamos National Laboratory to successfully verify a shape estimation scheme based on photometry of low orbiting rocket bodies. Raven systems have also been deployed to study satellites in geostationary orbits that had exhibited anomalies or other changes [Tamara E Payne et al., 2007; Paul Kervin, Hall, Toth, & Lambert, 2014].

A somewhat improved version of the Raven system using a larger 0.5 m telescope

was created by engineers at RC Optical Systems (RCOS) [Azari & Ehrhorn, 2007]. Although this system used COTS CCD imagers and a COTS acquisition telescope, the RC Optical Systems elevation over azimuth (EL/AZ) tracking mount provided improved tracking performance over the Raven systems. Additionally, the use of the automated acquisition camera allowed RCOS to initiate open loop tracking but then begin offset guiding to put the satellite in the center of the main imaging array. In order to improve the imaging cadence, the RCOS system sub-framed the detector readout on the satellite position and used the high accuracy of the mount pointing model to refine the orbital elements of each satellite tracked.

Shortly afterwards, Graff [2010] presented a thesis describing a similar closed-loop control system for the Air Force Institute of Technology's COTS Satellite Tracking Telescope. Graff recognized that actively tracking with a closed-loop controller would allow tracking of satellites that deviated from their published TLEs. This was especially important given the small field of view of their 10 inch Schmidt-Cassegrain telescope.

Spurred by the increasing Space Situational Awareness problem, the United States Air Force Academy (USAFA) created a Center for Space Situational Awareness Research (CSSAR), and with it, the Falcon Telescope Network (FTN) [Dearborn, Chun, Liu, & Tippets, 2011]. FTN is a network of 0.5 m telescopes with identical instrumentation clustered in Colorado and with additional sites around the world. Figure 1.3 shows the Falcon Telescope at Otero Junior College in La Junta, Colorado. The network is designed to be a general optical space situational awareness tool used for observation of satellites in low and geosynchronous Earth orbit, and with photometric, spectral, and sometimes polarimetric measurement capabilities. As a telescope *network*, FTN can make multi-site observations to deduce additional information on a satellite's geometry in a single pass, as demonstrated by Hope [2014]. Falcon Telescope Network is also meant to serve as an educational tool and is primarily utilized by students rather than professional researchers.

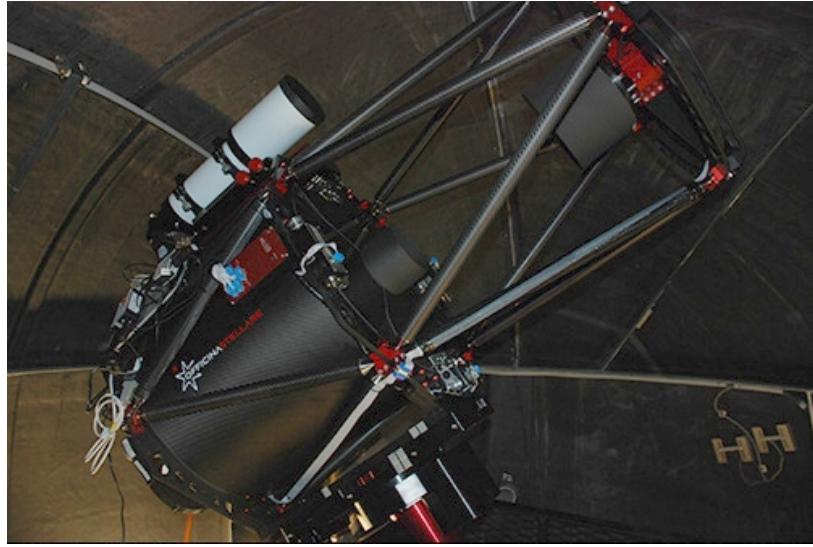


**Figure 1.3:** A typical 0.5 m Falcon Telescope installed at the Otero Junior College node of the Falcon Telescope Network. FROM USAFA CENTER FOR SPACE SITUATIONAL AWARENESS RESEARCH [2013].

Several other universities have also recently begun construction of observatories for satellite observation. Coder and Holzinger [2013] performed a careful analysis to determine which size Raven-class telescope will work well for the Georgia Institute of Technology observatory in Atlanta, Georgia. They concluded that although a telescope with high focal ratio will reduce the impact of bright background skies, the SNR threshold required by the detection algorithm also has a large influence on the overall capability of the system for orbit determination. At Cal Poly San Luis Obispo, Schmalzel [2013] presented a thesis aiming to demonstrate the feasibility of observing small LEO satellites with “amateur” or Raven-class telescopes. Although dozens of satellites were observed as part of that work, only one smallsat, a  $0.6 \times 0.6$  m microsatellite, was successfully tracked. However, by extrapolating TLE accuracy and magnitude predictions to CubeSats, Schmalzel concludes CubeSat observation with amateur equipment may be possible under ideal observing conditions. Lastly, others have begun to experiment with laser ranging techniques using COTS equipment [Hampf, Wagner, & Riede, 2015]. Although this does not allow for high power lasers, which are required for active sensing of small objects, it does offer sufficient power to see echoes from satellites equipped



**Figure 1.4:** The Celestron RASA deployed in the field on an amateur astronomy mount is capable of observing CubeSat sized objects.

with retro-reflectors and possibly large un-cooperative objects.

## 1.2 OSCOM’s Role

The primary goal of OSCOM is to develop and apply a complete solution for targeted optical characterization of individual small satellites and debris in orbit. OSCOM also investigates spatially resolved imaging of large satellites as a secondary goal. Orbit determination is a tertiary goal that will come out of a new photometry technique planned for OSCOM in the future. The requirements for CubeSat photometry are quite different than satellite imaging, and the equipment that OSCOM deploys reflects the needs of specific observations. OSCOM is fortunate to make use of the observatory at Embry-Riddle’s Daytona Beach campus, which has a 1 m, 0.5 m, and smaller telescopes, as well as specialty equipment, including an 11 inch Celestron RASA Schmidt Astrograph, shown in Figure 1.4. Besides the 1 m telescope, entirely COTS optics and detectors are used, which makes the system relatively inexpensive and easy to replicate.

An equally important part of OSCOM is its Python toolset for image reduction and

analysis. By deploying modern and robust photometry and analysis routines, OSCOM seeks to maximize the effectiveness of its COTS equipment. Additionally, the author has learned from experience the importance of using well collimated and focused optics and having a good pointing model for the telescope mount. A successful observer must be familiar with these requirements and more. It is extremely beneficial to understand the characteristics of every individual observatory site and electro-optical system, and this knowledge is only gained through hours of observation on the telescope.

OSCOM differentiates itself from current university-level optical satellite tracking systems in several ways. Perhaps most importantly, the OSCOM system has successfully tracked CubeSats and nanosatellites dozens of times using equipment that can be purchased for under \$10,000. It does so with high enough imaging cadence to resolve photometric fluctuations that occur with as short as 1 s periods. Additionally, OSCOM concentrates on object characterization rather than orbit determination. The role of OSCOM is to observe RSOs with predetermined orbital elements in order to identify the RSO or its operational status. Lastly, OSCOM is successful largely because of its full system approach to this SSA problem. Optical tracking and observation of satellites is a unique domain that blends the fields of spacecraft engineering, electro-optical design, observational astronomy, signal and image processing, and control theory. For successful results, each of these fields has been considered in the design.

### **1.2.1 Cubesat operational missions and SSA**

OSCOM provides data, e.g. lightcurves, that enable two major capabilities. The first uses OSCOM data as an operational mission support tool, especially for small satellites. The second uses OSCOM data for identification of unknown RSOs. As part of realizing these capabilities, it will likely be necessary to catalogue and characterize the optical nature of space objects, including material type and change due to radiation degradation and atomic oxygen in low Earth orbit (LEO). Although OSCOM is currently an enabling

system for this type of research, little of this work has yet to be conducted.

## **Operational Mission Support**

OSCOM creates a unique opportunity for small satellite and CubeSat operators to “get eyes” on their satellite while it’s in orbit. Small satellites send limited information on their status in radio telemetry, and in most failures, this information is never received anyways. As previously mentioned, “no contact”, power, and communications loss made up a total of 79% of CubeSat failures between 2000 and 2012 [Swartwout, 2013]. Due to the small size and low budget nature of CubeSats, the true cause for “no contact” failures usually remains unknown. The lack of information when a small satellite fails creates a frustrating situation for the satellite builders who have little opportunity to improve their future designs. OSCOM creates the ability to independently verify several independent characteristics of the satellite including spin rate, deployable status, materials and their degradation, and the approximate attitude.

Such a distinct diagnostic tool will enhance CubeSat mission operations and help assess and address mission critical situations. Small satellite failures can be due to countless reasons: uncontrolled spin, failure of antenna deployment, unfavorable pointing leading to power loss, or even incorrect satellite orbit information leading to incorrect ground station antenna pointing. In these cases, spectral and photometric optical observations may be the only option for independently confirming the status of certain physical features. Independent observations are also useful for verifying satellite telemetry. For example, telemetry might indicate a solar panel has been deployed from a satellite, but if the spacecraft is registering low power, an optical observation can help verify if the panels have been fully and properly deployed or if something else might be causing the power issue.

## **RSO Identification**

The same optical characteristics that can be used to support operational missions can also be used to help identify unknown satellites or debris. Although RSO identification is a more difficult problem in general, because neither the object's shape nor attitude are known, it is possible to identify whether an object is rapidly spinning or stabilized and establish an approximate size and material makeup with multi-band spectral observations. A catalog of observations can serve as a reference to classify an unknown RSO as natural/man-made, tumbling/controlled, few/many facets, etc. From an SSA perspective, this information helps protect and evaluate the safety of functional spacecraft in intersecting orbits, and from an intelligence perspective can provide insight into the mission functions of an uncooperative small satellite.

### **1.3 Thesis Overview**

This thesis approaches OSCOM with sufficient detail so that the techniques can be understood by both engineers and astronomers. Chapter 2 begins by reviewing the conditions under which satellites are illuminated and what they might look like when observed. The satellite observation process, following the signal from solar reflected light through OSCOM-analyzed data, is introduced in Chapter 3. Instrumentation, including telescopes and detectors required for optical satellite observation is reviewed next in Chapter 4. Although much of this is general knowledge, it is nonetheless necessary to understand when choosing a system for observing particular types of satellites. Others have claimed CubeSat observations with amateur-class equipment is impossible, but this is likely due to a poor choice of equipment for this task and lack of experience using the equipment. After observation, image data must be reduced and analyzed, as described in Chapter 5. Finally, several samples of satellite photometry are provided in Chapter 6. These demonstrate OSCOM's capabilities to observe a wide range of satellites, including those as small as CubeSats.

# Chapter 2

## Satellite Visibility Basics

OSCOM relies on solar illumination for passive optical observations of resident space objects. It is therefore important to understand how visibility of these objects can be predicted. Obviously the satellite must be in view of the sun and in view of the observer, but it is also necessary for the observer's background sky to be darker than the sun-lit satellite. In visible light, this usually means the sun must be below the observer's horizon.

The timing for when a satellite is visible depends on the satellite's orbital altitude. LEO satellites must usually be observed immediately after sunset or before sunrise, while satellites in higher orbits or GEO are visible late into the night. A schematic of the situation is presented in Figure 2.1. The satellite on the right side of the figure meets all of the criteria for visibility: direct solar illumination, in line of sight of the observer located at **X**, and the observer is in darkness. The satellite will remain visible to the observer even after the satellite passes over the terminator because it continues to be illuminated by the sun at its altitude above Earth. Eventually, the satellite will enter Earth's shadow and appear to dim into the background sky. In Figure 2.1, the dashed part of the orbit represents when the satellite is in darkness.

Assuming a spherical Earth and neglecting atmospheric refraction and Earth's

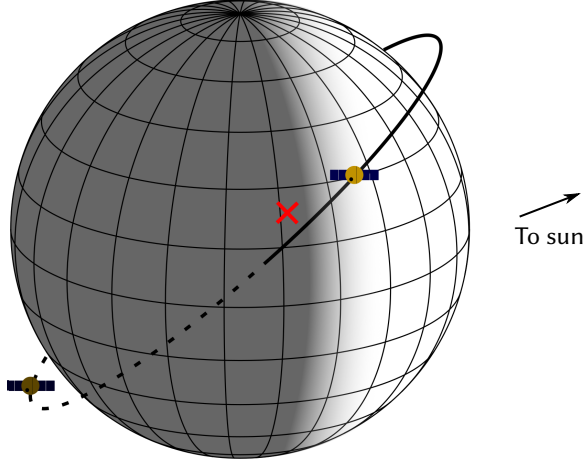


**Figure 2.1:** Satellites in low Earth orbit only remain illuminated (solid orbit line) for a short time after crossing over the terminator. Once they enter Earth’s shadow, they are no longer visible to an observer (dashed orbit line). Additionally, the sun must be below the horizon for the observer (red X) for most satellites to be visible against the background sky.

penumbral shadow, it is straightforward to determine a relationship between a satellite’s altitude and when it enters darkness. The angular distance  $\theta$  from the terminator to where the satellite enters shadow is given by

$$\theta = \arccos\left(\frac{r_E}{r_E + h}\right) \quad (2.1)$$

where  $r_E$  is the radius of the Earth and  $h$  is the orbital height of the satellite [Veis, 1963]. A satellite in a 400 km orbit like the ISS would enter Earth’s shadow at an angular distance of about  $20^\circ$  beyond the terminator. A GPS satellite in a 20,200 km orbit remains illuminated for a much longer time and does not enter Earth’s shadow until an angular distance of  $76^\circ$  beyond the terminator.

Although there is no strict rule on how dark it must be at the observer’s site for a satellite to be visible, a good rule of thumb is the beginning of nautical twilight, when the sun’s center is  $6^\circ$  below the horizon. Although the sky is still bright at this time, stars begin to become visible and bright satellites should be easy to spot as well. The sky continues to darken until the end of astronomical twilight when the sun is  $18^\circ$  below the horizon. After this point, however, only satellites in higher orbits will be visible.

Equation 2.1 can be used to estimate if a given satellite will be illuminated when the sun is a certain angle below the horizon.

## 2.1 The Magnitude System

Although detailed radiometric models often predict the optical power received from a satellite in  $\text{W/m}^2$ , observational data commonly uses the astronomical stellar magnitude system  $m$  to describe the brightness of an observed RSO. The brightness of an object as it appears in the sky is called the *apparent* magnitude or just magnitude, whereas the *absolute* magnitude is the magnitude of an object scaled to a fixed distance from the observer—often 1000 km for satellites in low Earth orbit.

The magnitude system uses a logarithmic scale that roughly approximates the human eye’s response to brightness. In this system brighter objects have lower values and dimmer objects have higher values. For example, the full moon is approximately magnitude  $-12$ , the brightest star in the sky, Sirius, is magnitude  $-1.5$ , and the dimmest object visible to the naked eye is roughly magnitude  $6$ .

The difference in magnitude between two objects has been strictly defined as the ratio of intensity flux  $I$  between them:

$$m - m_{\text{ref}} = -2.5 \log_{10} \left( \frac{I}{I_{\text{ref}}} \right). \quad (2.2)$$

Therefore, every step by 1 magnitude represents a change in intensity of about 2.512. In other words, every 5 magnitudes is a factor of exactly 100 in brightness. To put the brightness of objects on a common scale, the magnitude system is referred to a black body model of the star Vega, which is defined as magnitude  $0$ . Standard star fields across the sky have been carefully imaged in particular filters, e.g. UBVRI from Bessell [1990] and Landolt [1992], and serve as more practical references for accurate photometry.

## 2.2 Estimating Satellite Brightness

A lot of work has been conducted to predict the brightness of a satellite pass. Not only is it important to predict the brightness of a satellite for designing or preparing observational equipment, but the problem of estimating a satellite's brightness can be inverted to help identify or characterize an unknown RSO. Different satellites exhibit a tremendous range of apparent magnitudes depending on their size, orientation, range from the observer, material properties, solar phase angle, etc. Under the right conditions, a glint off the polished antennae of an Iridium communications satellite can exceed magnitude  $-8$  while CubeSats or relatively small satellites in geostationary orbit are magnitude  $11$  or dimmer. Individual satellites can also vary in brightness by several magnitudes during a single pass in case of a glint or flare.

Besides a satellite's characteristic brightness changing due to differences in materials, shape, and illumination geometry, several additional factors confound the observed brightness of a satellite during a pass. A problem common to astronomical observations is that Earth's atmosphere extinguishes the apparent magnitude of an object when it is closer to the horizon. This is caused by increased absorption and scattering of the light ray as it passes through a greater air mass. Unique to satellite observations, the slant range  $R$  from the satellite to the observer changes dramatically over a satellite pass. As expected, the intensity of the satellite-reflected light varies by  $1/R^2$ . This means an object passing through zenith in a  $450\text{ km}$  orbit appears nearly 2 magnitudes brighter than the same object at  $1000\text{ km}$  slant range. For spatially resolved satellites, this is further complicated by the fact that the satellite's apparent size will change with distance and deliver a different number of photons per pixel as it is imaged on the detector array. Methods to correct for these effects will be discussed in section 5.3.

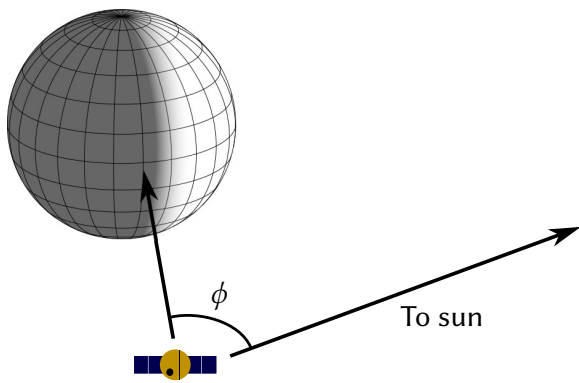


**Figure 2.2:** Solar phase angle  $\phi$  is the angle between the Earth and the sun with the satellite at the vertex.

### 2.2.1 Phase angle

During a satellite pass the lighting geometry for the satellite and observer are constantly changing. To help understand the relationship between the size and shape of an optically unresolved RSO and its brightness, satellite observers sometimes analyze a satellite's light curve, the satellite's brightness over time, using the solar phase angle. The phase angle, defined as the sun-satellite-Earth angle (see Figure 2.2), has proven itself extremely useful for determining the shape of asteroids [Belskaya & Shevchenko, 2014] and is used in the standardized data reduction model of the Inter-Agency Space Debris Coordination Committee (IADC) [Africano et al., 2005].  $0^\circ$  phase angle means the satellite is at full phase.

Phase angle has also proven a useful method for shape analysis of satellites in GEO [Tamara E. Payne & Shine, 2013]. For 3-axis attitude controlled satellites in GEO, as the phase angle changes, the visual magnitude measured by an observer varies primarily because of the change in reflection angle off surfaces on the satellite. Any surface that is illuminated by the sun and visible to the observer may contribute to the observed irradiance. Surfaces that do not meet this condition will not contribute to the observed irradiance. Because the phase angle can be calculated for any satellite that is observed, it is possible to determine the orientation of major reflective surfaces on the

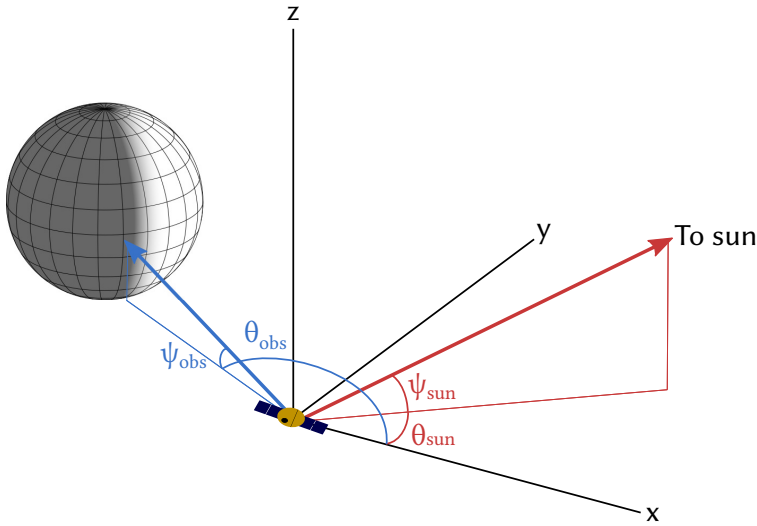


**Figure 2.3:** Four angles are required to fully describe the illumination geometry of an object in orbit. The coordinate system is referenced to the orbiting body so that its attitude must be known to determine these angles. The  $\theta$  angles are in the  $xy$  plane, measured from the  $x$  axis, and the  $\psi$  angles are perpendicular to and measured from the  $xy$  plane.

satellite. If observed over a large range of phase angles, a model of the satellite shape can be created.

Unfortunately, the solar phase angle is not sufficient for understanding the light curve of spinning satellites or satellites in orbits other than GEO. This is largely due to the fact that phase angle is actually a simplification of a system with four angles. As shown in Figure 2.3 and as described by Paul Kervin, Hall, Bolden, and Toth [2010], the position of the sun and the position of the Earth in the reference frame of the RSO are each represented by two angles,  $\theta$  and  $\psi$ . There are an infinite combination of these angles that yield a given phase angle. In other words, there are many possible illumination geometries, and therefore many possible observed magnitudes that could occur for one phase angle.

In general, the shape and attitude of the satellite are not known and this makes the four angles that describe illumination geometry impossible to calculate. However, if either the shape or satellite attitude is known, this information could be used to determine the other. See Hall, Calef, Knox, Bolden, and Kervin [2007] for a description of

attitude and shape effects for non-resolved objects.

### 2.2.2 Phase functions

To help understand the light curve of satellites, models have been created that describe how simple shapes, such as spheres and cubes, reflect light from different angles. These curves that describe the intensity of reflected light as a function of phase angle are called phase functions. Although real-life satellites are a complex aggregate of these and other simple shapes, phase functions can provide a low-order fit for the shape of a satellite based on its light curve.

In general, the magnitude of an RSO can be estimated by

$$m = -26.74 - 2.5 \log_{10} \left( \frac{A\gamma F(\phi)}{r^2} \right) \quad (2.3)$$

where  $A$  is the cross-sectional area,  $\gamma$  is the reflectivity or albedo, and  $F(\phi)$  is the shape dependent phase function that varies with phase angle  $\phi$  [McCue, Williams, & Morford, 1971; Hejduk, Cowardin, & Stansbery, 2012]. As previously mentioned,  $\phi$  also depends on the satellite attitude. The  $-26.74$  scales the value to exoatmospheric stellar magnitudes.

#### Specular and diffuse reflections

There are generally two phase functions for each shape—one for a diffuse reflecting surface and one for a specular reflecting surface. Diffuse reflectors can be modeled using Lambert's reflection law, which assumes constant radiance when viewed from all angles from surface normal. For satellites that are small and far away enough to be considered point sources, a diffuse reflector follows an inverse square and cosine law of

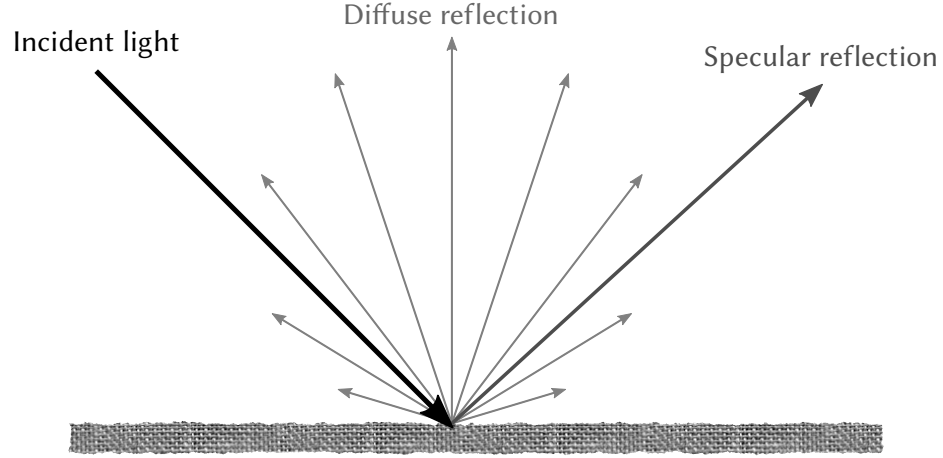


**Figure 2.4:** When light strikes a real surface, it will likely be reflected in two major ways: diffuse and specular. The bright specular reflection occurs at an angle from the surface normal equal to that of the incident ray. Diffuse reflection occurs at all angles and has a cosine intensity distribution for a Lambertian reflector.

irradiance [Rask, 1982]. This can be expressed as

$$E = \frac{I \cos \theta}{r^2} \quad (2.4)$$

where  $E$  is irradiance,  $I$  is radiant intensity, and  $r$  is the distance between the reflecting surface and observer.

Specular reflections follow the law of reflection,  $\theta_{\text{incident}} = \theta_{\text{reflected}}$ , and are mirror-like in appearance. These two types of reflections are diagrammed in Figure 2.4. Most materials are not pure diffuse or specular reflectors, but are somewhere in between, as described by their bidirectional reflectance distribution function (BRDF). To approximate this, a mix of both diffuse and specular models are used simultaneously with weights or mixing coefficients that must total 1, i.e.  $w_{\text{diff}} + w_{\text{spec}} = 1$  where  $w_{\text{diff}}$  and  $w_{\text{spec}}$  are each multiplied by their respective phase functions.

Perhaps the simplest phase function is that of a purely specular sphere,

$$f(\phi)_{\text{spec,sphere}} = \frac{1}{4\pi} \quad (2.5)$$

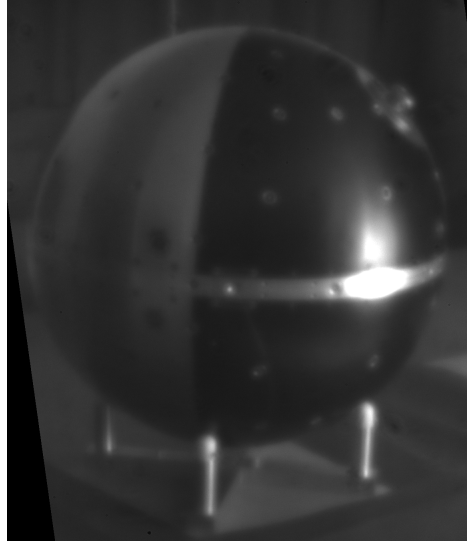


**Figure 2.5:** The Naval Research Laboratory SpinSat satellite in R band (550 nm to 800 nm) has a distinct difference in diffuse reflection from its black and gold colored quadrants. The smooth aluminum shell, however, has strong spectral reflection characteristics, as seen by the bright glint in the black quadrant and mirror-like image of the room seen in the gold quadrant. The specular reflection is nearly independent of the rotation angle of the satellite and dominates the diffuse reflection, making spin rate determination of this satellite surprisingly difficult to pull out of the photometry.

which has no dependence on phase angle [McCue et al., 1971]. In other words, a mirror-like sphere looks the same under all lighting geometries. It would be impossible to distinguish the attitude of such an object (see Figure 2.5). A diffuse sphere does have a dependence on phase angle, and its phase function is given by

$$f(\phi)_{\text{diff,sphere}} = \frac{2}{3\pi^2} ((\pi - \phi) \cos \phi + \sin \phi) \quad (2.6)$$

where  $\phi$  is strictly defined as the difference in longitude of the sun and observer [McCue et al., 1971].

The phase function of a diffuse flat plate depends on the individual latitudes of the sun  $\phi_1$  and observer  $\phi_2$ :

$$f(\phi)_{\text{diff,plate}} = \frac{1}{\pi} \sin \phi_1 \sin \phi_2. \quad (2.7)$$

The magnitude of a diffuse flat plate will always be greater than that of a diffuse sphere

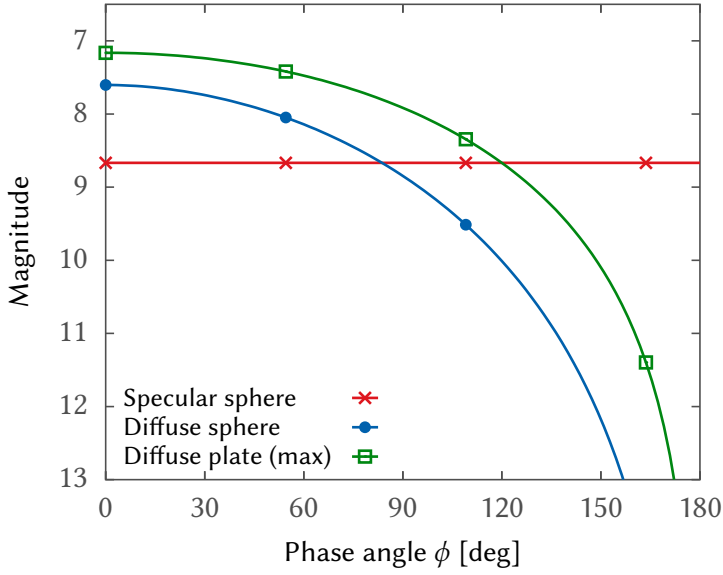


**Figure 2.6:** Several sample phase functions plotted using Equation 2.3 with an albedo of 0.1, a cross sectional area of  $1 \text{ m}^2$ , and a range of 1000 m. The magnitude of the diffuse plate is the maximum possible magnitude, i.e.  $\phi_1 = \phi_2$ .

of equal cross-sectional area, as shown in Figure 2.6. A table of phase functions, including the functions for a cylinder, are given in McCue et al. [1971].

### 2.2.3 Albedo-area product

Besides the shape-dependent phase function, the albedo-area product ( $\gamma A$  product) is another important term in Equation 2.3. Each component of a satellite can be considered an individual facet with an intrinsic albedo-area product, as shown in Figure 2.7. For example, a simple satellite might consist of two major facets: a cylindrical spacecraft bus and solar panel off to the side. The reflected brightness of an RSO depends on both the cross-sectional area and albedo, but without knowledge of the material optical characteristics and object shape, the two are intertwined in the photometric data. Additionally, the area contributing to the observed brightness is actually the *projected* area based on the RSO attitude and illumination geometry.

The concept of the albedo-area product has been very useful in determining space-

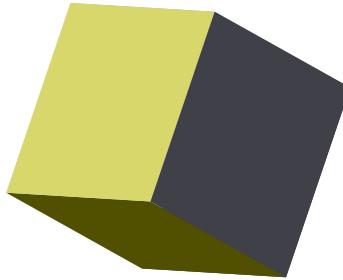


**Figure 2.7:** A simple cube-shaped satellite has 6 facets—one for each side. Each facet illuminated by the sun and visible to the observer contributes to the observed magnitude of the satellite.

craft shape or attitude using photometric measurements. Tamara E. Payne et al. [2013] have been able to demonstrate a method for converting photometric measurements to the projected albedo-area of an RSO—a process that is independent of sensor and color band and is able to decompose the aggregate albedo-area product of an unresolved RSO to the respective  $\gamma A$  product of the major object components, e.g. bus and solar panels. This product might also serve as a useful tool for the classification of objects, especially in GEO. The ability to break down the photometric signature of unresolved RSOs into individual facets with individual  $\gamma A$  products has also been exploited by many others, including Calef, Africano, Birge, Hall, and Kervin [2006], Chaudhary et al. [2013], and Hope [2014], although the focus has been on objects in GEO.

### Satellite albedo values

In order to relate the observed optical brightness of a satellite to its physical size, the albedo must be known. For a basic analysis, the space debris community often assumes space debris have an albedo of 0.08 or 0.1 [Gibson, Pearce, Blythe, & Trujillo, 1993; Wellemans & Bowers, 2007]. Intact satellites tend to have a higher value of around 0.2, although studies from the 1990s found objects with a wide range of albedos, from 0.02 to 0.5 [Lambert, Osteen, & Kraszewski, 1993; Henize, O'Neill, Mulrooney, & Anz-Meador, 1994]. Material reflectivity darkens over time from radiation and atomic oxygen exposure so there is some ambiguity when extracting albedo-area products, even if the object

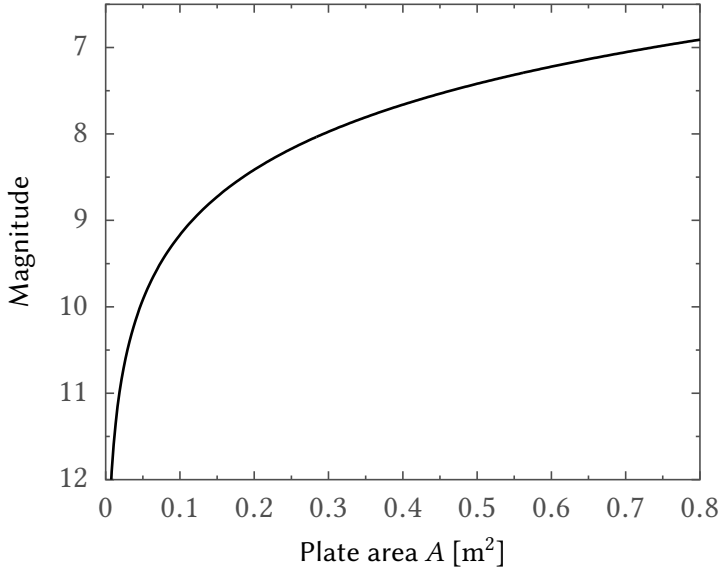


**Figure 2.8:** The magnitude of a diffusely reflecting flat plate has a strong dependence on the plate area, especially when the area is very small.

material is known.

The temperature of the satellite is also related to the visible albedo of a satellite. Although a large, dark satellite might have the same optical brightness as a small, reflective satellite, the dark satellite will likely be hotter, and thus brighter at thermal infrared wavelengths. Therefore, if observations are made simultaneously in visible and thermal infrared bands, it may be possible to make a better estimate of the object size [P.W. Kervin, Africano, Sydney, & Hall, 2005].

The role of the albedo-area product remains important for small satellites because a change in a small facet area can have a relatively large impact on the reflected intensity of the small satellite. For example, a 3U CubeSat of albedo 0.1 has approximately a  $0.03 \text{ m}^2$  surface area on its largest face, which results in an expected magnitude of about 10.5 mag if it's passing overhead in a 450 km orbit. If a single  $1 \times 30 \text{ cm}$  strip, e.g. the CubeSat rail, is polished to have an albedo of 0.5, the magnitude increases to about 10.1 mag—a significant increase in brightness! Similarly, if it were to deploy an additional  $10 \times 30 \text{ cm}$  panel, its magnitude would increase by 0.75 mag. Of course a similar

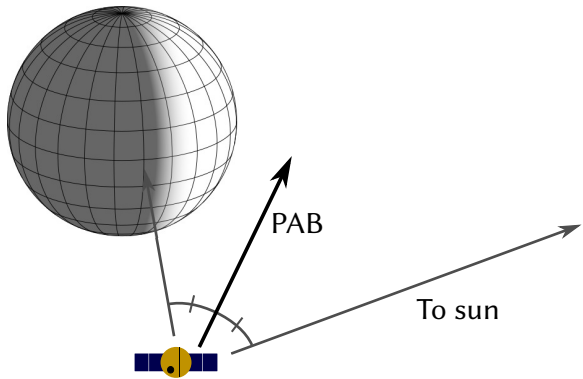


**Figure 2.9:** The phase angle bisector (PAB) extends midway between the satellite-to-sun and satellite-to-observer vectors. When a satellite facet normal is aligned with the PAB, a glint will be observed.

effect occurs when the projected area changes as a satellite rotates. The relationship between RSO area and magnitude is shown in Figure 2.8.

#### 2.2.4 Glints

Specular flat plates, such as solar panels, often have the ability to create mirror-like glints when the illumination geometry is under the correct conditions. These glints can be remarkably bright—potentially by several magnitudes. Glints allow the satellite attitude to be constrained because they only occur when the specular condition for the glinting facet is satisfied. In other words, when the angle of incident sunlight is equal to the angle from the facet to the observer, the light beam will be directed at the observer.

Satellite observers commonly use the concept of the phase angle bisector (PAB) to more easily discuss the glint condition. The PAB is the unit vector directed midway between the satellite-to-sun and satellite-to-observer vectors, as seen in Figure 2.9. A glint occurs when the facet normal and the PAB approximately coincide [Hall et al., 2007]. At every time  $t$  that a glint occurs, the facet normal must be oriented in the direction of the PAB.

Not only are glints produced by solar panels, but they are also produced by wire antennas, such as those used on small satellites or CubeSats. By analyzing the pattern

of bright body glints and smaller antenna glints, it may be possible to discriminate CubeSats from others with slightly different designs or antenna configurations [Hall, 2008].

Smaller facets produce their own glints and provide additional information to the observer on the satellite shape. Although these glints are dim compared to the glints produced by solar panels or the main body of a satellite, if they repeat multiple times under similar lighting angles, they are likely caused by the same component on the satellite. These can be used to characterize unresolved satellites, especially in GEO where lighting conditions change much more slowly than LEO [Hall & Kervin, 2013].

Because glints often have such strong signatures, they are especially useful for anomaly resolution. As discussed by Paul Kervin et al. [2014], unusual glints were observed in observations of the Galaxy 15 satellite just 15 minutes after anomalous behavior began. This suggests regular optical observations could be used to indicate satellite instability after only a short amount of time. Additionally, glints can be used as convenient photometric markers to establish an accurate satellite spin rate to confirm if the satellite attitude control system is operating properly [Hall et al., 2006].

## 2.3 Satellite Color

Color provides an extra dimension of information to solve the space object identification problem. It can be approached in two primary ways: with the use of colored filters or with the use of a spectrograph. Each has pros and cons, but they will not be discussed here.

The traditional approach for RSO characterization or identification has been to compare the color or spectra of observed RSOs to laboratory measurements of paints and materials commonly used on rockets or spacecraft. The utility of color has been demonstrated in several observation campaigns [Nishimoto et al., 2001]. Cowardin et al. [2013]

analyzed low resolution spectra and multi-band color photometry of fragments of Titan IIIC transtage debris in GEO, and were able to roughly match many fragments to laboratory spectra. Lederer et al. [2012] performed similar work on the IDCSP spacecrafts and similarly concluded they could identify general solar cell material, but could not determine the specific type. They attribute this partially to space weathering and partially to rotational variation between their measurements in different filters.

To capture color information on LEO satellites, Frith, Gibson, Knox, and Kuluhiva [2008] made observations in two or three photometric filters simultaneously by using two or three identical telescope systems. This allowed them to capture color information with high temporal resolution. Their goal was to distinguish between specular and diffuse reflections using the change in color over time. This is possible because it has been shown that specular reflections take on the color of the source, which for simple satellites is the sun [Cook & Torrance, 1982]. By comparing the color of the incident light (color of the sun) to the color of reflected light, specular and diffuse reflections can be separated.

### 2.3.1 Color index

The term “color” as used in astronomy or satellite observations is actually a difference in the brightness of an object in two optical bandpass filters (see section 4.4 for a discussion of common filters). The Bessell UBVRI filter set [Bessell, 1990] represents passbands for ultraviolet, blue, visible, red, and near-infrared light, respectively. Commonly, the colors  $B - V$  or  $V - R$  are used, although other combinations also exist. The Sun has a  $B - V$  index of 0.65 [Gray, 1992]. Bluer objects have smaller, even negative,  $B - V$  values, while redder objects have larger  $B - V$  values. This might seem counterintuitive, but is due to the fact that higher value magnitudes represents a dimmer object.

# Chapter 3

## OSCOM Design Overview

OSCOM addresses many aspects of optical tracking and observation of resident space objects. This chapter introduces the OSCOM system from a high level so that the reader can understand the data collection process and how OSCOM works. It also discusses OSCOM's tracking system.

### 3.1 Signal Flow

A simple way to understand the satellite observation process is to follow the signal from source to end product. For OSCOM, the ultimate goal of an observation or set of observations is to characterize the targeted RSO as a particular type of object, to detect a change in an object's characteristics, or to determine a particular physical state of the object, e.g. spin rate or attitude. Although the algorithms to provide this information to an end user (satellite operator, analyst, etc.) are not yet developed, OSCOM currently produces data that can be supplied to those algorithms.

The satellite optical “signal” itself changes form throughout the flow. Each step is described below and summarized in Figure 3.1.

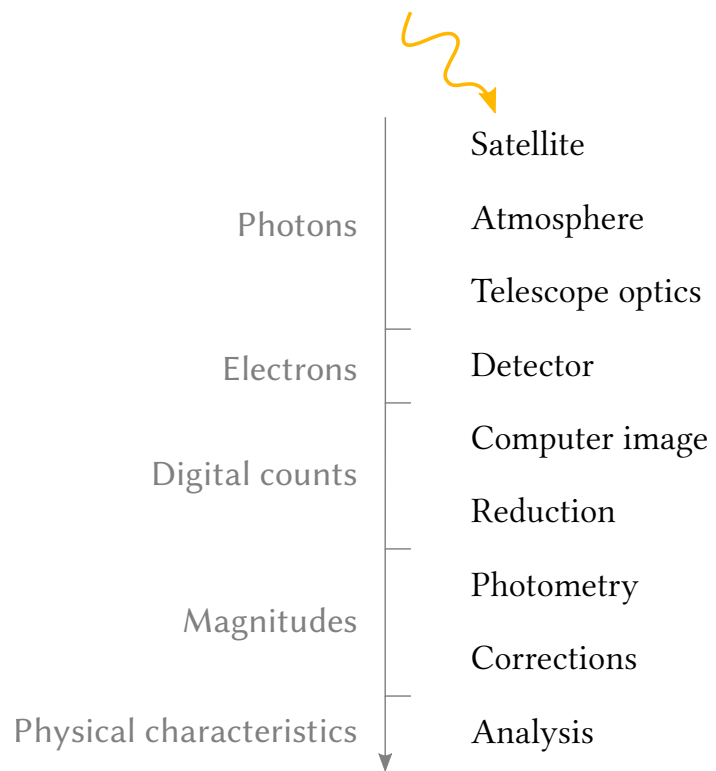


**Figure 3.1:** Signal flow for satellite observations by solar reflected light with OSCOM. Photometry is the most common OSCOM product, but in place of that stage, images could be combined and processed for spatial satellite imaging, or undergo different corrections if spectroscopy is performed.

### 3.1.1 Photons

The signal flow begins when sunlight strikes the satellite surface. We assume the incident light is unaltered solar illumination only, although earthshine may exhibit a small effect at very large phase angles<sup>1</sup>. Light will reflect off the satellite in a combination of diffuse and specular reflection, depending on the satellite materials and age. We will assume that at least one of the satellite facets has directed reflected light in the direction of an observer in darkness so that the satellite will be visible.

As the reflected light propagates towards the observer, not only does the irradiance drop by the square of the distance traveled, but the light is subjected to atmospheric optics effects. The atmosphere is particularly troublesome for satellite observations because satellites spend significant time of each pass low in the sky. Their angular rates are lowest when they are low in the sky and highest when they are directly overhead. Therefore, they spend a lot of time near the horizon and a short amount of time high in the sky. Although astronomers schedule their observations to observe a particular object when it is high in the sky, satellite observers often do not have that luxury.

Light from objects high above the horizon travel through less air, i.e. “lower airmass”, than objects near the horizon. Objects at the zenith are at an airmass of 1, whereas objects at the horizon are approaching 38 airmasses. A plot of airmass against elevation angle ( $90^\circ - \text{zenith distance}$ ) is shown in Figure 3.2. Obviously, the more air light must pass through, the more it is distorted. As a rule of thumb, astronomers will not perform photometry on an object until it is more than  $30^\circ$  above the horizon.

---

<sup>1</sup>Earthshine does not meaningfully contribute to the brightness of an RSO below about  $130^\circ$  phase angle, which is seldom exceeded in observations for when the sky of the observer must be in darkness. Additionally, earthshine models are currently lacking in their ability to reproduce observations, making corrections nontrivial [Hejduk, 2011].

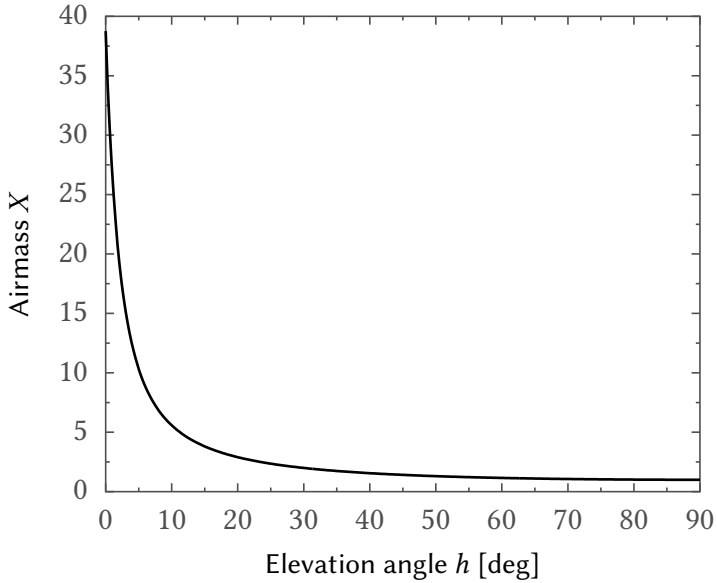


**Figure 3.2:** Light from objects near the horizon must pass through significantly higher airmass than objects 20° to 30° elevation. This model for airmass was developed by Pickering [2002].

### Atmospheric optics

A few of the major distortions that impact satellite observations are atmospheric seeing, absorption and scattering, and refraction. Turbulence in the atmosphere caused by thermal cells and wind distort the incoming wavefront with both low-level roughness and larger scale tilt error that moves the image around. This process is called scintillation and is also the reason stars appear to twinkle by eye. During a long exposure ( $\gtrsim 1$  s), the movement of the image is time averaged across a larger disk than that of the diffraction limit of the telescope. The size of the disk is known as “seeing”. Under better sky conditions, the seeing disk is smaller and effectively results in higher resolution imaging using conventional techniques. A smaller disk also means the same amount of light is being directed to a fewer number of pixels on the detector, leading to a greater per-pixel signal-to-noise ratio. Seeing is an especially important factor for spatially resolved imaging because it distorts the wavefront reducing the resolution and contrast of the image.

The atmosphere also absorbs and scatters light as it passes through. All wavelengths

are partially absorbed, and therefore the apparent magnitude of an object is extinguished by the atmosphere. The greater the airmass, the greater the extinction. Scattering is a strongly wavelength dependent effect. Red light is scattered less than blue light, leading to a “reddening” effect as an object nears the horizon. A secondary effect of scattering is that light produced by sources on the ground is scattered back down as light pollution. Not only does this decrease contrast for observations, but it results in additional background sky noise that impacts the quality of photometry.

For precision orbit determination, atmospheric refraction also plays a role by shifting the apparent position of a source in the sky from its actual position if the atmosphere were not present. Therefore, a correction model must be applied if optical satellite observations are being used for orbit determination or astrometry. Because refraction is a wavelength dependent effect, differential refraction leads to dispersion of the image. For spatially resolved imaging, if filters are not used, the image may appear blurred because of dispersion of the red and blue components of the light.

The reflected light, which has been distorted by the atmosphere, is next collected by the telescope optic. The optical system has characteristics that determine the brightness of the image, angular resolution, and field of view, and also introduces its own aberrations into the signal. Telescope optics will be discussed in detail in section 4.1. The telescope ultimately delivers the incident light onto a focal plane.

### 3.1.2 Electrons

OSCOM uses CCD or CMOS detectors at the focal plane to record the satellite observation. These detectors, which will be further discussed in section 4.2, consist of a rectangular array of pixels that together create a two dimensional image. Each individual pixel transforms incident photons into electrons via the photo-electric effect and stores the charge until the array is read out.



**Figure 3.3:** A cropped, unfiltered .fits image of the POPACS-2 nanosatellite acquired January 20, 2016 at 10:46:17.895 UTC using OSCOM’s RASA telescope in Daytona Beach, FL. The bright line in the upper left is a star streaking through the field of view as the telescope tracks the satellite.

### 3.1.3 Digital counts

When a command is sent to the detector to stop exposing and read out the array, the charge stored in each pixel is digitized by an analog to digital converter. At this point, each element of the image array now contains a value equal to the corresponding number of analog digital units (ADU) or “counts”. Background sky is dark and has few counts, while stars and the RSO are bright and have a higher number of counts. The array is read out and transferred from the detector to a computer multiple times every second.

At high frame rates, the images are read into memory using a double buffer before being saved to the hard drive. Depending on the image capture software used, the entire image sequence may be saved as a single uncompressed file, such as .ser. Individual .fits images, a standard data format in astronomy<sup>2</sup>, can then be extracted from the .ser file. A sample image is shown in Figure 3.3. The data at this point, whether a spatially resolved image or unresolved photometry, is contained in a 2D image matrix. Every image is then corrected for sensor and optical defects in a process called image reduction before being analyzed. This will be discussed further in section 5.1.

---

<sup>2</sup>See fits.gsfc.nasa.gov.

If the image is spatially resolved, several images will be selected, registered, and combined, as described in section 5.5. If the RSO is unresolved, the next step will be to run the images through a detection algorithm that locates the pixel position of the target RSO within the image. This information is used to position the aperture for photometric analysis.

### 3.1.4 Magnitude

Through photometry, which will be detailed in subsection 5.2.2, the total flux from the target RSO is summed up to produce an instrumental magnitude. The value of this magnitude is not calibrated with the standard system, but can be used for time series analysis of the RSO over every image frame. Before that analysis is conducted, the instrumental magnitudes must be corrected for atmospheric extinction and satellite range. For satellites of simple geometry, it might also be possible to correct for phase angle, but this is not done for the majority of observations.

### 3.1.5 Physical characteristics

Now that the RSO has been observed, the data reduced, and photometry produced, the signal can be analyzed to extract information of interest. A time series of magnitudes may be analyzed using a fast Fourier transform (FFT) or another spectral analysis technique to determine flash period and ultimately spin rate of the RSO. In fact, there is a significant amount of information that has been collected up to this point that can contribute to the space object characterization or identification. The data collected during a single pass could include the speed and direction, or orbit, of the RSO, color index, absolute magnitude, time series photometry characteristics, or spectral information. By collecting this data over repeated passes of the RSO, machine learning algorithms can be used to characterize the object or alert to changes. Specific algorithms to estimate a known satellite's deployables status or approximate attitude could be applied directly on

the time series photometry.

## 3.2 Tracking System

OSCOM focuses on detailed characterization of targeted RSOs. To accomplish this, OSCOM makes use of a satellite rate tracking system that follows satellites as they pass through the sky (see Tracking Modes in section 1.1). The tracking system follows a traditional design and is summarized below.

### 3.2.1 Physical system

Several different techniques have been built and tested for tracking satellites with OSCOM. This work has converged on two main techniques, the choice of which often comes down to the equipment being used and the amount of time available to the observer for setup and take down. These two techniques will be referred to as *optical feedback* and *elements only* and may require different equipment setups in order to be successful. Sample setups for each of these tracking techniques are shown in Figure 3.4.

#### Elements only

The elements only tracking method does exactly that, relying only on RSO orbital elements to guide the telescope along the objects path. Orbital elements in the form of two line elements (TLEs) are produced by the Joint Space Operations Center (JSpOC) and are currently freely available to satellite operators, academics, and hobbyists at space-track.org. Additionally, unofficial sources with orbital elements collected by amateur satellite observers can provide satellite observation maps and tools as well as elements for classified objects not released by JSpOC<sup>3</sup>. The disadvantage to orbital elements is that some satellites are updated more frequently than others and small satellites tend

---

<sup>3</sup>Popular amateur websites for satellite elements include [www.calsky.com](http://www.calsky.com) and [heavens-above.com](http://heavens-above.com). Dr. T.S. Kelso provides a cleaned-up version of the JSpOC TLEs at his website [celestrak.com](http://celestrak.com).



**(a)** Celestron RASA in elements only track mode.

**(b)** Meade LX200 and Borg 77EDII in optical feedback track mode.

**Figure 3.4:** Two sample OSCOM tracking setups for the elements only and optical feedback track mode.

to have the lowest accuracy and least frequently updated elements. This means the telescope might miss the satellite entirely or quickly track off the real satellite path.

To counter some of the downsides of elements only tracking, it is best to use an electro-optical system with a fairly wide field of view. This provides the best opportunity to see and track the satellite without losing it. Additionally, if the satellite begins to wander from the center of the image, the observer can update the telescope rates with a quick press of a computer key. This basic human-in-the-loop tracking is sufficient for most wide-field telescope systems.

### Optical feedback

Rather than requiring the telescope operator to manually update the telescope rates if the RSO drifts from the center of the detector, the tracking software can do the same automatically using computer vision algorithms. The tracking software uses orbital elements as a first approximation of the RSO position, but after tracking begins, the satellite is detected in the image and the telescope mount is commanded to adjust the

track rates so that the satellite stays centered. To give the best odds of acquiring the satellite as it passes over the observer, a wide-field tracking telescope, coaligned with the main science telescope, is used to provide the automatic optical feedback tracking. This then allows the satellite observer to use a main telescope with a longer focal length and smaller field of view, as shown in Figure 3.4(*b*).

### 3.2.2 Tracking process

The OSCOM tracking system follows a basic process that is currently performed by a telescope operator, but which could easily be automated. The process consists of three major stages, as outlined in Figure 3.5. The first phase is pre-track, during which the tracking software prepares to track the RSO. This usually occurs while the object is still below the horizon. The telescope operator loads the orbital elements into OSCOM's tracking software, which then propagates them for the duration of the satellite pass. This process creates a table or ephemeris of satellite position in the sky for every second from when the satellite rises above the observer's horizon to when it sets. A cubic spline is then fit to the azimuth and elevation of the ephemeris and the derivative of the spline is calculated. Ultimately, the commands sent to the telescope mount will not be positions, but angular track rates for each axis of the tracking mount. By precalculating a spline derivative internal to the tracking software, the angular rates of the satellite can be determined on the fly by simply evaluating the spline derivative function at the current time. Once this function is created, the tracking software propagates the orbital elements to the position of the satellite when it passes through a preset elevation of 10° and then slews the telescope to that location.

The telescope mount motors are turned off until the instant the satellite enters the field of view of the telescope. At that time, the mount motors rapidly slew up to the apparent angular rates of the satellite, as predicted by the previously computed spline derivative. At every time step, perhaps 20 times every second depending on the proce-

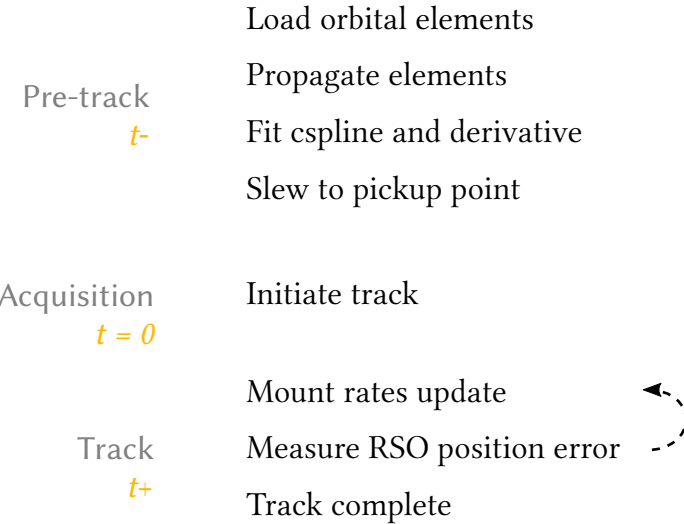


**Figure 3.5:** Optical tracking of satellites or orbital debris occurs in three major phases: pre-track, acquisition, and track. During the pre-track phase, the telescope computer propagates the object's orbital elements and slews to the pickup location. When the satellite arrives at that location, it is acquired by the system, and the telescope mount track rates are continuously updated to the rate of the RSO.

sor speed, the current time is entered into the spline derivative and the mount rates are updated. In the elements only tracking mode, this process continues until the satellite sets or the track is aborted by the telescope operator. The operator might also issue commands to the tracking software to slightly change the track rates in one or both axes in case the satellite is drifting in the field of view. If in the optical feedback track mode, the error—pixel distance from the satellite's actual to ideal centered location—is used to modify the mount rates. This keeps the satellite centered throughout the pass even if the orbital elements are old or inaccurate.

### TLE vs. CPF elements

OSCOM tracking software currently supports two forms of orbital elements. The first, two line element set (TLE), also known as an elset, is a plain text data format for encoding orbital elements of an Earth-orbiting object for a given point in time. The prediction formula, published by the United States Department of Defense in *Spacetrack Report No.*

*3*, can be used to propagate the orbital position of the satellite to a specific time [Hoots & Roehrich, 1980]. Several perturbation models have been used to create TLEs: SGP, SGP4, SDP4, SGP8, and SDP8. The most common are SGP4 and SDP4 for low and deep space orbits, respectively. Small updates have been made since the original release of *Spacetrack Report No. 3*, which have been compiled into a non-proprietary version of SGP4 theory presented in Vallado, Crawford, Hujasak, and Kelso [2006]. The accuracy of SGP4 is about 1 km [Oltrogge & Ramrath, 2014]. There are many ports available of the SGP4 code from the original Fortran. OSCOM's tracking code makes use of the C++ SGP4 library written by danrw<sup>4</sup> and provided under the permissive free software Apache License. This library includes the updates suggested by Vallado et al. [2006].

Although far less common, the International Laser Ranging Service (ILRS) publishes orbit predictions using its own format called consolidated prediction format (CPF). The CPF format is an ephemeris of satellite position in cartesian geocentric space at 1 minute intervals [Ricklefs, 2006]. The data are interpolated between the 1 minute ephemeris intervals extending for several minutes on either side of satellite rise and set time. After conversion to azimuth/elevation angles, the interpolated data goes through the standard cubic spline fit and derivative calculation. CPF data is only available for satellites that are tracked by laser ranging stations.

### 3.2.3 Choosing a track mode

Given the option of elements only or optical feedback tracking, how does an observer choose which to use? Experience with OSCOM has demonstrated that for an electro-optical system with a  $\approx 1^\circ$  field of view, elements only track mode is sufficient for photometry of nearly all satellites. The disadvantage is that if the elements are old or the telescope mount is not carefully aligned to north, the mount might need a couple of human-in-the-loop adjustments to keep the RSO centered on the detector. Optical feed-

---

<sup>4</sup>[www.danrw.com/sgp4](http://www.danrw.com/sgp4)

back tracking has multiple advantages, most important of which is its ability to keep an object centered throughout its pass, even if the original elements or mount alignment were slightly off. Because it does not require human intervention, it is especially convenient if an OSCOM system were operated remotely and automatically. Because it precisely maintains the target object in the center of the detector, it is also useful for high resolution imaging at high focal length and with a coaligned tracking telescope. The disadvantage is increased complexity of the setup. At minimum, it requires an additional computer, and it might also require an additional telescope and camera.

### 3.3 Tracking Logic and Control

OSCOM's tracking software, called Auriga, is based on work originally completed by the author as part of an Embry-Riddle Aeronautical University student research award called *An Aerospace Tracking System for Embry-Riddle's Astronomical Telescopes*. That effort provided funds for cameras and development of a software code to control some of Embry-Riddle's telescopes for tracking satellites. Auriga has gone through several versions and remains in active development, although some of the basic ideas are presented below.

Auriga is written in C++ for speed and adaptability, and makes use of the OpenCV library for open source computer vision<sup>5</sup>. OpenCV is a popular library that provides optimized image processing algorithms across several interfaces including C++, Python, and Java, and supports Windows, Linux, Max OS, and mobile operating systems. It has a strong focus on real-time applications and is released under a BSD license for free academic and commercial use. Auriga also has wxWidgets GUI and non-GUI versions. Experience has shown the GUI can allow the observer to more rapidly prepare for satellite passes and more easily keep files organized, but requires additional software development time over the non-GUI version.

---

<sup>5</sup>[opencv.org](http://opencv.org)

### 3.3.1 Mount commands

Auriga code currently supports two telescope control systems: TheSkyX<sup>6</sup> and Gemini 2<sup>7</sup>. TheSkyX, a full featured planetarium software by Software Bisque, controls a variety of telescope mounts including the Paramount line, also made by Software Bisque. The Gemini 2 system is most often used on Losmandy mounts, such as the G-11 owned by the author. Both of these mounts are of the German Equatorial style (see section 4.5 for a discussion of tracking mounts) and require commands be sent to the right ascension (RA) and declination (DEC) motors to track an RSO as it passes through the sky.

Both of these telescope control systems can be commanded over the TCP network protocol using the Winsock library. The Gemini 2 system can be connected directly to the network and called by its own address. Text commands are then sent directly to the Gemini 2 and Auriga listens for responses. The text commands come from a table of commands understood by Gemini 2<sup>8</sup>. These commands include options such as requesting the current declination or right ascension, requesting the DEC or RA velocity, commands to move to a position in the sky, or setting motor rates. Paramount mounts controlled by TheSkyX are commanded in a roughly similar way. TheSkyX can open a TCP server that listens for connections on port 3040. Assuming TheSkyX is running on the same machine as Auriga, the TCP server address should be set to localhost or 127.0.0.1. Once the connection is made, the mount can be commanded using Java Script commands<sup>9</sup>. Through the sky6RASCOMTele object, Paramount mounts can have their tracking rates directly set for each axis independently.

As discussed in subsection 3.2.2, in elements only tracking mode, the steps for tracking are straight forward. A command is first sent to the mount to point to the precalculated satellite intercept position in the sky. It is simplest to issue this as a position

---

<sup>6</sup><http://www.bisque.com/sc/pages/TheSkyX-Professional-Edition.aspx>

<sup>7</sup><http://www.losmandy.com/losmandygoto/gemini2.html>

<sup>8</sup><http://www.gemini-2.com/web/L5V1serial.html>

<sup>9</sup><http://www.bisque.com/scriptTheSkyX/>

in the azimuth/elevation coordinate system rather than right ascension/declination because the later is fixed to the (moving) stars, rather than the horizon. When the satellite passes into the field of view, commands are sent from Auriga to the telescope control system to set the mount rates in RA and DEC such that they match the satellite rates in RA and DEC at the same instant in time. This process is repeated many times per second to continuously match the angular rates of the satellite as it passes through the sky. If the telescope mount is out of alignment or the orbital elements are old or inaccurate, position errors might grow during the satellite pass. The telescope operator may manually adjust the track rates by a small percentage to keep the RSO near the center of the detector. If the satellite is missed or accidentally driven off the chip, the telescope can be commanded to slew to a new predicted intercept point at some time, e.g. 20 s, in the future. Alternatively, optical feedback tracking can be used so that Auriga automatically adjusts the track rates to keep the RSO centered.

### 3.3.2 Optical feedback

Optical feedback is similar to the observational technique called *autoguiding*. In astronomy, autoguiding keeps the target object centered on the detector during a long exposure by continuously imaging a neighboring guide star with short exposures. The telescope control system sends corrections to the tracking mount if the guide star begins to drift. Optical feedback or automatic tracking with OSCOM performs a similar task except the “autoguiding” is performed on the rapidly moving RSO. Although this ensures stable and controlled active pointing and tracking, it requires increased complexity not only of the hardware, but of the software.

### Calibration

Before the tracking camera can provide meaningful feedback to the control system, it must be calibrated so the rotation angle and pixel scale are known by Auriga. The

calibration can be performed using a distant object on the ground, or by using a star if the mount is tracking at sidereal rate during the calibration. The calibration occurs in five repeated steps. After slewing to the calibration target, the telescope operator selects the target in the tracking camera image. A blob detector locates the target and calculates a subpixel centroid and the telescope then jogs a short distance in one axis. The user selects the target again, the process repeats, and then the telescope jogs in the other axis, and the process repeats again. These steps are summarized graphically in Figure 3.6.

The calibration process builds a matrix that describes how motion on the detector array corresponds to motion in the sky and vice versa. The calibration matrix is

$$\begin{bmatrix} \text{RA} \\ \text{DEC} \end{bmatrix} = \frac{1}{s} \begin{bmatrix} a & b \\ c & d \end{bmatrix} \begin{bmatrix} u \\ v \end{bmatrix} \quad (3.1)$$

where  $a = \overline{\Delta x}$  and  $b = \overline{\Delta y}$  in the RA direction and  $c = \overline{\Delta x}$  and  $d = \overline{\Delta y}$  in the DEC direction,  $(u, v)$  represents pixel positions of the target, and  $s$  is the angular distance that the telescope jogs in between each step. Once the calibration is complete, the angular distance in RA and DEC can be calculated from a pixel offset  $(u, v)$  on the detector. This allows tracking errors on the detector to be corrected by the tracking software that sends commands to the mount RA and DEC drives.

### 3.3.3 Tracking algorithms

Several tracking algorithms have been coded into Auriga for optical feedback tracking of satellites. Several assumptions have been made that simplify the image processing required for target detection and tracking. First, there is very little background clutter—only detector noise and streaked background stars. Second, the target object is a point or nearly a point. This is true for all unresolved satellites, and because most resolved satellites will be imaged through a wide field tracking camera, they remain small on

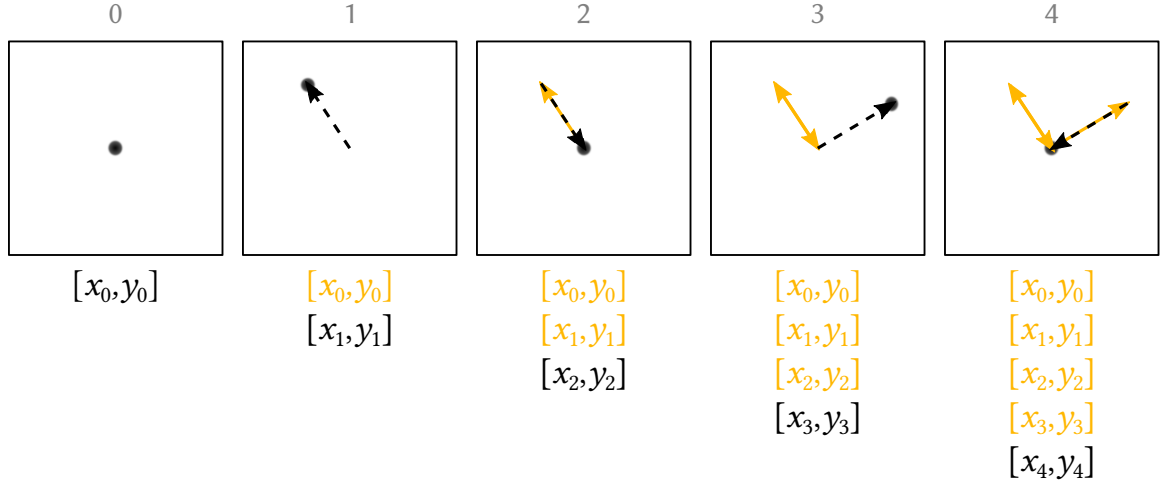


**Figure 3.6:** The optical feedback tracking system can be calibrated in five steps by pointing at a star. After the user clicks on the star, the telescope moves and the process repeats until the star has moved back and forth in both axes.

the detector. Third, the RSO will be significantly above the background noise. Because orbital elements are required for OSCOM tracking, the signal counts from the satellite will build over the exposure time so that even dim small satellites will have good signal to noise ratios.

These assumptions mean even a simple “brightest pixel” algorithm can be used. In Auriga, this is called `nroiMax`. After the RSO passes into the telescope field of view and the mount begins tracking by orbital elements, the observer simply clicks on the RSO in the image. This action creates a region of interest (ROI) that masks all but a small region of pixels around the click position. Within the ROI, the RSO is identified as the brightest pixel using the `ncvo::nminMaxLoc()` of OpenCV. Once the position of the RSO is determined, the error  $e(t)$  between the current RSO position and “target” RSO position on the detector is calculated:

$$e(t) = (u, v) - (u, v)^* \quad (3.2)$$

where  $(u, v)$  is the RSO pixel coordinates on the detector and  $(u, v)^*$  is the nominal position. This situation is diagrammed in Figure 3.7. In most cases, the nominal position

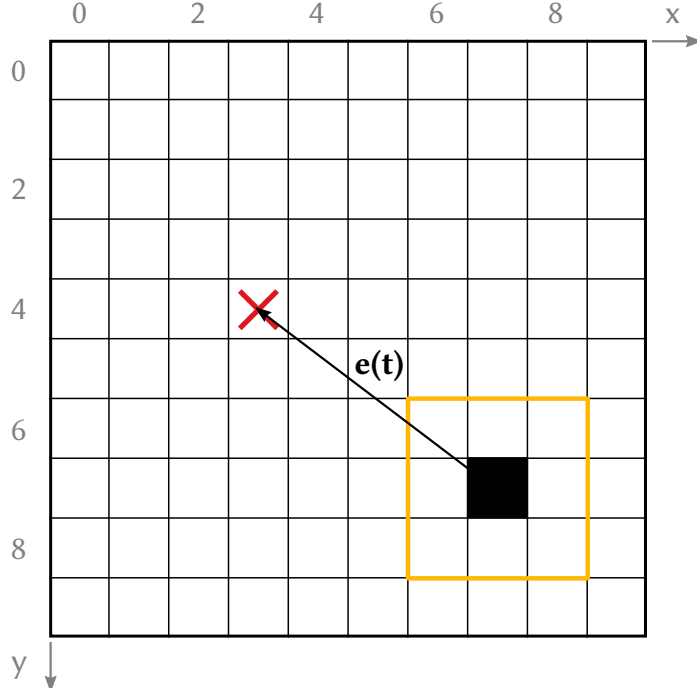


**Figure 3.7:** When tracking begins, the observer selects the RSO (black pixel) and a region of interest (yellow box) is drawn around it. The tracking algorithm moves the RSO to the targeted location on the detector (red x). The distance between them is called the error  $e(t)$ .

is the center of the detector. However, if the tracking telescope and main telescope are not perfectly coaligned, the telescope operator may purposely have the tracking algorithm drive the satellite so it is not centered on the FPA of the tracking telescope, but so it is centered on the FPA of the main telescope. This offset should be determined before the pass begins.

Once the error is established, the pixel error is transformed to RA and DEC using the calibration matrix. A proportional controller is used to adjust the mount track rates from the prior rate, beginning at the nominal element-derived rate, to a higher or lower rate so that the RSO will be driven to the target position on the detector array. This can be expressed mathematically as

$$dRA(t) = dRA(t - 1) + K_p \left( \frac{1}{s} \begin{bmatrix} a \\ c \end{bmatrix} e(t - 1) \right) \quad (3.3)$$

where  $K_p$  is the proportional gain,  $dRA(t)$  is the new rate in RA and  $dRA(t - 1)$  is the current rate (set by the last time step). The same is true for the DEC axis. Rather than using the correction term directly, the rates are filtered with an exponential moving average. This delays the responsiveness of the controller, but helps ensure smooth track motion. With each new image received from the tracking camera, the ROI is updated to be centered on the position of the brightest pixel within the old ROI, and the process repeats. Over several frames,  $e(t)$  will hopefully decrease to 0.

The process described above requires an operator to manually select the RSO in the image so that an initial ROI can be established. However, if full automation is required, a blob detector such as `ncvo::nSimpleBlobDetector()` can be used. With a high inertia ratio (low elongation) requirement, star streaks should be automatically filtered out and the only “circular” group of bright pixels in the image will hopefully be the RSO. A similar technique can be used as the regular tracking algorithm, which is especially useful for resolvable objects. By requiring a high inertia ratio, star streaks will not be selected by the algorithm as the target object.

### 3.3.4 Potential improvements

The primary focus of OSCOM has been photometry of small satellites. Therefore, the most important requirement of the tracking system has been smooth tracking. As long as the target RSO is roughly near the center of the detector, the error term is not very important because it does not affect the quality of the photometry. However, if high focal ratio, narrow field of view (NFOV) telescopes are used for photometry or spatially resolved imaging, it may be advantageous to use a complete PID controller. The integral and derivative terms are easy to integrate into the tracking code, however the tuning of the system is complicated. Not only does the frame rate of the process depend on the detector and computer running Auriga, but most observations by OSCOM are performed using portable or semi-permanent setups that are setup and taken down for

every night of observation. This makes it difficult to fine tune the multiple terms of the PID control. Additionally, independent gains would need to be determined for each of several different telescope and mount systems used by OSCOM. Besides PID, a Kalman filter on either the image processing or control stage might benefit the smoothness of the tracking system [Zhao, 2009]. Kalman filters are able to predict the location of the RSO in the next frame and do so with immunity to noise.

Although OSCOM assumes the orbital elements belonging to the target RSO are roughly correct, i.e. close enough so that the object will be somewhere in the tracking camera FOV at the predicted time, many satellites with old orbital elements arrive early or late from the predicted time but along a similar trajectory. OSCOM currently begins tracking at the time predicted the RSO will enter the center of the FOV. However, even with a FOV of  $1^\circ$  across, satellites in LEO only offer a window of about  $\pm 1$  s before they pass through the FOV. If it is known that an object has old or questionable orbital elements, a low SNR streak detection algorithm may offer the ability to track objects that arrive early or late. The telescope waits and stares at the expected intercept location until a streak is detected at which point the standard tracking process begins. This is a more advanced concept, but increases the capability of OSCOM to characterize unknown objects.

# **Chapter 4**

## **Instrumentation**

OSCOM makes use of a variety of telescopes, detectors, filters, and tracking mounts in order to match instrumentation with observation goals. The ideal equipment for small satellite photometry is not the same as that for high resolution imaging of large LEO satellites. Although many different systems across the world are successfully tracking satellites, it is important to understand the advantages and disadvantages of these set ups. This chapter provides general background on telescopes, detectors, filters, and tracking mounts, as well as criteria that OSCOM uses for selecting its instrumentation.

### **4.1 Telescopes**

Telescopes are arguably the most important part of an optical satellite observation system. They are responsible for collecting light from satellites not visible to the naked eye and magnify the image of resolved satellites. Although all telescopes take incoming light and direct it to a focal plane, there are many different designs with associated mechanical and optical trade-offs.

### 4.1.1 Telescope parameters

Ultimately, telescopes accomplish two tasks; they make objects appear brighter and larger. Associated with these are the contrast and resolution of the optical system. To determine how much brighter or larger a telescope image will become, telescopes are characterized by several parameters. The first basic parameter is *aperture diameter*,  $D$ . The diameter of the aperture is often given with the name of a telescope, such as “8 inch Schmidt Cassegrain” or “150 mm refractor”. This specification describes the extent of a telescope’s light gathering power and resolution. The larger the aperture, the brighter the image and the higher the resolution. Physically, the aperture is usually the diameter of the first optical surface that incoming light strikes on the telescope, although more generally it is the diameter of the system element that determines the cone angle of rays being focused in the image plane.

The second parameter is *focal length*,  $f$ . The focal length of an optic is the distance to the point of ray convergence on the optical axis. Collimated incoming light will be focused at a distance equal to the focal length from the optic. For complex optical systems with multiple elements, the effective focal length is the net focal length of the elements working together. Focal length directly drives angular magnification. Longer focal lengths spread incoming light over a larger distance on the focal plane. Physically, focal length is weakly related to the physical size of the telescope. More directly, it is related to the distance of the light path in the telescope optical system. For small telescopes, typical focal lengths are in the hundreds of millimeters while larger telescopes have focal lengths of meters to over 10 meters. A diagram of the effective focal length of a multi-element optical system is shown in Figure 4.1.

The first two parameters can be combined into a single parameter known as the *focal ratio*,  $f/ \#$ . Focal ratio is defined as  $f/D$  and describes the final angle of convergence of light onto the focal plane. Low focal ratios, usually slightly larger than 1, are

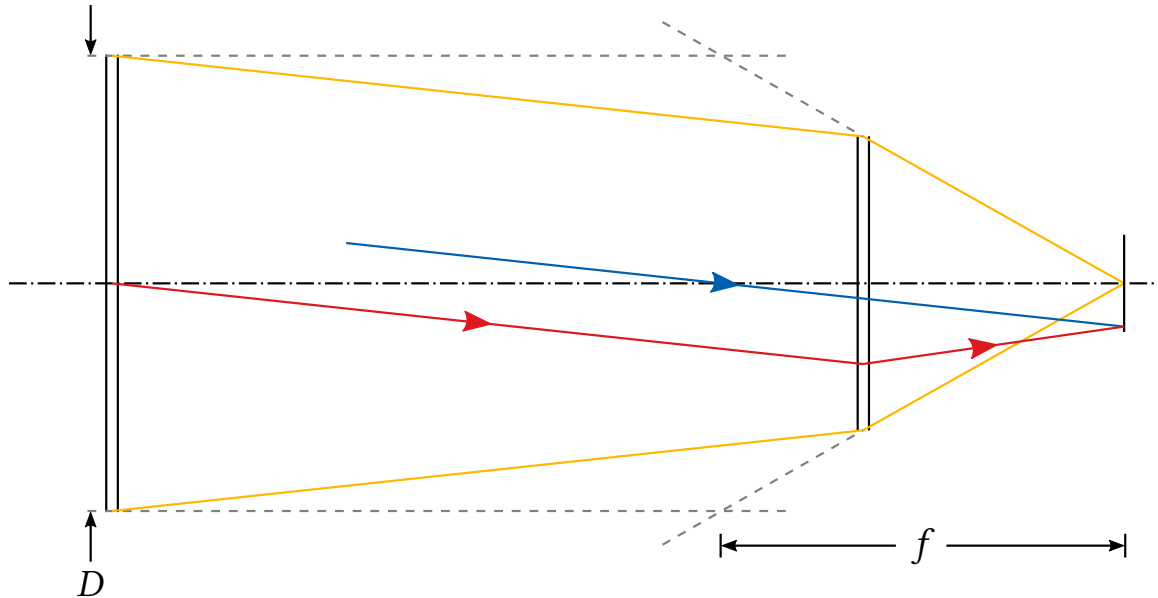


**Figure 4.1:** In this two element optical system, the aperture  $D$  is the diameter of the first optical element. The effective focal length  $f$  of the system is shorter than the physical length because of the influence of the second optic. Knowing the distance from the last optical surface to the focal plane, the effective focal length of the system is determined by the intersection of the final converging cone with the height of the aperture [Sacek, 2015]. This system is a simplified version of the Borg 77EDII refractor and focal reducer.

known as “fast” optical systems because light captured over a relatively wide view angle is delivered to a small area on the focal plane. A high focal ratio, e.g.  $f/20$ , spreads light from the same view angle over a large area on the focal plane and is known as a “slow” optical system. This is because if both of these systems are imaging the same source at the same distance, individual detector elements on the fast optical system will collect photons at a higher rate than the slow system. The detector elements of the fast system look larger when viewed through the optics than the slow system. If both systems have the same aperture diameter, the total number of photons collected across the entirety of each (perfect) detector will be the same.

Besides the focal ratio, there are several other properties that can be derived from the focal length and aperture. One of these properties, field of view (FOV), is especially important for choosing telescopes for satellite imaging. Field of view is determined by the focal length of the telescope and by the physical diameter of the detector (discussed

in section 4.2). The geometry shows the field of view can be calculated as

$$\theta = 2 \arctan \left( \frac{d/2}{f} \right) \quad (4.1)$$

where  $\theta$  is the FOV,  $d$  is the physical width of the detector array, and  $f$  is the focal length. For small angles, this is typically simplified to

$$\theta \approx \frac{d}{f} \quad [\text{rad}]. \quad (4.2)$$

Many astronomical telescopes typically have fields of view around  $20'$  across, but the recent increase in electronic detector size has allowed some telescopes to reach fields of view several degrees across.

The aperture diameter of a telescope drives the theoretical resolution of the telescope. Assuming perfect optics, the *diffraction limit* using the Rayleigh criterion is

$$\theta_R = 1.22 \frac{\lambda}{D} \quad (4.3)$$

after applying the small angle approximation. The Rayleigh criterion states that the minimum resolvable detail in an image occurs where the first diffraction minimum of one point source coincides with the maximum of another. An otherwise perfect optical system will always be limited by diffraction. The realizable image resolution is further reduced by atmospheric effects, optical aberrations, and the detector sampling scale.

Aperture also drives the brightness of the image. Image intensity is related to the area of the aperture, which for circular optics goes by  $D^2$ . This means a telescope of 12 inch aperture collects 2.25 times as much light as an 8 inch telescope, even though the diameter has only increased by 1.5 times.

An oft forgotten component of a telescope's light-gathering power is its *transmission efficiency*. To minimize transmission losses, refractive elements are often coated with

high efficiency coatings to greatly reduce reflection. Even if corrector plates or refractor lenses are carefully protected from the elements when they are not in use, over time they will pick up air particulates that drive their transmission efficiency down. The same is true for reflecting mirrors. First-surface mirrors are carefully coated with a variety of metals, but even if dielectric reflective coatings with losses less than 1% are used, they will eventually deteriorate and pick up dust and particulates. Refractive elements also have inevitable absorption losses. All told, the transmission efficiency for an amateur telescope might vary between 80 and 95% [Sacek, 2015].

A final concept is called *etendue*, which describes how light is spread out by an optical system. It is also referred to as optical throughput and is a conserved quantity in perfect optical systems. Etendue is sometimes called the  $A\Omega$  product because it is equal to

$$G = A\Omega \quad (4.4)$$

where  $G$  is the etendue,  $A$  is the beam area or system pupil, and  $\Omega$  is the beam divergence or system FOV. A larger etendue represents greater light collecting power. If the field of view is known, the aperture in  $\text{m}^2$  may simply be multiplied by the FOV in square degrees. Otherwise, the projected solid angle of the entrance pupil can be approximated by

$$\Omega \approx \frac{A_{\text{ep}}}{f^2} \quad (4.5)$$

following the definition of the solid angle. This can be further simplified to

$$\Omega \approx \frac{\pi}{4(f/\#)^2} \quad (4.6)$$

which demonstrates the inverse square relationship between focal ratio and optical throughput. Low focal ratio optical systems have higher throughput than high focal ratio systems.

### 4.1.2 Aberrations

Although telescopes are designed to meet theoretical operating criteria, the figure, i.e. curvature, of real optical elements deviates from the nominal shape. This is especially true of amateur and COTS hardware that is manufactured to lower tolerances. Some telescope tubes will be better than others just by chance, while others will be worse. Optical systems can suffer from many aberrations, but five are particularly common in telescope designs and will be introduced here.

*Spherical aberration* is perhaps the most basic aberration an optical system can have. Optics manufacturers prefer that optical elements (lenses or mirrors) be shaped spherically because this is much easier to make than other conic sections. Unfortunately, the constant radius of curvature of a spherical element means that paraxial rays at different radial distances from the center of the element will come to focus at different points. Although this effect can occur in both refracting and reflecting telescopes (see subsection 4.1.4), it is rare in modern multi-element refracting telescopes because multiple lens elements cancel the effect out. Spherical aberration sends energy into the rings of the Airy disk and washes out detail in spatially resolved images. It is easiest to identify spherical aberration by the significant difference in brightness between intra and extrafocal images.

To avoid spherical aberration either non-spherical optical elements or corrective lenses are used. If a parabolic primary is used in a reflecting telescope to remove spherical aberration, the next most likely aberration is called *coma*. Coma is an off-axis aberration that appears near the edge of the field of view. Point sources affected by coma are imaged as comet-looking objects that all point to the center of the field.

To avoid coma, more complicated designs using hyperbolic surfaces or multiple non-spherical surfaces have been designed. Unfortunately, some of these systems suffer from *astigmatism*. Astigmatism is also an off-axis aberration and exists because an optical

element has two different focal surfaces corresponding to each plane of the system. Many optical designs are astigmatism free, and for those that are not, it is often possible to use a corrective lens to remove the aberration.

For low focal ratio, wide field of view electro-optical systems, *field curvature* can become a problem. Many telescope designs naturally create curved focal planes where off-axis light focuses slightly closer to the objective than on-axis light. Because nearly all COTS detectors are flat, it is impossible to have the entire field of view in focus at the same time. In order to remove field curvature, a field flattener must be used in front of the detector.

Lastly, refractors or telescopes using corrective lenses may suffer from *chromatic aberration*. This is caused by the wavelength dependent nature of refraction, so that bluer light comes to a focus closer to the objective than red light. Multi-lens systems known as achromats or apochromats bring multiple wavelengths of light to the same focal point, removing the color distortion.

Note that many of these aberrations can be reduced or even removed entirely by adding optical elements—either additional mirrors or corrective lenses. Commercial camera lenses have many internal elements for this reason. Unfortunately, there are transmission losses at every element, reducing the efficiency of the lens overall. For astronomy and satellite observations, this reduction cannot be tolerated, which is why telescopes usually have only a few optical elements with expensive, non-spherical figures.

#### 4.1.3 Evaluating the effect of aberrations on optical quality

Every telescope design comes down to trades of cost, engineering complexity, transmission efficiency, aberration removal, etc., but even the perfect telescope design is manufactured with limited tolerance. Opticians and observers have developed measures to evaluate the performance of actual telescope systems. One of the most common and

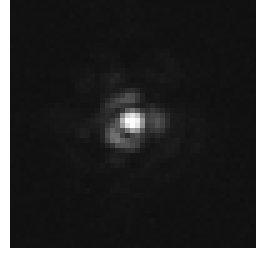


**Figure 4.2:** A single 10 ms i' band image of a star taken by a 12 inch Schmidt Cassegrain telescope, 2× barlow lens, and the Manta G-235 detector on a night of fair seeing. The Airy disk is in the center, surrounded by arcs of the first diffraction ring. The diffraction limit of this telescope at 775 nm is 0.64 arcsec/pix and the pixel scale is 0.2 arcsec/pix. The measured FWHM of the Airy disk is about 3.5 pix, close to the expected size of 3.2 pix.

useful measures is the *Strehl ratio*. This ratio compares the peak intensity of the aberrated Airy disk (see Figure 4.2) to the peak Airy disk intensity of a perfect wavefront. The Strehl ratio can take on values between 0 and 1, with 1 being an ideal telescope operating at its diffraction limit. In general, the goal of telescope designs is to place as much energy into the Airy disk as possible in order to maximize contrast.

Strehl ratio is typically calculated by measuring the RMS wavefront error of the system (or element) and can be approximated using the equation

$$\text{SR} \approx e^{-(2\pi\omega)^2} \quad (4.7)$$

where SR is the Strehl ratio and  $\omega$  is the RMS error in units of the wavelength [Sacek, 2015]. Typically, Strehl ratios greater than 0.8 are considered capable of diffraction limited imaging and correspond to an RMS error of about  $\lambda/14$ . This should be considered an absolute minimum. A very good optical system has a Strehl ratio of about 0.94 [Royce, n.d.].

Strehl ratio is a representation of the bulk error from all aberrations and does not provide details on what the aberrated image may look like. To do so, it is necessary to measure the point spread function (PSF) of the optical system. The PSF is the image of a point source as viewed through the system. As mentioned above, even perfect systems

have limited spatial resolution due to diffraction at the edge of the aperture, and therefore the PSF consists of a central Airy disk surrounded by concentric rings. Errors in the system tend to move energy from the disk into the rings. Measuring the encircled energy of the PSF out to the first ring and comparing it to the ideal Airy function is akin to the Strehl ratio. An image of the PSF is easily obtained by observing stars. However, this is not the PSF of the optical system, but of the system and atmosphere combined. This can be measured around the time of each observation and potentially used as a source for deconvolution of the image.

For spatially resolved imaging, it is also important to consider the modulation transfer function (MTF) of a telescope optic. The MTF is a description of how an optical system operates as a function of spatial frequency. In other words, how much contrast does a system deliver when imaging objects that are closely spaced versus objects that are spaced further apart. An example MTF plot for three theoretical telescopes is shown in Figure 4.3. To resolve fine details on an object, the telescope must be capable of delivering high contrast at small spatial frequencies. The MTF is the Fourier transform of the PSF and so the Strehl ratio is like a frequency averaged MTF.

#### 4.1.4 Telescope types

Telescopes can be broadly separated into three distinct categories: refractors, reflectors, and catadioptrics, as shown in Figure 4.4. Refractors are what people classically think of as a telescope: a long skinny tube with a lens on the end. Refractors tend to provide very sharp images because there is no secondary obstruction, but they are very expensive for their size. None have ever been made larger than Yerkes Observatory 40 inch. Despite these limitations, refractors are the default choice for small optics, such as finder scopes or tracking telescopes, because of their small size and unobstructed aperture. Additionally, they require little maintenance because they are a sealed tube aligned by the manufacturer.

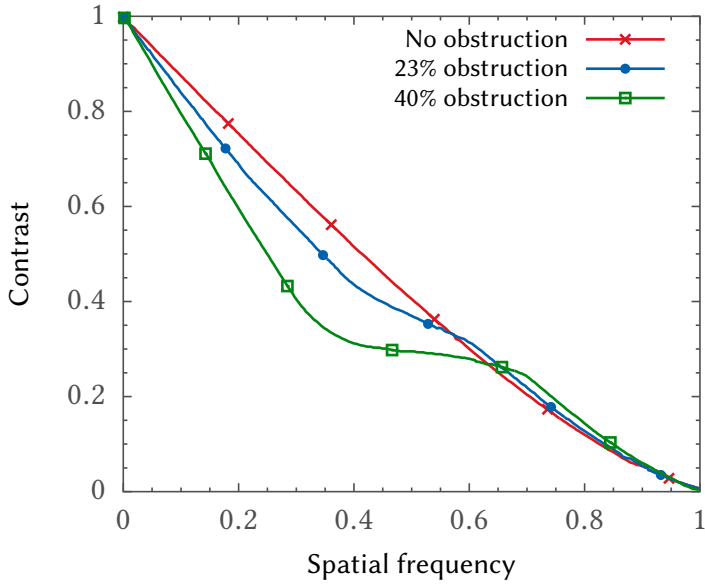


**Figure 4.3:** Theoretical modulation transfer functions for three 12 inch  $f/5$  reflecting telescopes. The central obstruction (secondary mirror) size reduces the performance of the telescope at low to mid frequencies, but maintains the performance or very slightly outperforms the unobstructed telescope with fine detail. Curves modeled using the Aberrator software ([aberrator.astronomy.net](http://aberrator.astronomy.net)).

The best telescopes by dollar-value are reflecting telescopes. These use mirrors only and are therefore less expensive than refractors of the same size. Because mirrors can be supported from underneath, reflecting telescopes can be extremely large. The largest single (primary) mirror telescopes are over 8 m in diameter. Unfortunately, reflectors usually require that a secondary mirror be placed in the lightpath of the primary. Not only does the secondary obstruction impact the MTF of the telescope, but the structure that supports the secondary mirror assembly must also pass through the light path. Light is diffracted by the assembly, removing energy from the Airy disk to spikes typically seen emanating from the center of bright stars in astrophotos. Reflecting optics must also be carefully aligned by the observer for optimum performance.

Catadioptric systems combine both lenses and mirrors and are very popular among amateur observers. Perhaps their most useful feature is their compact size. By using a folded light path, long focal lengths can be achieved in a small physical space. They also offer many optical performance gains over pure refracting or reflecting telescopes. They

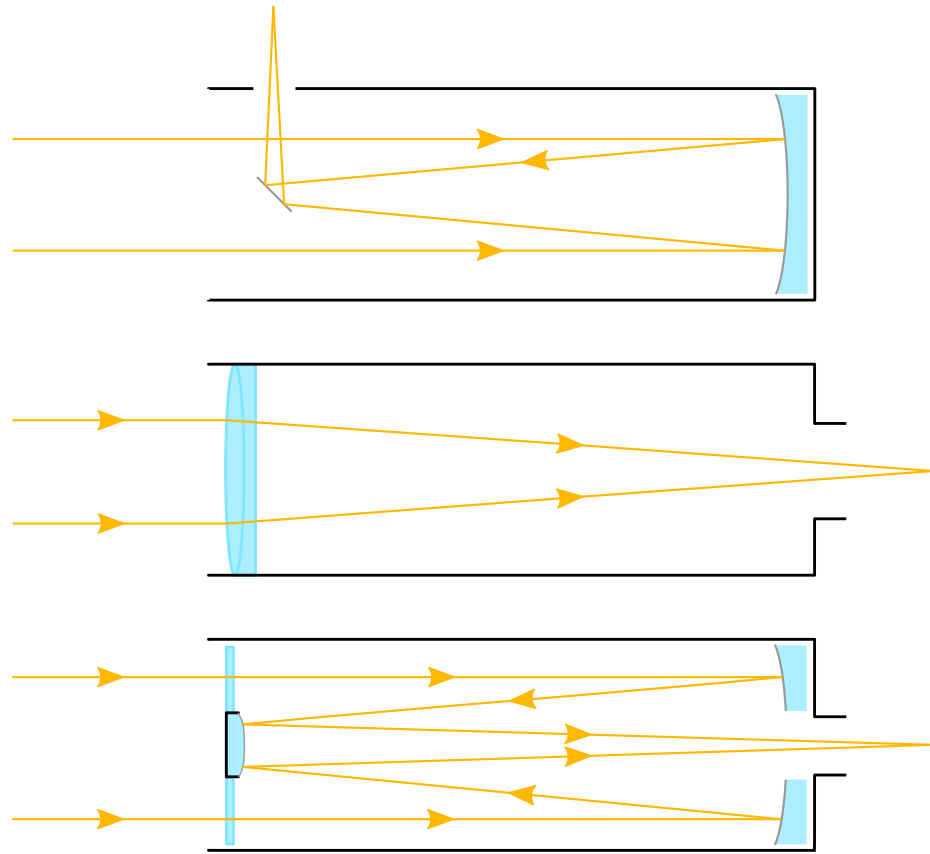


**Figure 4.4:** The three basic types, from top to bottom, are reflectors, refractors, and catadioptrics.

exhibit virtually no chromatic aberration and have greatly reduced coma compared to reflectors. The secondary mirror is typically supported by a glass correcting element and therefore no diffraction spikes are formed.

## 4.2 Detectors

Detectors are the second major component of a satellite optical tracking system. After light is collected by the telescope and delivered as an image on the focal plane, the detector captures those photons and transforms them into a digital representation of the image. Just like telescopes, detectors come in a few major types and can be characterized by several properties.

### 4.2.1 Detector types

The standard scientific visible imaging detector is the charge-coupled device (CCD). CCDs have an array of photoactive capacitors that accumulate charge during an exposure. Each of these are essentially image pixels. When the exposure is complete, charge is transferred from row to row until it reaches the final row, which acts as a serial register. Charge is then transferred across the serial register into an output amplifier before it is digitized by an analog to digital converter. The key trait to the CCD architecture is that charge is transferred across the device and the entire array is (usually) converted to a voltage and digitized at a single point off chip.

The other common visible imaging detector is the complimentary metal oxide semiconductor (CMOS). CMOS active-pixel sensors have circuitry at each pixel that amplifies the collected charge and additional circuitry converts the voltage to digital data elsewhere on the chip. Because the CMOS manufacturing process is used in many industries, the cost of CMOS detectors is far less than CCDs. Their cost, in combination with their reduced power requirements compared to CCDs, are the reason they are found in cell phones, web cams, and other consumer devices. A limitation of this technology is that the fill factor is reduced. In other words, because there is circuitry at each pixel that is not light sensitive, the effective light collecting area of the sensor is reduced. Manufacturers must install microlenses above the pixel elements to collect light over the complete area and focus it onto the photo sensitive region in order to increase the fill factor of CMOS detectors.

There are also variations on CCD and CMOS detectors. A common variation on the CCD is the electron multiplying CCD (EMCCD). This innovation allows single photon detection while maintaining high quantum efficiency. An EMCCD is not limited by the readout noise of the conventional output amplifier because a solid state electron multiplying register is added in between the serial register and amplifier. The EM register

works in hundreds of stages, wherein impact ionization is utilized to produce secondary electrons, and hence EM gain. This allows very weak charges in the serial register to be increased to higher levels.

CCD and CMOS technology has been somewhat combined on a single chip to produce what is known as the scientific CMOS (sCMOS) image sensor. The goal of sCMOS was to produce a high frame rate CMOS detector capable of the high quantum efficiency and low noise seen in CCDs. Although the specifics of this architecture are protected by the companies that make them, the general design has pixels that can be read through either a low gain or high gain path. The low gain path can detect large numbers of photons with high noise while the high gain path detects low numbers of photons with low noise. The two are added together “in an interesting way” to obtain a high dynamic range, low noise image [Baker, 2011].

Finally, many CCD and CMOS sensors are naturally sensitive out to about 1000 nm because of their silicon based chip. To capture light further into the near infrared and shortwave infrared (SWIR), an InGaAs image sensor is a common choice. Depending on their design, they are capable of detection out to between 1.7  $\mu\text{m}$  to 2.6  $\mu\text{m}$ . SWIR has the advantage over visible imaging in that the technology allows similarly high resolutions and optical systems as visible imagers, but the longer wavelength means reflected light is less affected by the atmosphere. For satellite imaging, there are two major disadvantages to SWIR. The first is airglow, which is a natural emission of light in the upper atmosphere as bright as the full moon in SWIR. The increased background noise and decreased contrast makes the use of SWIR to observe small satellites difficult. Additionally, solar irradiance is reduced at this wavelength, which means fewer solar photons are being reflected by the satellite. Therefore, SWIR is effectively only an option for spatial imaging of large, bright satellites.

## 4.2.2 Detector characteristics

The most basic characteristic of an image sensor is its size. This includes both the size of the chip and the size, also known as the pitch, of individual pixels. The chip size determines the total field of view in conjunction with the focal length of the optics it is attached to (see Equation 4.1 and 4.2). Typical sensor sizes vary between just a few millimeters diagonally to several tens of millimeters. The pixel pitch determines the pixel scale or instantaneous field of view (IFOV), which is how much sky is covered by one pixel. This is important so that spatial sampling of the target object is obtained. In other words, it partially determines the effective spatial resolution of the data. Typical pixel pitches vary from around  $4\text{ }\mu\text{m}$  for small pixels to  $24\text{ }\mu\text{m}$  for larger pixels.

Part of the sensor unit will be the analog to digital converter (ADC). Although this may or may not be on the same chip as the photosensitive detector, it is a fundamental part of the camera device. Based on the dynamic range, noise, and sensitivity of the detector, the manufacturer will use an analog digital converter that creates between 8 and 24 bit samples for each pixel. Most scientific CCDs are 16 bits per pixel, corresponding to 65,536 intensity levels per pixel, although many CMOS detectors are only 12 bit, creating 4,096 levels per pixel. Both CCD and CMOS detectors have a reduced dynamic range for accurate photometry because the detector response becomes nonlinear before saturation. The dynamic range in physical units of the signal is determined by the gain of the output amplifier before the ADC. The gain/ADC combination leads to a certain number of photo-electrons per analog digital unit (ADU). For cameras that have software controlled gain, when the gain is increased, the ADC maps the input signal to a smaller number of electrons per ADU (see Figure 4.5). Typical image sensor gains are around  $1\text{ e}^-/\text{ADU}$ .

The photosensitive region of the detector has a quantum efficiency (QE) that describes what percentage of incident photons are converted to charge carriers in the

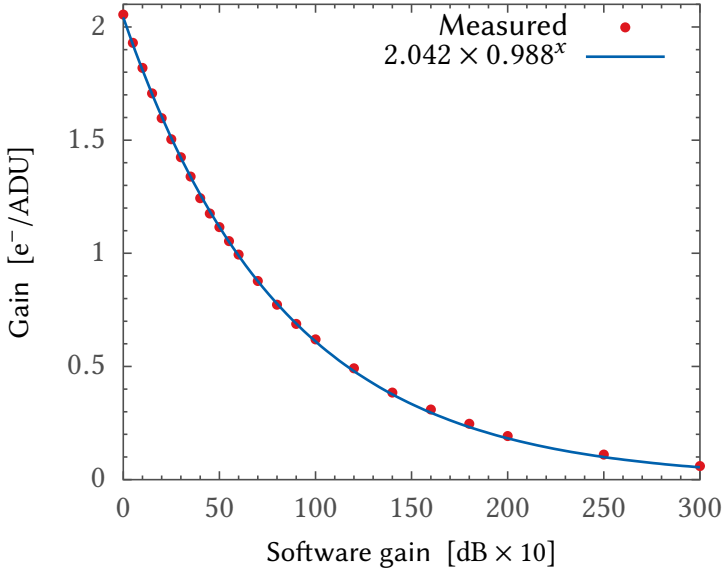


**Figure 4.5:** The Manta G-235 CMOS detector has a software controllable gain from 0 to 40 dB. By characterizing OSCOM’s unit, the true gain in  $e^-/\text{ADU}$  was determined as a function of the software gain. Having a wide range of gain selection makes the Manta a versatile camera, capable of imaging bright and dim objects.

device. QE is a highly wavelength dependent characteristic, and although all silicon based detectors have roughly similar QE curves, manufacturer specific doping and design decisions can increase or decrease the QE. A sample QE curve for the Manta G-235 CMOS detector is shown in Figure 4.6. Ideally, the QE of a detector is as high as possible so that as many incident photons as possible are detected by the device.

Random thermal noise produces dark current in image sensors. The longer the exposure, the more time thermal noise has to add to the charge collected in the sensor. Although the dark current of a detector can be characterized and subtracted from science frames, there is noise associated with the dark current that decreases the total signal to noise ratio of any science measurements. Luckily, at the short exposure times used by OSCOM ( $< 1 \text{ s}$ ), dark current is negligible. It is dominated by the read noise. Read noise is present in every image read out from the detector and is impossible to avoid or subtract out. Read noise can be reduced by registering and co-adding frames, but this is counterproductive for time-resolved photometry. The amount of read noise in

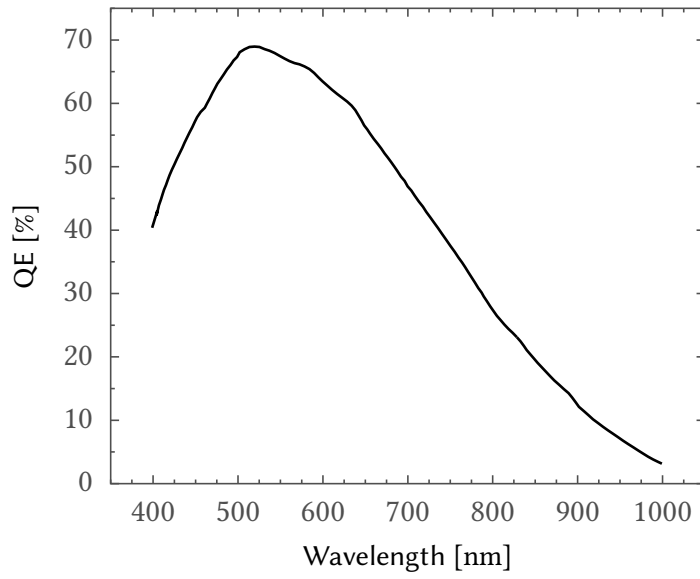


**Figure 4.6:** Quantum efficiency curve of the Manta G-235 CMOS detector used by OSCOM. All silicon based image sensors have QE curves shaped similar to this. REPRODUCED FROM Allied Vision [2015].

a frame is a function of the internal electronics of the device and is therefore up to the manufacturer to minimize. Typical values for scientific cameras range from 1 to 15 e<sup>-</sup> RMS. Note that there is a significant difference between these two values. Every time you halve the total system noise, you have effectively doubled the dynamic range of the image.

An additional noise source is present in every image, even if the detector is perfect. This is called shot noise or Poisson noise because it is modeled by a Poisson process. Shot noise is caused by the particle nature of light so that the signal to noise ratio for large numbers of photo-electrons,  $N$ , is

$$\text{SNR} = \frac{N}{\sqrt{N}} = \sqrt{N}. \quad (4.8)$$

Therefore, the shot noise is reduced by collecting more light.

Individual image sensors will have their own fixed pattern noise (FPN). FPN consists of both dark signal non-uniformity across the detector as well as photo response

non-uniformity from pixel to pixel. Some pixels might be more or less sensitive to dark current, i.e. “hot” and “cold” pixels, while others might provide more or less gain than the pixels around them. The latter is especially important to consider in CMOS detectors that have individual pixel circuitry. Hot and cold pixels or other fixed signal spatial effects will be mostly removed by a dark frame subtraction. Likewise, pixel-to-pixel sensitivity variation can be corrected using a flat-field (discussed in section 5.1). This technique normalizes the response of pixels across the detector.

## 4.3 Electro-Optics for Satellite Observation

Rather than discussing the telescopes and detectors used by OSCOM in those individual sections, it makes sense to discuss them together. Telescopes and detectors act as a unit to provide images with particular characteristics, such as pixel scale and FOV. Just because a detector works well with a given telescope for one task does not mean it will work well for another. The goals of unresolved RSO photometry are different from those of high resolution imaging, and the equipment used by OSCOM for each of these tasks reflects that.

### 4.3.1 Unresolved photometry

Of particular interest to OSCOM is time-resolved photometry of unresolved objects. CubeSats may have pre-deployment spin rates of 0.5 to 1.5 Hz and therefore flash rates 4 times that (from each of 4 sides) [Graversen, Frederiksen, & Vedstesen, 2002]. To optically resolve these flashes requires frame rates of more than twice as fast and ideally even faster. Yet at the same time, these small satellites are only as bright as magnitude 11. These two requirements work against each other and force us to consider unique solutions. Additionally, OSCOM is currently located in Daytona Beach, Florida, where there is a bright sky background.

There have been several recent analyses of system design parameters for optical orbit determination [Coder & Holzinger, 2013; Ackermann, Zimmer, McGraw, & Kopit, 2015; Shell, 2010], but the author is not aware of any for optical characterization systems. The goals of each system are slightly different, with orbit determination emphasizing extremely large fields of view and high magnitude detection capabilities, but not the ability to time-resolve rapid events. For orbit determination systems, Coder and Holzinger [2013] found that under light polluted skies the system design is pushed towards large f-numbers and small pixel sizes to maximize the accuracy of initial orbital elements. Coder and Holzinger also suggested pushing the aperture diameter as far as the system budget allows in order to achieve high limiting magnitudes. Large focal ratios and small pixel sizes decrease the background noise while potentially increasing RSO position accuracy, but a system like this will likely also suffer from small fields of view, unless a very large detector is available. Ackermann et al. [2015] analyzed system design for GEO observation by trying to maximize both sensitivity (limiting magnitude) and search rate, a function of the field of view. The result was a large aperture, optically fast telescope—nearly the opposite of the system suggested by Coder and Holzinger. This difference likely results because most telescopes are located at dark sites, and Ackermann et al. probably assumed background sky levels would be low.

Shell [2010] performed a basic radiometric analysis to examine three space debris monitoring scenarios including ground-based optical observation of objects in LEO and GEO. Shell was surprised to find that a 20 cm scope could relatively easily detect LEO objects in the sub-10 cm size range. In fact, read noise dominated dark and sky noise with the short exposure times used for imaging objects in LEO. Sensitivity was slightly reduced for observations conducted with higher sky background, but his analysis used large  $24\text{ }\mu\text{m}$  pixels for increased detection capability.

## Signal-to-noise ratio estimation

Before discussing OSCOM's specific choices of equipment, it is helpful to show mathematically how the signal-to-noise ratio (SNR) of an imaged point source be estimated. Rather than performing a detailed radiometric analysis to model the system performance, this section will focus on trends that occur when varying system parameters. System design choices should be made to maximize the signal-to-noise ratio under certain constraints. For a simple electro-optical system, the signal-to-noise ratio of an RSO in an image can be expressed as

$$\text{SNR} = \frac{e_s}{\sqrt{e_s + e_b + e_n^2}} \quad (4.9)$$

where  $e_s$  is the number of detected source electrons,  $e_b$  is the number of electrons from background light, and  $e_n$  is the read noise of the detector. Dark current is not meaningfully present in short exposure times, so the only meaningful noise source from the detector is read noise. Background and source electrons each contribute uncertainty to the image photometry because of Poisson noise (Equation 4.8).

The number of point source electrons  $e_s$  measured in the detector is a function of the optic and detector and can be predicted by

$$e_s = \text{QE} \cdot \tau \cdot A \cdot E_s \cdot t \quad (4.10)$$

where  $\tau$  is the transmission efficiency of the optics and atmosphere,  $A$  is the aperture of the optic,  $E_s$  is the irradiance of the source, and  $t$  is the detector integration time [Shell, 2010]. It is important to note that the most flexible design parameters are the aperture area and exposure time. The focal length of the optic does not impact the source intensity when imaging a point source.

Background sky noise comes from natural air glow, light pollution, solar illumina-

nation, or moonlight. The sky is an extended source which creates  $e_b$  electrons in the detector, as modeled by

$$e_b = \frac{\text{QE} \cdot \tau \cdot \pi \cdot L_b \cdot x^2}{1 + 4(f/d)^2} t \quad (4.11)$$

where  $L_b$  is the background radiance,  $x$  is the pixel pitch, and  $f/d$  is the focal ratio [Shell, 2010]. This can be rearranged and simplified to

$$e_b \approx \text{QE} \cdot \tau \cdot L_b \cdot A \cdot \frac{x^2}{f^2} \cdot t \quad (4.12)$$

by approximating  $1 + 4(f/d)^2$  as  $4(f/d)^2$ . The important difference between the calculation of  $e_s$  and  $e_b$  is that the background is an extended object and therefore the number of background electrons is a function of the pixel size and focal length, essentially the pixel scale (IFOV).

## OSCOM Electro-optics

OSCOM's electro-optical system must meet several requirements listed in Figure 4.7. Meeting these requirements can generally be achieved by the EO system parameters given in the same figure. For example, to observe dim targets the aperture diameter  $A$  can be increased. This come directly from the SNR formulation above. Unfortunately, several of the possible solutions to achieving each of OSCOM's requirements are in direct conflict, e.g. long exposure times are better for observing dim targets, but short exposure times are necessary to time-resolve brightness fluctuations from a tumbling target. These types of conflicts needed to be balanced in order to meet all of the requirements.

Perhaps the most important requirement is the ability to observe targets as small and dim as CubeSats. This is the first requirement listed in Figure 4.7 and can be achieved by using a large aperture telescope, by using a long exposure time, or potentially by using a larger pixel scale to collect more source photons in a single pixel. The next require-

Optically track and observe CubeSats using COTS equipment from Daytona Beach, FL

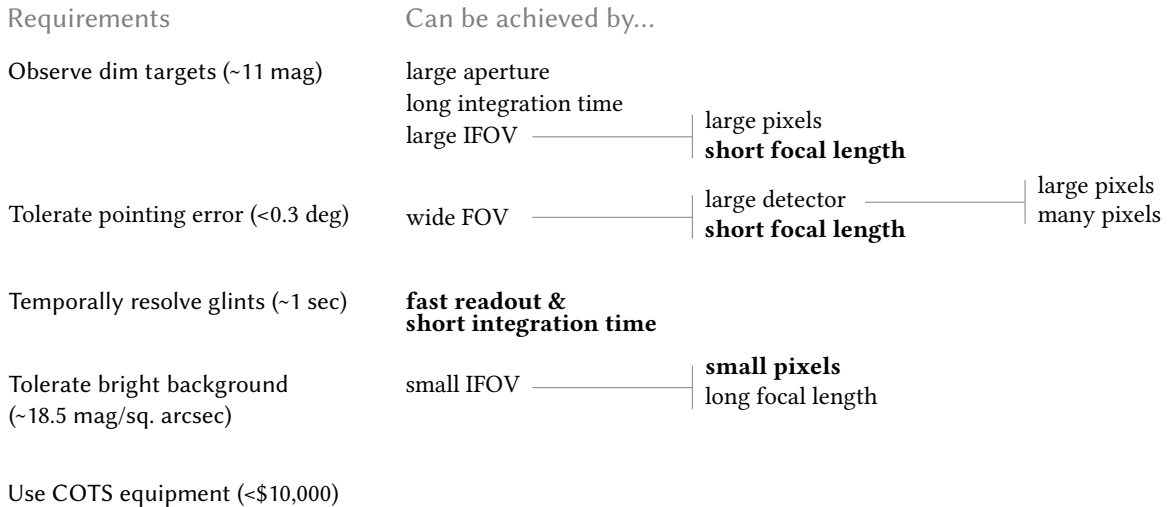


**Figure 4.7:** Each major requirement that the OSCOM electro-optical system must meet can be achieved by several combinations of optic and detector. However, in order to meet all of the requirements, including the use of COTS equipment, only those characteristics in **bold** text were chosen.

ment stems from several different uncertainties: error in the orbital elements of small debris and CubeSats, error in the OSCOM system computer time, and error in the telescope mount pointing. If these uncertainties are too large, the CubeSat will not be seen in the field of view of the EO system. To maximize the tolerance of the system, a large field of view can be used. Now that there is a theoretical system that can see CubeSats, the next requirement to add is the ability to temporally resolve glints and other rapid brightness changes that a tumbling satellite might exhibit. This is best accomplished by using short exposure times and fast readout detectors. This solution is also the first solution in conflict with another solution in the theoretical EO system design. There are several ways to observe dim targets, but only one way to time resolve glints, so short exposures will be a mandatory capability of the system.

The next challenge for the system is the ability to operate with the bright sky background found in Daytona Beach, Florida. To achieve this, the pixel scale of the EO system should be fairly small. This ensures that when the RSO is over a particular pixel, the background sky contributes very little to the same pixel. A small pixel scale can be

achieved by either small detector pixels and/or a long focal length optic. This is in conflict with the large IFOV solution of observing dim targets, but the situation is slightly more complicated. As the pixel scale decreases, the background contribution also decreases, but the read noise becomes more and more significant because the RSO signal will be distributed among a greater number of pixels. The seeing disk over Daytona Beach is roughly 2 arcsec on average, so an image of an unresolved RSO will be spread over 2 arcsec. This might be a slight overestimate because of the short exposure times used by OSCOM, but for the dimmest satellites which require  $t > 100$  ms, it is a fair approximation. Therefore, we aim for a system IFOV of about 2 arcsec/pix. Again, this can be achieved by varying the telescope focal length  $f$  and pixel pitch  $x$ .

The final system requirement is used to decide between long focal length or small pixel pitch: the use of affordable COTS equipment. There are many long focal length telescopes available in the amateur astronomy market, but very few detectors with both large pixels and a fast readout. On the other hand, there are many COTS CMOS sensors with fast readout and small pixels. If the EO system is going to have small pixels, the telescope should have a short focal length and large aperture, i.e. low focal ratio, in order to achieve the proper pixel scale of 2 arcsec/pix.

OSCOM ultimately chose to use the 11 inch Rowe Ackermann Schmidt Astrograph (RASA)  $f/2.2$  telescope made by Celestron. This variation on the Schmidt Cassegrain has corrective lens elements in place of the secondary mirror and the detector is placed at prime focus, as shown in Figure 4.8. At the time of this writing, an 11 inch RASA is available for only \$3500 in the United States. The RASA is current paired with a Manta G-235 CMOS detector made by Allied Vision. This detector has a 1/1.2 inch Sony IMX174 CMOS chip with  $5.86\text{ }\mu\text{m}$  pixels and 25 full frame per second capture rate. This rate is obtainable because the Manta is only a 12 bit detector. Data is then transferred over a gigabit ethernet cable at 117 MBps. The detector specification sheet claims a read noise of only  $6\text{ e}^-$ , but tests show OSCOM's unit actually does better than this. The

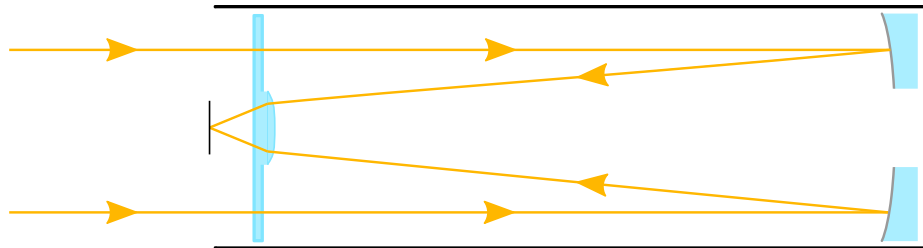


**Figure 4.8:** The Celestron Rowe Ackermann Schmidt Astrograph telescope uses a Schmidt corrector plate, spherical primary mirror, and corrective lens element at the prime focus.

Manta G-235 is currently available for about \$1200. The RASA/Manta system is pictured in Figure 3.4a.

The frame rate of a detector is limited by the number of detector pixels that must be read out. For high frame rates, there is a maximum number of pixels that can be read out before the detector clock rate limits the frame rate or the capacity of the data transfer cable is reached. With fairly small pixels, to minimize background sky noise, that also means the detector size will not be very large. When paired with a short focal length telescope, the FOV may then be described as “medium”: larger than most astronomical telescopes, but smaller than telescopes used for orbit determination or surveys. A very large field of view is not necessary because OSCOM’s purpose does not include searching for new or lost objects, but it should be large enough to accommodate pointing error. As a unit, the RASA/G-235 system has a FOV of  $1.05^\circ \times 0.66^\circ$  (shown in Figure 4.9) and a pixel scale of  $1.95''/\text{pix}$ .

Perhaps one of the most unusual aspects of this system compared to other satellite tracking systems is the decision to use a CMOS detector. Nearly all systems the author is aware of use CCD detectors. In part, this is because CCDs have high fill factor, high QE, and can have larger pixels, so they have increased sensitivity of a system for orbit determination. Unfortunately, CCDs also have a slow readout time that prevents their use in high rate imaging. Exceptions to this include the ML line by Finger Lakes Instrumentation that uses four separate amplifiers to read out the chip simultaneously at frame rates of about 4 Hz.

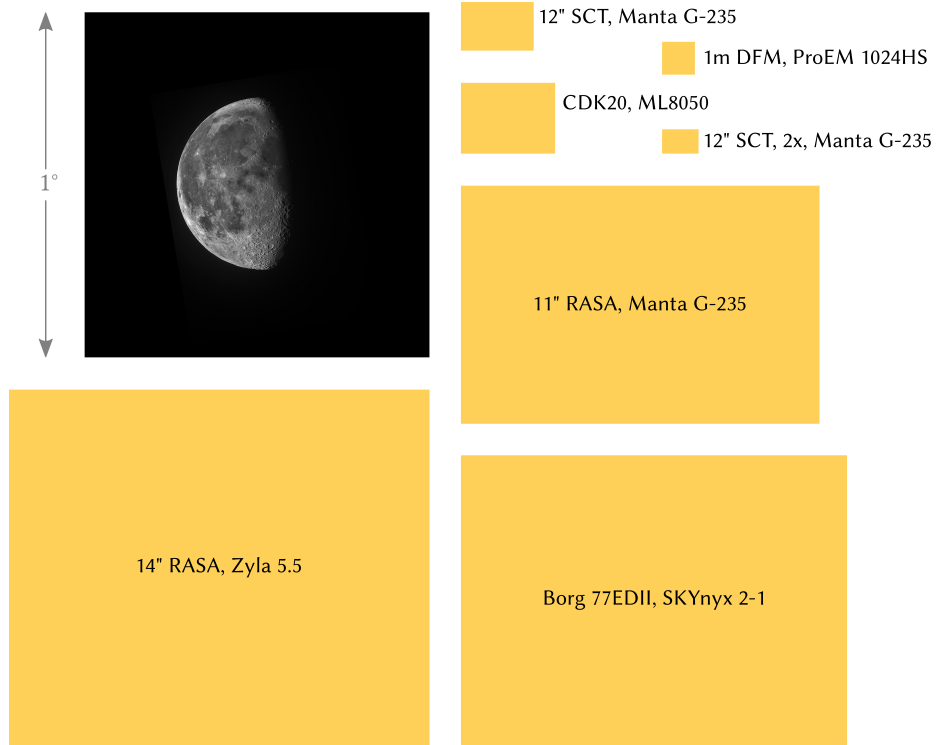


**Figure 4.9:** Field of views of several electro-optical systems evaluated for OSCOM. Labels are telescope, detector.

Some advantages of OSCOM’s RASA system for satellite observation is that the equipment is not very large or heavy, and thus is easily deployed in the field if necessary. Additionally, the short exposure times allow somewhat increased tolerance for tracking error. In turn, this eases the track mount requirements, reducing the tracking system’s total cost. The disadvantage of the  $f/2.2$  tube includes some difficulty with precise collimation. Fortunately, the focuser provided by Celestron provides precise control for the small critical focus zone of the fast optic.

The effective RSO magnitude limit using the RASA/G-235 system has not yet been reached. Satellites as small as 10 cm spheres (see Figure 6.4) have been consistently tracked. Orbital elements for objects smaller than this have not been available. Star tests have been performed to predict performance on dimmer satellites, but it was determined that atmospheric scintillation has a large impact on photometric variation over time. This is because OSCOM commonly uses exposure times that are similar to

the timing of atmospheric motion. Therefore, scintillation may be convolved with RSO photometry. This has the interesting effect that bright sources have high flux variability and dim sources have low flux variability such that the ratio of source brightness to variability is approximately constant for bright and dim sources. Additionally, this ratio only has a weak correlation with exposure length, although for the dimmest targets (magnitude 11+) it is advantageous to use relatively long exposure times of 100 ms or more. This is out of a necessity to provide a sufficient number of counts to be detectable by the photometry tool. With 300 ms exposures and a gain of 10 dB on the Manta G-235, photometry can be performed on sources as dim as 13 mag without significant difficulty.

If necessary, Embry-Riddle's Daytona Beach campus has a 1 m telescope (shown in Figure 4.10) which provides more photons per pixel for a given source than the RASA. However, because it has over 8 m of focal length, the field of view is very small. Wider field of view telescopes coaligned with the main telescope are used for acquisition and tracking of the RSO while the main telescope provides higher SNR science data. In the future, the 1 m telescope is likely a good platform for spectroscopy of dim RSOs because it provides a mechanically solid mounting surface and delivers a large number of photons to the instrument.

### 4.3.2 Spatial imaging

Although this is not OSCOM's primary focus, spatially resolved imaging of large RSOs can directly reveal their physical condition. Not only is this process useful for large LEO satellites, such as the International Space Station, but it can also be used to image a venting upper stage or debris from a satellite explosion or collision. High resolution spatial imaging requires long focal lengths and small pixel sizes in order to spatially sample the diffraction limit of the optical system. The RASA operates at  $f/2.2$ , but typically a telescope of at least  $f/20$ ,  $f/30$ , or higher is used for spatial imaging if possible. The difficulty is that as the angular resolution increases, the field of view decreases. Therefore,

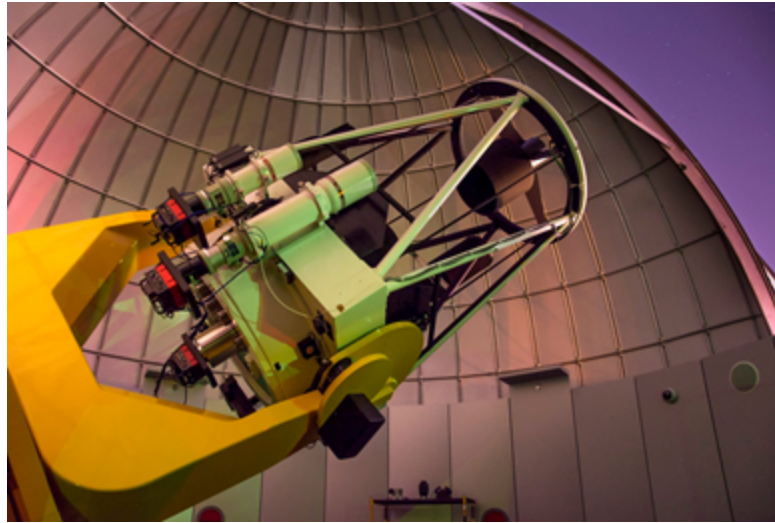


**Figure 4.10:** The DFM 1 m telescope at Embry-Riddle’s Daytona Beach campus. With over 8 m of focal length, the field of view is very small with most detectors. Several telescopes are co-aligned with the main telescope to provide a variety of fields of view. FROM observatory.db.erau.edu, COPYRIGHT MICHELLE BLAKE.

the pointing and tracking requirements become very steep. This is why OSCOM uses a wider field tracking telescope coaligned with the larger narrow FOV main telescope.

A sample OSCOM system for spatial imaging is shown in Figure 3.4b. This 12 inch setup is just one of several systems used for satellite observations. There have also been observations using a 20 inch CDK20 by PlaneWave and a 16 inch LX200 by Meade. In order to achieve higher effective focal lengths, a 2 or 3 $\times$  barlow lens is typically used. Either the Manta G-235, FLI ML8050, or Lumenera SKYnyx 2-1 or 2-0 are used as detectors. Each of these are capable of imaging at 4 FPS or faster and have pixels of 6  $\mu\text{m}$  or smaller. In all cases, OSCOM uses a Borg 77EDII refractor as the tracking telescope at  $f/4.3$ . When paired with a Lumenera SKYnyx 2-1, the field of view is  $1.12^\circ \times 0.84^\circ$ .

High resolution imaging through the atmosphere poses additional challenges, mostly caused by the atmosphere itself. In order to achieve sharp images, short exposure times must be used to prevent atmospheric blurring. Alternatively, expensive adaptive optics systems must be used to counteract atmospheric effects in real time. Generally, a significant amount of post processing is required for high resolution imag-

ing. This includes image selection, registration, stacking, deconvolution, etc. It is also important to remember that excellent collimation of the optical system is mandatory for the system to perform at its best. The particular optical tube being used for observations should also be of high quality, capable of providing a high Strehl ratio. Local thermal conditions and atmospheric conditions above the observatory site will also impact the effectiveness of a passive electro-optical system to make high resolution observations.

## 4.4 Optical filters

By placing color filters between the telescope and detector, the observer has much more control over what is being measured. Without a filter, the detector's QE curve effectively weights light of some wavelengths more greatly than others. This creates bias in photometric measurements. If an object changes color while maintaining its radiance, the detector would register a change in intensity. This can occur either by atmospheric reddening or a real color change. Without a well defined bandpass, it is difficult to know exactly what is happening. Filters restrict light to a small passband so that instrumentation and atmospheric effects can be easily removed from the data, leaving only the RSO color. Filters also reduce atmospheric dispersion effects, an important consideration for high resolution imaging. Most importantly, if an object is observed in two different filters, its color index can be measured, which aids in characterization.

There are many standard photometric filter sets, but OSCOM makes use of two: Johnson-Cousins/Bessel UBVRI [Bessell, 1990] and Sloan Digital Sky Survey (SDSS) u'g'r'i'z' [Fukugita et al., 1996]. The use of standardized filters allows data comparison with the larger community. Not only can standard tables of space material color indices be used for RSO identification, but more accurate comparison-star magnitudes be obtained from standard catalogs. The filter transmission curves for OSCOM's two photometric filter sets are shown in Figure 4.11.

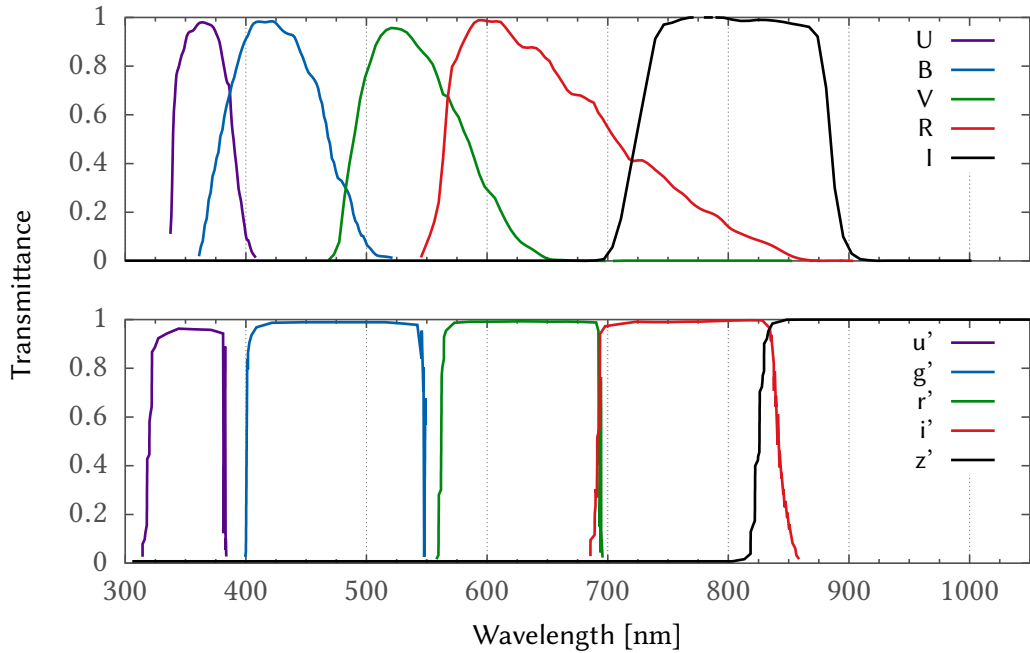


**Figure 4.11:** Johnson-Cousins/Bessel and Sloan Digital Sky Survey filter transmission curves. The atmosphere, detector QE, and optical system transmission efficiency all affect the actual wavelength response of the system. DATA FROM ASTRODON PHOTOMETRICS (<http://www.astrodon.com/>).

Occasionally, OSCOM uses special purpose filters. Because longer wavelength light is less affected by atmospheric effects, more stable, less distorted images result. In poor atmospheric conditions, it can be advantageous to use red or NIR bandpass filters to isolate only longer wavelength light. The downside is that the size of the diffraction disk increases for these longer wavelengths and therefore fine feature detail suffers.

Despite the advantages of isolated passbands, the image brightness suffers because less light is let through to the detector. For very faint objects, a wide band filter can be used. These are traditionally called clear or luminance filters by astronomers. Clear filters are clear glass that do little to block any light sensitive to the detector. Their primary role is to provide parfocal performance with other filters and help keep the detector clean. Luminance filters are traditionally UV/IR blocking. Silicon based detectors are sensitive past red light for nearly another 300 nm. Without blocking NIR, the profile of an unresolved RSO would have a wider full width half max from atmospheric

diffraction and dispersion. For imaging faint RSOs, the additional photons are usually preferred over the sharper image.

## 4.5 Telescope Mounts

Motorized mounts are required for moving the electro-optical system. This process is usually broken down into two parts: pointing and tracking. Pointing is the process of rotating the mount so that the optics are looking in a specific direction. Because fields of view can be very small, pointing must be accurate to within a few arcminutes across the entire sky. Tracking is the process of rotating the mount so that the optics follow a target at the correct rates and along the correct path. Traditional telescope mounts track at sidereal rate ( $\approx 15 \text{ arcsec/s}$ ) to compensate for Earth's rotation. They might also have the ability to track at lunar rates or rates of planets or asteroids that are close but not equal to the sidereal rate. To track LEO satellites, however, the mount must be capable of smoothly tracking between 0 and several degrees per second in both axes. Figure 4.12 demonstrates the approximate angular rate of a satellite with a particular orbit height and elevation above the horizon.

Most telescope mounts are made to very smoothly move at sidereal rate. Although they might have faster slew rates to quickly repoint the telescope, mount designers often do not plan for smooth tracking at 1 deg/s. Mount drives often have periodic errors in their gears, usually the worm gear because it is difficult to precisely make. If there is a “bump” in the worm, it will repeat every time the worm cycles past that point. A bump in the worm will cause the telescope to move slightly away from its nominal pointing position. These errors can add up every cycle of the worm. This can be reduced by training the mount and applying periodic error correction (PEC). PEC monitors the position of the worm and automatically adjusts the track rates to compensate for the worm error. This can help smooth out target motion on the focal plane array and

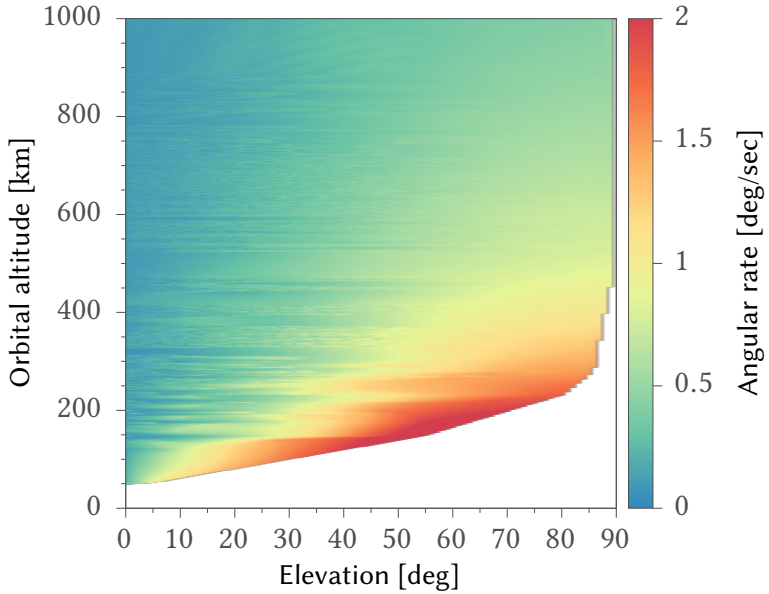


**Figure 4.12:** The orbit of 100 bright satellites and 100 CubeSats were propagated and access analyzed for Daytona Beach, Florida using STK software by AGI ([www.agi.com/products/stk](http://www.agi.com/products/stk)). Angular rates over the site were output with orbit altitude and elevation, which were then smoothed to produce this chart. It demonstrates the minimum range of mount rates required to track satellites in LEO.

reduce peak-to-peak errors by an order of magnitude.

Before a telescope can track a satellite, it must be pointing in the correct location. Tracking mounts either require alignment with north and a level base, or they must be calibrated to the sky once they are set up. For precision pointing of better than an arcminute across the sky, the entire mount and electro-optical system must be modeled. This is typically done using Tpoint Software<sup>1</sup>. Tpoint analyzes telescope pointing by looking at where a telescope actually points in the sky compared to where the telescope control system thinks it is pointing. A complete model consists of 200 to 300 star fields across the entire sky. Tpoint models polar misalignment, mechanical and optical non-orthogonality, lack of roundness in drive gears, and flexure caused by gravity. It fits all of these errors and suggests an optimal set of pointing corrections so that pointing errors are minimized across the sky.

More expensive COTS equipment includes absolute on-axis encoders. These en-

---

<sup>1</sup>[www.tpointsw.uk](http://www.tpointsw.uk)

coders monitor the true position of both axes thousands of times per second to ensure accurate pointing and tracking because the encoders are past the worm gear. Such an option usually costs an additional several thousand dollars per mount axis.

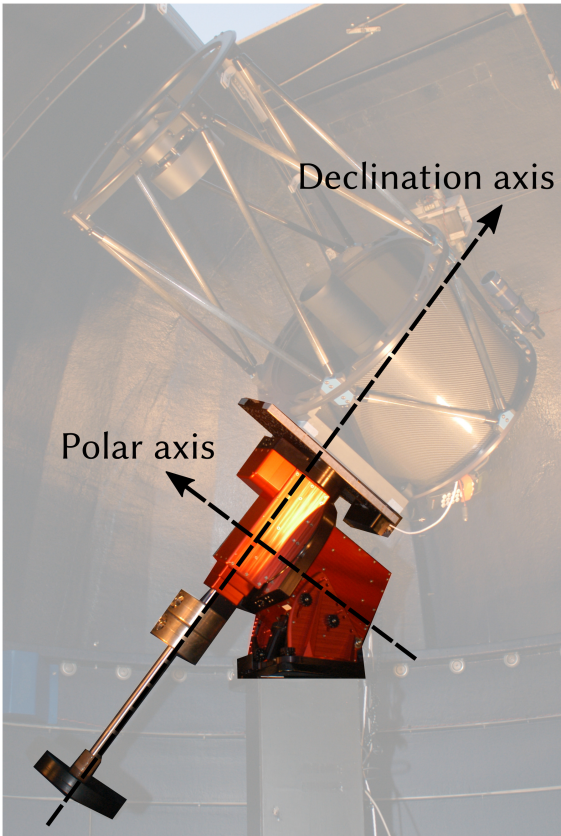
#### 4.5.1 COTS mount designs

COTS telescope mounts typically come in two different types: German equatorial (GEM) and altitude/azimuth (alt/az)<sup>2</sup>. German equatorial mounts are the more common among quality amateur class mounts. This is because GEMs are designed so that motion in only 1 axis is required to track stars. This reduces the chance for tracking errors and eases requirements on the mount manufacturer. This is accomplished by equatorial alignment—one of the mount axes is aligned with the north celestial pole and the mount rotation axes are aligned with the right ascension/declination coordinate system (see Figure 4.13a). Although such a design is convenient for tracking stars, it is not so good for tracking satellites. The mount axes are oriented inconveniently and GEMs are not capable of tracking through the meridian—the north/south line that divides the sky in half. This means if a satellite passes through the meridian, a GEM mount must stop, flip to the other side of the mount, and attempt to continue tracking. Unfortunately, this can take a considerable amount of time ( $\approx 60$  s).

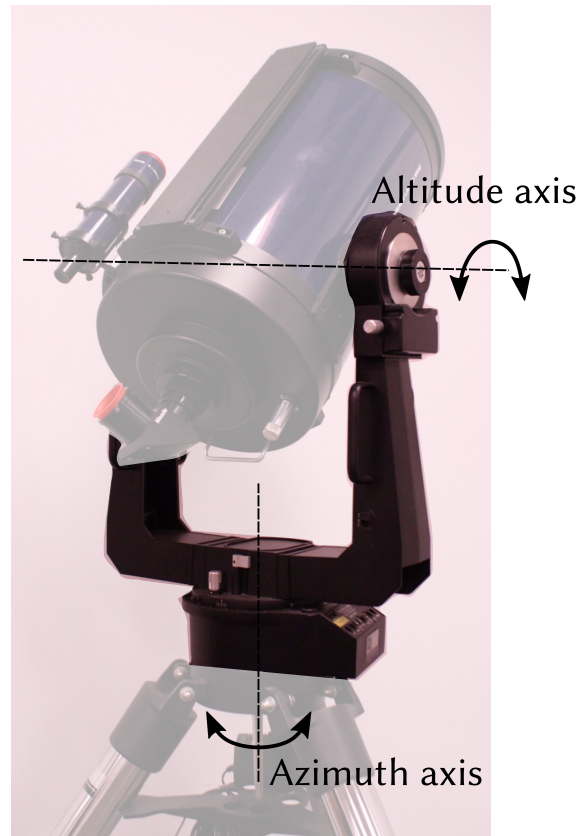
Altitude/azimuth mounts traditionally have two fork arms that support the telescope tube on both sides. This usually increases the payload capacity and stiffness of these mounts. As their name suggests, alt/az mounts have one axis rotating in azimuth and one axis rotating in altitude (see Figure 4.13b). This is fairly convenient for satellite tracking, which will require motion in two mount axes anyways, but it does suffer from a node at zenith. As an RSO passes near zenith, the alt/az mount must be capable of rapidly tracking in azimuth in order to continue tracking the RSO through the other side. Alternatively, some alt/az mounts can be configured so the entire telescope simply

---

<sup>2</sup>Also known as azimuth/elevation (Az/El).



(a) CDK20 on a Paramount ME German equatorial mount.



(b) Meade LX200 on an altitude/azimuth fork mount.

**Figure 4.13:** German equatorial and fork mounts are the two most common mount designs amongst amateur astronomers.

tracks through zenith with the elevation angle axis motors and continues tracking to the other side with the telescope tube upside down. This fork design can also be used in an equatorial mode if the entire mount is angled so that the line perpendicular to the azimuth axis is pointed at the north celestial pole. Unfortunately, there are not many motorized alt/az mounts available in the amateur astronomy market that are capable of smoothly tracking satellites.

OSCOM primarily uses Paramount ME and MX German equatorial mounts made by Software Bisque. This same mount is also used by the United States Air Force Academy's Falcon Telescope Network, the Defence Research and Development Canada Space Surveillance Observatory, and J.T. McGraw and Associates, LLC [Scott & Wallace, 2008;

Dearborn et al., 2011; McGraw, Zimmer, & Ackermann, 2014]. The reason for this is likely its solid performance over a range of track rates for only \$15,000 or less. Additionally, it is a U.S. based company, which might matter for some defense applications. Paramounts can track at up to 10 deg/s using an optional higher wattage power supply and track up to 2 hours right ascension past the meridian. The control software, TheSkyX, is tightly integrated with Tpoint, making it especially easy to produce pointing models for Paramounts. Typically all sky pointing accuracy of 30 arcsec RMS can be achieved. Software Bisque has recently introduced the Taurus mount, a fork style mount that does not suffer from mount flips. This convenience, as well as the added performance of absolute on-axis encoders costs about 4 times as much as the Paramounts.

# Chapter 5

## Data Reduction and Analysis

Although good raw data is a necessity for the best characterization performance, robust data reduction and analysis tools can extract and make sense of low signal to noise information. As described in section 3.1, there are several steps after an RSO is observed and the images saved on a computer. First, those images must be reduced or calibrated to remove optical system and sensor defects. Then, image “measurements” are made for photometry or spectroscopy and those measurements are further corrected for atmospheric and lighting effects. Finally, the corrected measurements are filtered and analyzed to produce information about the physical characteristics of the RSO. Spatially resolved images go through a slightly different process, as described below in section 5.5.

### 5.1 Image Reduction

OSCOM data goes through a fairly standard image reduction routine used by astronomers and satellite observers. Images are reduced using the PixInsight software<sup>1</sup> or OSCOM’s own Optical Satellite Analysis Toolset (osat) that makes use of the Python Astropy and affiliated packages [Astropy Collaboration et al., 2013]. Because of the large number

---

<sup>1</sup><https://pixinsight.com/>



**Figure 5.1:** A crop from a master dark frame created by averaging fifty 150 ms darks from the Manta G-235 CMOS detector.

of images usually recorded during a single satellite pass (1000–6000 as limited by the exposure time), both of these reduction tools support multi-threading to reduce the time required to correct the images.

To remove fixed pattern noise from the sensor, dark or bias frames are used. These are images taken by the sensor while the sensor is in darkness. This means everything seen in the images are from the sensor only. By recording many dark or bias frames, they can be averaged together to produce a master dark or bias that is largely free from read noise or cosmic ray events. These events can be explicitly rejected from the averaging process by using a sigma clipping mask to include only those pixels within a few standard deviations of the median value. A crop of a master dark image is shown in Figure 5.1. Some horizontal structure as well as hot pixels can be seen. All of these same defects are in every science image, so now that they are known, the master dark frame can be subtracted from every RSO image just as one would subtract one matrix from another.

OSCOM typically uses exposure times no longer than 300 to 500 ms. Therefore, even

though several of OSCOM’s cameras are not cooled, the dark current is negligible. This was confirmed for the Manta G-235, which is noticeably warm while imaging at high frame rates, by comparing darks at different exposure times and gain levels under different temperature conditions. Although by externally heating the camera with a lamp there was an increase in the background level when recording with 20 dB gain and 200 ms exposure times, this was not seen without external heating. Nonetheless, because the science frame exposure times are so short, it is easy to rapidly acquire dozens of these images. To err on the side of caution, dark/bias frames are usually taken at the same exposure time as the science image. The term “dark” and “bias” are used interchangeably to refer to these images.

Flat fields are used to correct for vignetting and pixel-to-pixel sensitivity variation. Flats are taken by imaging an evenly illuminated surface, or ideally the sky itself. These calibration frames are typically taken at dusk or dawn, before or after observations. An example flat field is shown in Figure 5.2. Each individual flat must be dark subtracted before they are all averaged together to make a master flat field. To prevent any background stars from making their way into the master flat, a strong kappa-sigma rejection mask may need to be used, similar to during the creation of the master dark. The master flat should reveal vignetting caused by the optical system. Vignetting is the reduction of image brightness from the center of the image out to the edges of the detector. Several factors affect vignetting, including the physical diameter of optical elements and baffling in the optical tube, but the net effect is that objects in the center of the FOV appear brighter than objects near the edge of the field. The master flat also measures the pixel-to-pixel sensitivity of the detector. If imaging an evenly illuminated source, one would expect two neighboring pixels to measure the same number of counts within the Poisson noise, but in many cases one pixel will be more sensitive than the other.

The master flat field is applied to the dark-corrected science images by division. The pixel array is normalized by the flat so that differences in optical system illumination

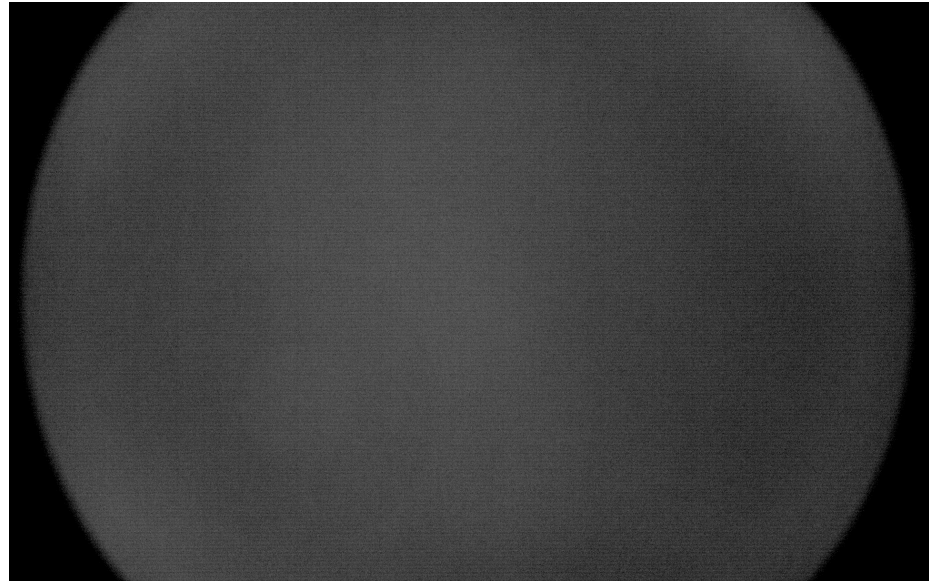


**Figure 5.2:** Master flat made by averaging 126 dark-subtracted flat fields. The C-mount on the Manta G-235 detector restricts light around the edges of the steeply converging light cone on the  $f/2.2$  RASA. A large donut-shaped shadow seen in the bottom left corner is caused by a single out-of-focus speck of dust.

and pixel sensitivity are removed.

## 5.2 Photometry

Photometry, or really radiometry, is the measurement of how bright an object is. As discussed in section 1.2, by measuring the brightness variation in an RSO over time, the shape or attitude of an RSO can be estimated. The calibrated brightness can suggest how large the object is, and when the brightness is known in several color bands, the RSO materials can be estimated. Astronomers have long used photometry for determining physical characteristics of stars, asteroids, active galactic nuclei, and more recently, exoplanets. Satellite observers have borrowed many of the techniques already developed by astronomers.

Traditionally, astronomers use a technique called aperture photometry to measure the flux from an object in their image. The position of the science object on the image is determined and a circle is drawn around it with radius  $r_{\text{ap}}$ . This circle is known as an

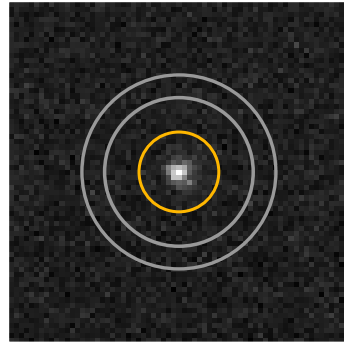


**Figure 5.3:** The yellow circle represents the aperture drawn around the science object. The sky annulus is identified by the two gray circles.

aperture. The aperture should be large enough so that it contains most of the light from the science object, but is not so large that background sky noise begins to influence the measured flux. Typically,  $r_{\text{ap}}$  might be chosen as 1.5 to 2 times the FWHM of the science object (assuming that object is a point source). An annulus is then drawn around the aperture. A picture of the aperture and sky annulus is shown in Figure 5.3. This ring, with inner and outer diameters of  $r_{\text{sky,in}}$  and  $r_{\text{sky,out}}$ , respectively, is used to measure the background sky level so that it can be subtracted from the measurement of the science object aperture flux to determine only the contribution from the science object. In other words,

$$f = N_{\text{ap}} - B \times A_{\text{ap}} \quad (5.1)$$

where  $f$  is the science object flux,  $N_{\text{ap}}$  is the number of counts in the aperture,  $B$  is the background sky level, and  $A_{\text{ap}}$  is the area of the aperture. It is then necessary to go from these linear units of flux to magnitude using Equation 2.2 or

$$m = -2.5 \log_{10} f. \quad (5.2)$$

The resulting magnitude is called the instrumental magnitude because the values are valid only for that individual frame. The system must be calibrated by observing standard stars to put all of the magnitudes onto the stellar magnitude scale.

### 5.2.1 Source detection

Before photometry can be performed, it is necessary to center the aperture on the source. This occurs as two steps, source detection, and then fine centering. OSCOM's reduction and analysis toolset osat can support several different detection methods.

Up to now, the most commonly used method has been to preprocess the images using `ntrackonpointo.npy`, an osat tool for centering and cropping a set of images on a source. `ntrackonpoint` loads a time series of images and lets the user select the source on the first frame. It then makes use of `ncv2o.nSimpleBlobDetectorp()` to detect the source in a ROI on the next frame, updates the ROI position, and continues. For each frame, it saves a new cropped image centered on the source and writes the pixel position of the source to a text file. The new folder of cropped images saves on average 2 orders of magnitude of hard drive space. This allows the full frames to be archived on an external storage device while analysis can continue on a standard laptop computer.

The `nphotometryo.npy` module of osat optionally uses the `daofind()` algorithm, image segmentation with `ndetectsourcesp()`, or local peak detection with `nfindpeaksp()` of Astropy photutils<sup>2</sup>, or coordinates provided by a file. DAOFIND is an algorithm well known by astronomers that searches the image for local density maxima with a peak amplitude exceeding a specified threshold and with a size and shape similar to a defined 2D Gaussian kernel [Stetson, 1987]. DAOFIND provides subpixel centroiding, which is important for large pixel scale.

Image segmentation is similar to a blob detector. Every group of a minimum of  $n$  neighboring pixels that all exceed a specified threshold is labeled as a source. This can be prefiltered with a specified kernel to enhance image features that resemble the expected RSO shape. Typically for a point source, this will be a 2D Gaussian kernel, although the true PSF of the optical system at the observation time could be used, or if there is consistent motion blur resulting in an elliptical shape, that could also be used.

---

<sup>2</sup>[photutils.readthedocs.org](https://photutils.readthedocs.org)

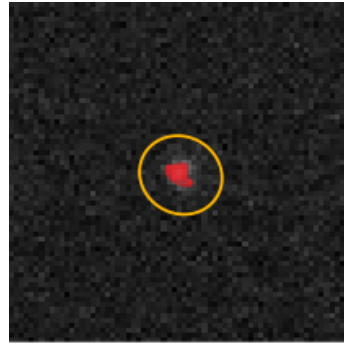


**Figure 5.4:** The red colored pixels exceed the threshold criteria and are labeled as the source. A yellow elliptical aperture is then defined around the source based on the segment properties.

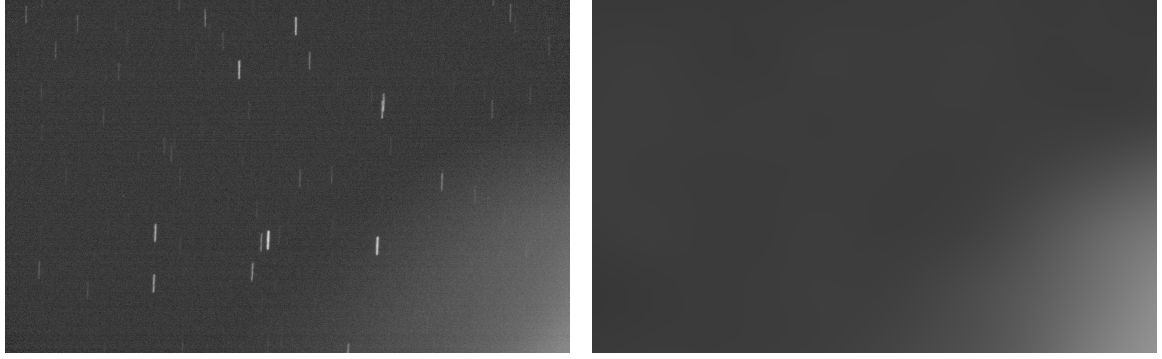
The segment properties can then be used to define an elliptical aperture around the source, as shown in Figure 5.4.

Local peak detection is a simple algorithm that finds peaks in an image that exceed a threshold and only occur within a minimum distance from one another. To achieve subpixel precision, an ROI is centered on the peak and fit with a 2D Gaussian. When images are preprocessed and cropped, this is the easiest technique to use because the cropped image usually only contains background and one round point source. It will only fail for an image if a bright star passes very near the RSO.

OSCOM's osat tool allows a great deal of flexibility in choosing and even combining these detection algorithms. For example, if pixel precision coordinates are provided by a file, the user may optionally select to also perform a subpixel centroiding. OSCOM also allows a small ROI mask to be preapplied to the center of each image before the detection algorithms are run. This reduces the likelihood of detecting a background star rather than the RSO.

### 5.2.2 OSCOM photometry

Just as osat provides several options for source detection, it also provides a couple of options for performing photometry on the source. Unlike in traditional aperture photometry, which uses the median or mode of pixel counts in the sky annulus as the back-



(a) Full frame with background gradient

(b) Extracted background map

**Figure 5.5:** This full frame taken from an observation of the POPACS-2 nanosatellite is not only filled with trailing stars, but suffers from a strong background gradient in the lower right corner. This can be robustly extracted from the image and subtracted before source before aperture counts are summed.

ground value, OSCOM makes use of photutils robust background extraction tools. Two separate methods are implemented. Assuming a cropped image is being processed, there will likely be little background variation across the image. The background level is estimated using the sigma-clipped median value. The background RMS is estimated by the sigma-clipped standard deviation. Before photometry is performed, the background is subtracted from the image.

If a full uncropped image is used, there may be background variation across the image from light pollution or the moon. This is especially likely given the large field of view optics used for OSCOM photometry. In this case, a background map is fit to the image. The image is divided into subregions and a sigma-clipped median is calculated for each. This low-resolution background is then median filtered to reduce local over or underestimations. This low resolution background map is then resized to the full resolution image using a bicubic spline interpolation. An example of this is shown in Figure 5.5. This background map is then subtracted from the image before pixel counts in the aperture are summed.

The summing of source counts is ultimately performed in two different ways, with an aperture or with image segmentation. The aperture photometry method draws an

aperture around the source, and sums up the pixel counts inside the aperture. The aperture is drawn using the detection methods explained above, including using image segmentation to define an aperture. Image segmentation may also be used directly to measure the flux from a source. This is especially useful for just barely resolved objects or objects with significant blurring on the focal plane array. Just as for osat’s reduction modules, both the aperture and image segmentation photometry functions are multithreaded using the `multiprocess` Python package in order to reduce the processing time on several thousand images [McKerns, Strand, Sullivan, Fang, & Aivazis, 2012].

The whole photometry process begins when the user defines some simple information about the satellite and parameters for the photometry. For example:

```
nsatname o= l+s+s1SPINSAT [20160301]
nsat o= nSatelliteObservationp(nnnameo=nsatnamep)
nsato.nsetobsp(ncreeksidelatp, ncreeksidelonp)
nsato.nreadtlefromfilep(ntlepatho+l+s+s1/sat.tlep)
nparams o= nphotometryo.nPhotParamsp(ndetectionthresholdo=l+m+mf1.5p,
→ ngaino=l+m+mf0.138p, nfwhmo=l+m+mf2.4p, nfinecenteringo=k+kcTruep,
→ nbackgroundmapo=k+kcFalsep,
→ nradiao=p[l+m+mi3p, l+m+mi4p, l+m+mi5p, l+m+mi6p])
nparamso.ndetectionmethod o= nphotometryo.nDetectionMethodo.nfindpeaks
```

The instrumental photometry is then performed with

```
ndfp, nsatp, nparamsp, ntlepatherp, nsatname o=
ninstrumentalp(nsatp, nparamsp, ntlepatherp, nsatnamep)o.
```

## 5.3 Photometry Corrections

The output of the photometry process is a file of source instrumental magnitudes, the associated magnitude error, and the time of the observation. By plotting these magnitudes against time, we have a lightcurve describing the RSO brightness as measured by the electro-optical system. The instrumental magnitudes, however, do not account for atmospheric extinction, satellite range, or changing illumination geometry throughout

the pass. These effects must be corrected in order to understand how the RSO brightness is truly changing.

Each correction is completely independent and therefore the order in which they are performed does not matter. To correct for the satellite slant range, the orbit of the satellite must be known. Currently OSCOM uses the nominal orbital elements, e.g. the TLE, to provide the range data. As described by Africano et al. [2005], the apparent brightness of the RSO can be normalized to a standard distance  $R_0$  (1000 km for objects in LEO), by the relation:

$$M = m - 5 \log_{10} \left( \frac{R}{R_0} \right) - 5 \log_{10} \left( \frac{R_{\text{sun}}}{R_{\text{sun}(1 \text{ au})}} \right) \quad (5.3)$$

where  $M$  is the range corrected magnitude,  $m$  is the instrumental magnitude,  $R$  is the slant range,  $R_{\text{sun}}$  is the satellite distance to the sun, and  $R_{\text{sun}(1 \text{ au})}$  is the average Earth distance to the sun, i.e. 1 au. The latter term is negligible for LEO satellites.

Satellite observations occur over a wide range of airmasses. The atmospheric extinction over these ranges can vary by nearly 2 mag. In order to correct for this, an extinction coefficient defined by the optical and site atmosphere characteristics must be determined. This value varies night to night, and so calibration observations of standard stars at multiple airmasses must be taken around the time of satellite observations each dawn or dusk observation. Strictly speaking, extinction is a color dependent correction, but OSCOM currently ignores this term. The actual correction is given by:

$$M = m - kX - c(\text{CI}) \quad (5.4)$$

where  $m$  is the instrumental (or range corrected) magnitude,  $k$  is the atmospheric extinction coefficient,  $X$  is the airmass,  $c$  is the color-correction term, and CI is a color index, e.g.  $B - V$  for observations in  $B$  or  $V$  filters. A typical value for  $k$  is between 0.2 and 0.3. In order to minimize required observation time and reduce time spent on im-

age reduction, OSCOM does not generally solve for  $k$  with standard star observations. Instead, OSCOM uses the pyExtinction package, which predicts atmospheric extinction above a site based on Rayleigh attenuation, ozone absorption, and aerosol extinction as described in Buton et al. [2012]. The atmospheric parameters entered into the model can be retrieved by the analyst from NASA's Earth Data Giovanni portal<sup>3</sup>. A normalized multiplication of the solar spectrum and detector QE is used as the wavelength weighting factor on the model output. These models are not perfect, but high precision photometry is not currently necessary for satellite observations. Satellites typically exhibit large fluctuations in magnitude exceeding 10%, and satellite attitude and shape determination algorithms are not yet good enough to require better photometry. OSCOM does not currently provide a technique for precisely zeropointing magnitudes to the stellar magnitude scale.

The impact of both range and airmass correction on an instrumental magnitude light curve is shown in Figure 5.6. The sky position and slant range to the satellite during the pass is shown in Figure 5.7. As the satellite set in the southwestern sky, not only were background sky counts increasing, but the slant range was increasing as well. This decrease in signal to noise ratio is evident in the increased spread in the light curve. The instrumental magnitude is also low and decreasing at the end of the pass, as expected due to extinction and the inverse square intensity reduction. The range correction curve has brightened the RSO by about 2 magnitudes at the end of the pass.

It is also possible to normalize illumination conditions. This is traditionally done by assuming the satellite is a diffuse sphere with a brightness as predicted by Equation 2.3 and Equation 2.6 [Roh et al., 2015]. The problem with this approach is that true shape and BDRF information is being destroyed. In fact, this correction is like changing the shape of the satellite. Instead, OSCOM light curves can be plotted against phase angle to possibly reveal information on the satellite shape. Although as discussed in

---

<sup>3</sup><http://giovanni.gsfc.nasa.gov/>

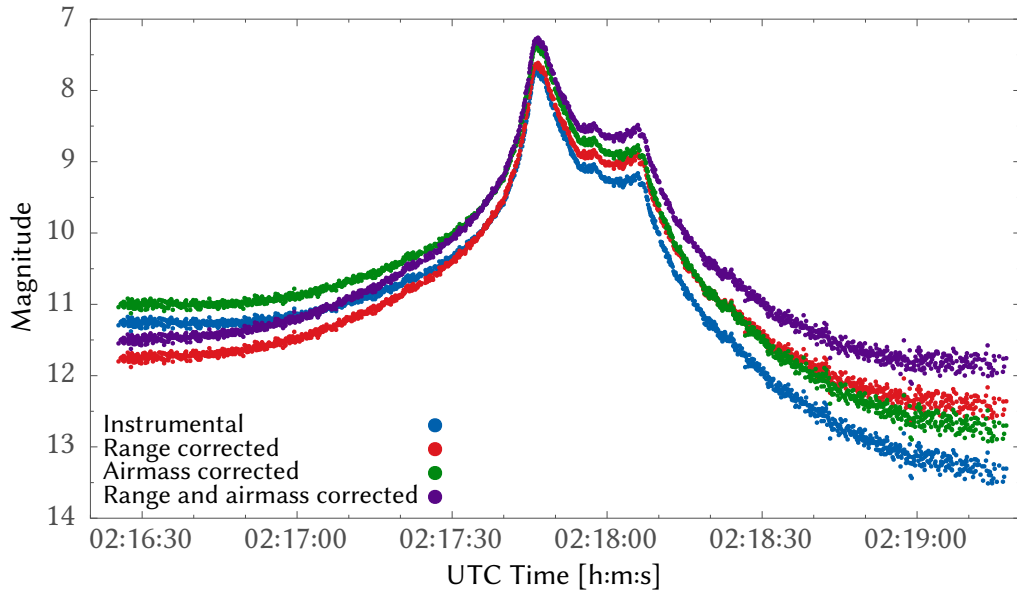


**Figure 5.6:** The microsatellite OPAL was observed by a field deployed OSCOM system on July 31, 2015. The raw instrumental light curve (blue) shows a 2+ decrease in brightness by the end of the pass due to atmospheric extinction and increased slant range. Correcting for both of these effects (purple) shows OPAL was only slightly dimmer at the end of the pass than the beginning. Phase angle corrections were not performed.

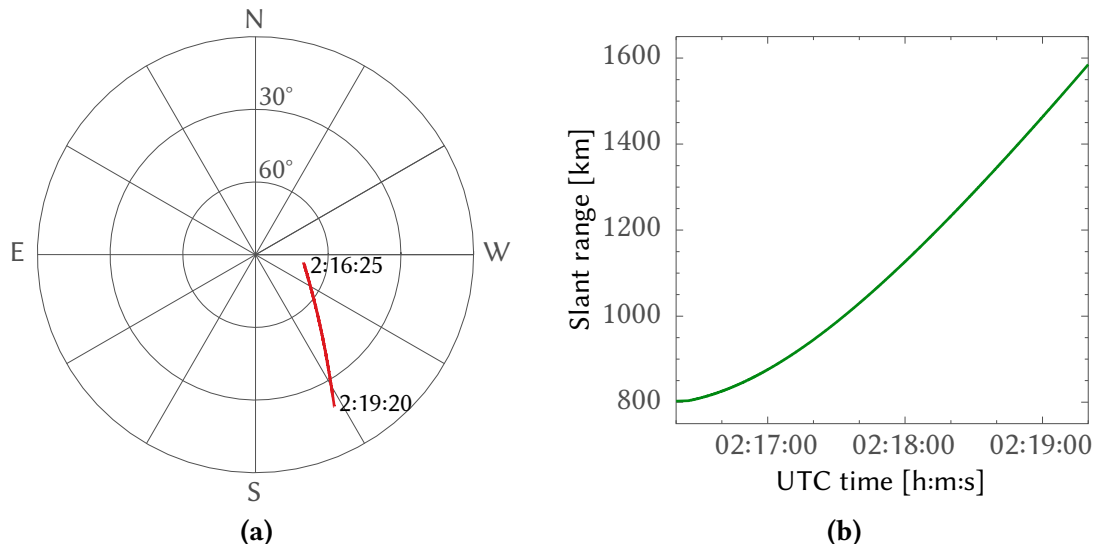


**Figure 5.7:** (a) OPAL's position in the sky during the July 31, 2015 pass. (b) The slant range between the observation site in Needham, MA and the satellite.

subsection 2.2.1, a single angle is insufficient to fully characterize the satellite shape or attitude.

To apply all of these corrections, the analyst simply evokes the following command in osat:

```
ndfp, nselectradii o= ncorrectionsp(ndfp, nsatp, nparamsp, ntlepathp,  
→ nsatnamep)
```

## 5.4 Photometry Analysis

The corrected light curve of an RSO may include particularly noisy data when the satellite is low to the horizon or if a star passed next to the satellite for one frame and was accidentally included as part of the source counts. It is also possible that the RSO becomes so dim that the detection algorithms are unable to centroid on the source. In any of these cases, the data points should be removed from the set so that they do not artificially influence any further analysis. The analysis, periodogram, and photscript modules of osat all contribute functions to this data reduction, filtering, and analysis process.

### 5.4.1 Filtering data

The simplest data cleaning method is to reject data points with magnitude thresholds. If a satellite appears to be no brighter than 10.8 mag during a pass, an analyst might choose to consider anything brighter than this an outlier. In Python, this is easily accomplished with the command

```
noutliers o|= ndfp[nmagp] o l+m+mf10.8
```

where outliers is a data series of outlier data points and df is the DataFrame of photometry data. The beginning or end of dataset may be clipped in a similar way, replacing ndfp[nmagp] with ndfo.nindex.

In many cases more dynamic rejection techniques are required. One such case shown in Figure 5.8. The bright specular reflection occurring just after 10:16:00 UTC prevents the use of a blanket threshold for rejecting outlier points. To get around this, a sliding median absolute deviation (MAD) algorithm is used. MAD is the median of the absolute difference between each value in an array and the median of the array. For example, for the array  $x = [4, 5, 11, 8, 9]$ , the median value is 8 and the absolute deviations from the median are  $[4, 3, 3, 0, 1]$ . The median absolute deviation is therefore 3. The reason for using such a measure is its robustness against outliers. To help handle the rapid and extreme changes that an RSO might exhibit in its brightness, a rolling median is used with a window size that must be selected by the analyst based on characteristics of the light curve. Outlier points can then be rejected if they exceed a threshold number of absolute deviations from the local median above the rolling MAD.

We calculate the absolute deviations from the median magnitude with

```
nresid o= n+nbabs(ndfp[nmagp] o npdo.nrollingmedianp(ndfp[nmagp],
→ nwindowsizep))
```

and the rolling MAD with

```
nrollingmad o= npdo.nrollingmedianp(n+nbabs(ndfp[nmagp] o
→ npdo.nrollingmedianp(ndfp[nmagp], nwindowsizep)), nwindowsizep)
```

Rejected points are those that satisfy the criteria

```
nrejects o= nresid o nkappa*nrollingmad
```

A plot of the residuals and rolling MAD are shown in Figure 5.9. Residual values that exceed the rolling MAD criteria are removed from the dataset.

The residuals and rolling MAD of the rolling MAD rejection algorithm is not very smooth and can sometimes reject good points. OSCOM has also used an exponentially weighted moving average to reject bad data. This filter is smooth but lags behind the curve and therefore wrongly rejects sharp peaks. FFT-based filters have also been ap-

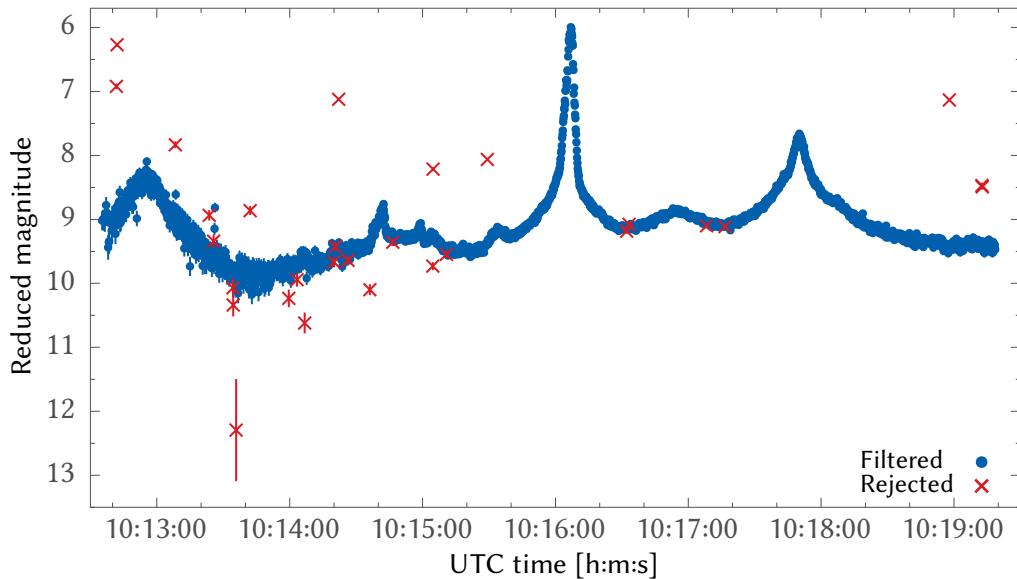


**Figure 5.8:** Reduced light curve of the DANDE microsatellite observed by OSCOM on January 18, 2016. Points marked with  $\times$  were rejected by a sliding median absolute deviation algorithm used to reject bad data points.

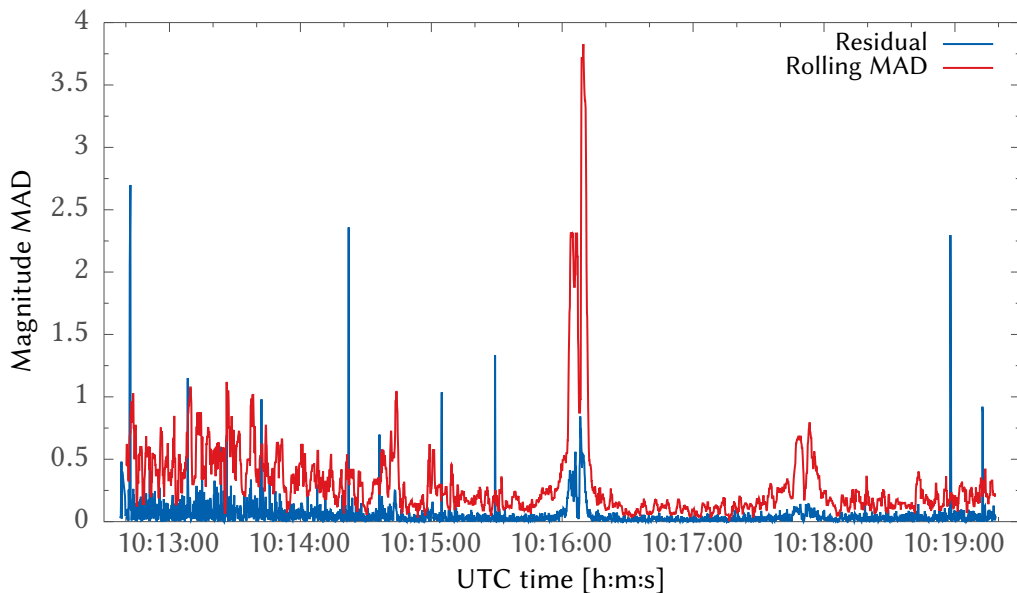


**Figure 5.9:** Photometry data (blue) exceeding the 7 MAD criteria (red) are rejected from the dataset.

plied. The analyst can choose to combine several of these techniques, removing different outliers each time. After identifying outlying points, they are removed from the dataset with the command `ndf o= ndfp[onoutlierspl]`. Future development will hopefully include more intelligent algorithms that can be applied without human intervention.

### 5.4.2 Period analysis

One of the most basic and useful indicators of a satellite's status is whether or not it is 3-axis stabilized or spinning, and if so, then at what rate is it spinning? The flash period, i.e. the period between observed flashes, of a satellite can be used to determine the rate at which the satellite is spinning, at least for RSOs of simple shape. Even if this rate does not represent the true spin rate of an RSO, it can be used for detecting a change in spin or orientation over time.

Traditionally the fast Fourier transform (FFT) algorithm is used to convert time domain signals to the frequency domain. The FFT, however, usually requires a power-of-two number of inputs and more importantly, requires evenly spaced samples. Although this is approximately true, the frame rate of the cameras partially depends on the memory and drive speed of the image capture computer. That rate may not be consistent during an observation, especially when a memory buffer fills and must write to the drive. Therefore, a least squares spectral analysis (LSSA) technique is used. OSCOM's `osat` package includes several Python implementations of the Lomb-Scargle algorithm, as provided by `astroML` and `gatspy` [Vanderplas, Connolly, Ivezić, & Gray, 2012]. Given a frequency grid, Lomb-Scargle computes the power at each frequency from a decomposition of the input time series into a linear combination of sinusoids [Lomb, 1976; Scargle, 1982].

An example of a fairly noisy light curve is shown in Figure 5.10. The satellite, DICE-2, is a 1.5U tumbling CubeSat that was observed at 8 frames per second using the 11 inch

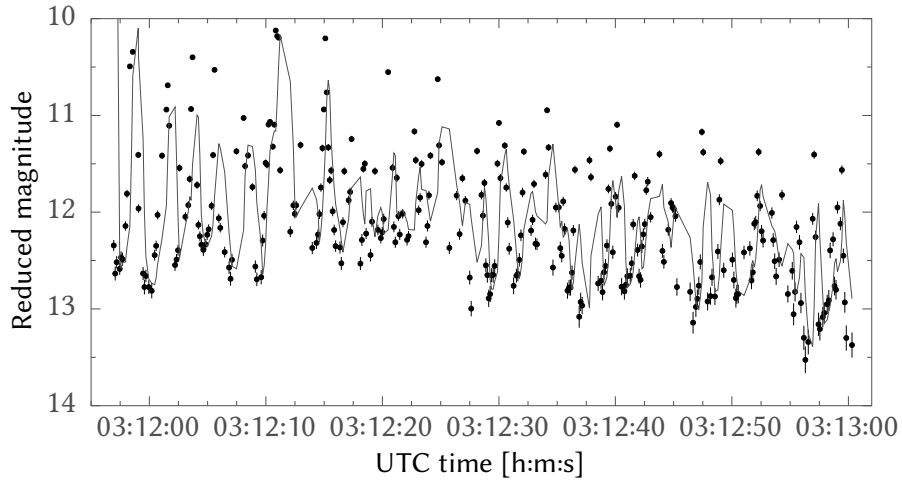


**Figure 5.10:** The 1.5U DICE-2 CubeSat was observed with the 11 inch RASA on July 27, 2015 using just 125 ms exposure times and 0 dB gain on the Manta G-235 detector. The resulting light curve is noisy, but shows signs of periodicity as highlighted by the gray line trace of a 3-sample moving average.

RASA telescope. It has several deployable antennae that create the 2 magnitude flashes. By performing a Lomb Scargle periodogram, shown in Figure 5.11, the dominant flash period is determined to be 2.41 s followed by 1.05 s and 3.22 s. The difference in these periods could be matched to the physical geometry of DICE-2 with its antennae deployed to attempt to establish the spin rate of the satellite.

## 5.5 Processing Resolved Images

The purpose of processing resolved images is to be able to directly see physical features of an RSO. To do this, an image must display fine detail with good contrast. Quality, thermally equilibrated optics, stable skies, and sampling of the diffraction limit are required for the most detailed images. Post processing techniques can be used to enhance the images further. Without an adaptive optics system, rapid imaging techniques are best suited to beat atmospheric effects. These images must be sorted to determine which are not distorted by the atmosphere. If the single frame signal-to-noise ratio is low, adjacent frames may be registered and co-added to increase the SNR.

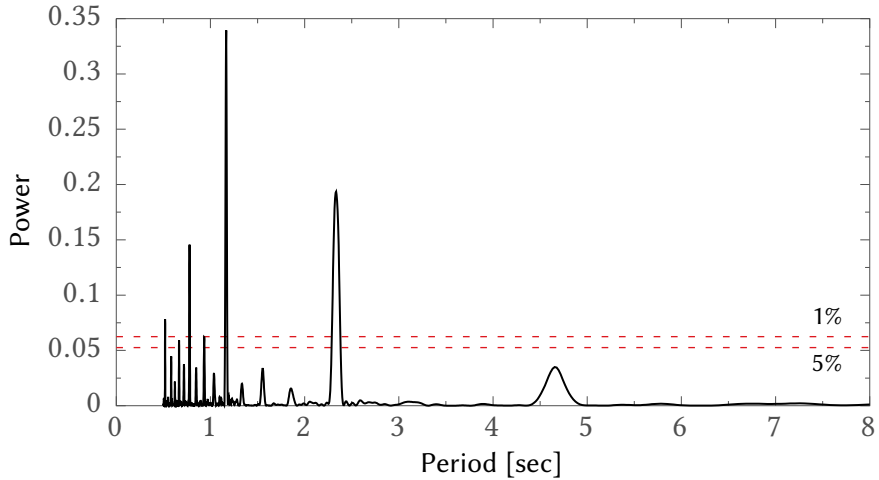


**Figure 5.11:** A Lomb-Scargle periodogram was computed for the DICE-2 photometry shown in Figure 5.10. The algorithm determined a statistically significant peak at 2.41 s and possibly 1.05 s and 3.22 s. Significance levels are computed using bootstrap resampling.

Frame selection techniques fall into two categories. One is based on the image brightness, with the theory that images with higher peak histogram values or total pixel values occur at moments of stable seeing. Although this works for stellar or planetary imaging, satellites are usually too dynamic for this to be effective. The second major technique is based on maximum gradient or sharpest edge. Here the theory is that sharp transitions or high contrast images will also contain the most detail. These algorithms can be easily coded in Python or another language, or used directly in programs such as Planetary Image PreProcessor<sup>4</sup>.

Adjacent frames can then be aligned, e.g. using an FFT technique, and co-added, or single frames of the highest quality can be selected from the set for further processing. The first processing step is typically deconvolution. Image deconvolution is a popular technique for deblurring, removing atmospheric degradation, correcting some optical aberration, and generally sharpening the image. Although blind deconvolution methods exist, it is easy to sample the actual PSF of the system by observing a star. By using short exposure times and sorting the resulting images by quality, a stable image of the point source star can be used as the deconvolution kernel applied to the RSO. A sample

---

<sup>4</sup>[sites.google.com/site/astropipp](http://sites.google.com/site/astropipp)

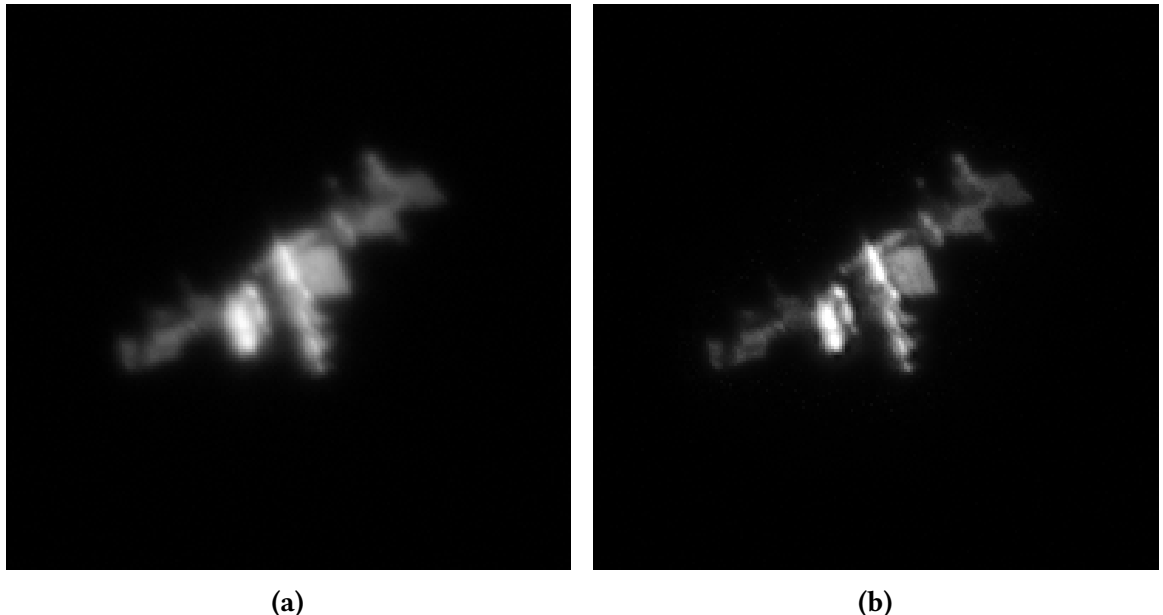


**Figure 5.12:** The International Space Station imaged on April 2, 2015 by the CDK20 and ML8050 in I band. The single 50 ms exposure (a) is significantly sharpened by applying a Van Cittert deconvolution (b).

of the Van Cittert deconvolution algorithm applied to a single frame of the ISS is shown in Figure 5.12.

Additional algorithms, such as wavelet transforms or unsharp mask, can also be used. These techniques enhance features at certain spatial scales. By properly selecting these scales, contrast of features on the RSO can be increased.

# Chapter 6

## Observations

The OSCOM system has been used to conduct spatial or photometric observations of more than 60 unique satellites of all sizes between spring 2015 and 2016. An additional 43 repeat observations were also made for several of the satellites. This chapter presents a subset of time-resolved photometry, the primary data product of OSCOM at this time. Every data set is corrected for atmospheric extinction and is shown at a normalized slant range. The magnitudes of each set are shifted by a constant value so that they roughly correspond with the apparent stellar magnitude of the observed satellite. Error bars represent the single-image error in the photometry aperture sum. This error includes the variation in the extracted image background and Poisson noise from the summed pixels (see <http://photutils.readthedocs.org/en/latest/photutils/aperture.html> for details). Some light curves are shown with moving average lines to support the visualization of trends. Data is categorized by the satellite wet mass category.

Satellite mission and design information is from [directory.eoportal.org](http://directory.eoportal.org) unless otherwise stated.

## **6.1 Large Satellites**

Large satellites have a wet mass of more than 500 kg.

## DMSP-5D2

The Defense Meteorological Satellite Program (DMSP) provides meteorological data for the United States Department of Defense. Two satellites from block 5D2 have been observed. Satellite F7 is currently stable but inactive, while satellite F12 is tumbling in orbit. This difference is clearly visible in their light curves.



FROM space.skyrocket.de

Name	Launch	EOL	Orbit [km]	Size [m]	Mag
DMSP-5D2 F7	Aug 1994	Oct 2008	835	6.4 × 9.3	7
DMSP-5D2 F12	Nov 1983	Oct 1987	800		5

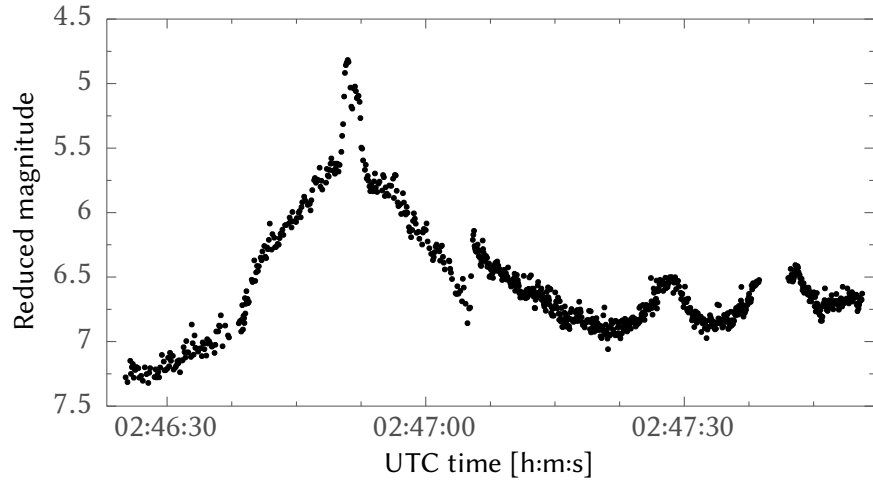


**Figure 6.1:**  
DMSP-5D2 F7  
June 20, 2015  
Needham, MA  
RASA/G-235  
105 ms

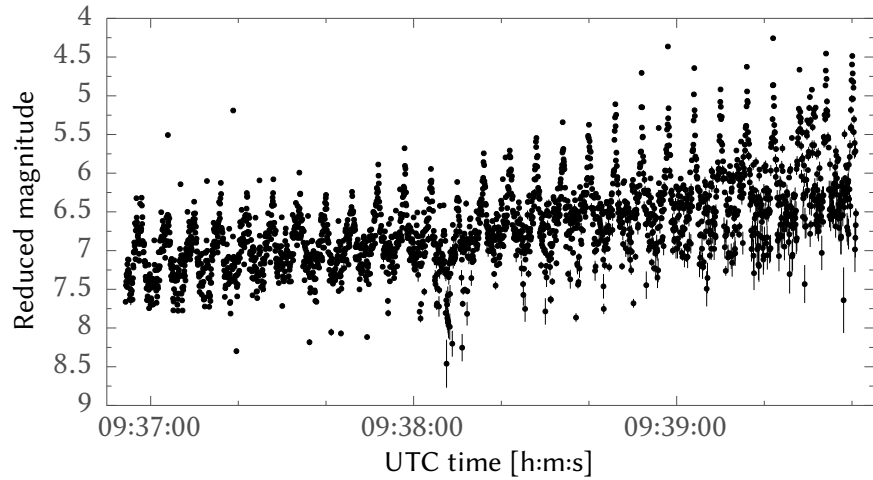


**Figure 6.2:**  
DMSP-5D2 F12  
April 1, 2015  
Daytona Beach, FL  
Borg/SKYnyx 2-1  
31 ms

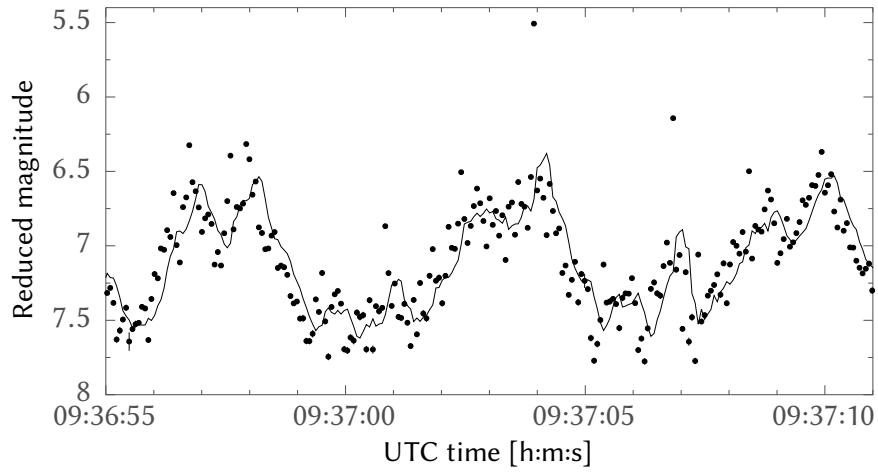


**Figure 6.3:** DMSP-5D2 F12. A complex double peaked structure is visible when rescaling the time axis.

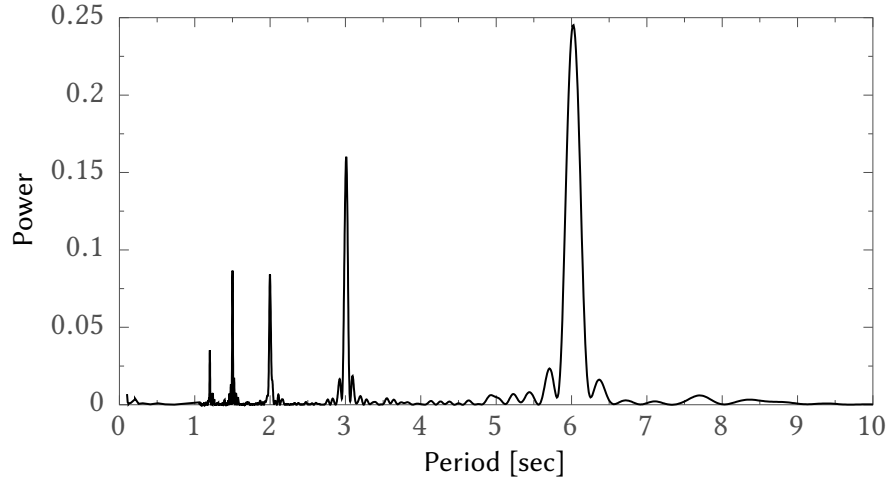
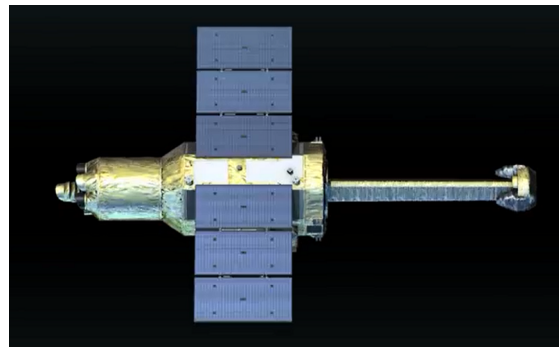


**Figure 6.4:** DMSP-5D2 F12. The Lomb-Scargle (LS) periodogram identifies a peak flash period of 6.02 s, matching the large amplitude variations apparent in Figure 6.2. The fine structure 1.5 s variation shown above is also identified.

## ASTRO-H (Hitomi)

Hitomi is an X-ray astronomy satellite commissioned by the Japan Aerospace Exploration Agency (JAXA). Solar panels were deployed, but during engineering checkout contact was lost. JSpOC reports 10 debris pieces related to what appears to be a breakup of the satellite. The main body and several fragments have been observed tumbling. High frame rate photometry resolves sub-second glints that might reveal nutation over time.



FROM www.pddnet.com

Name	Launch	EOL	Orbit [km]	Length [m]	Mag
Hitomi main	Feb 2016	Mar 2016	570	14	5
Hitomi debris L				?	6

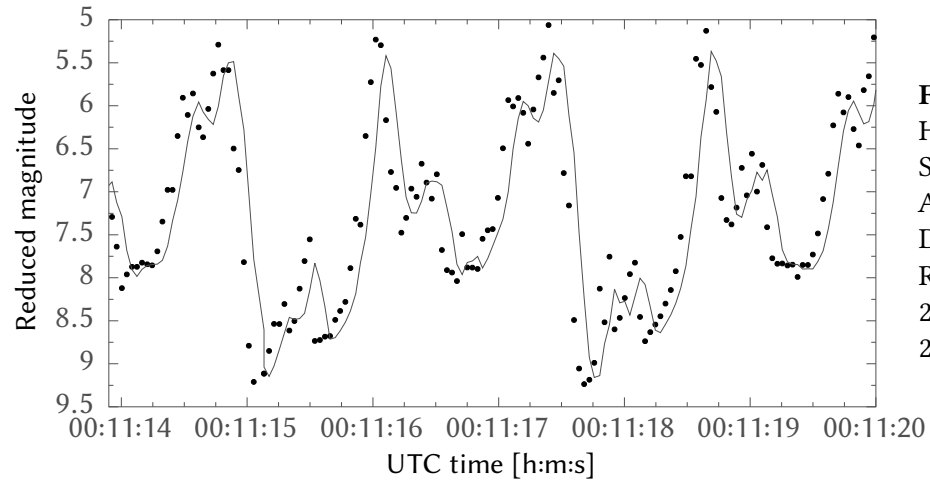


**Figure 6.5:**  
Hitomi main  
SATID 41337  
April 3, 2016  
Daytona Beach, FL  
RASA/G-235  
20 ms  
25 fps

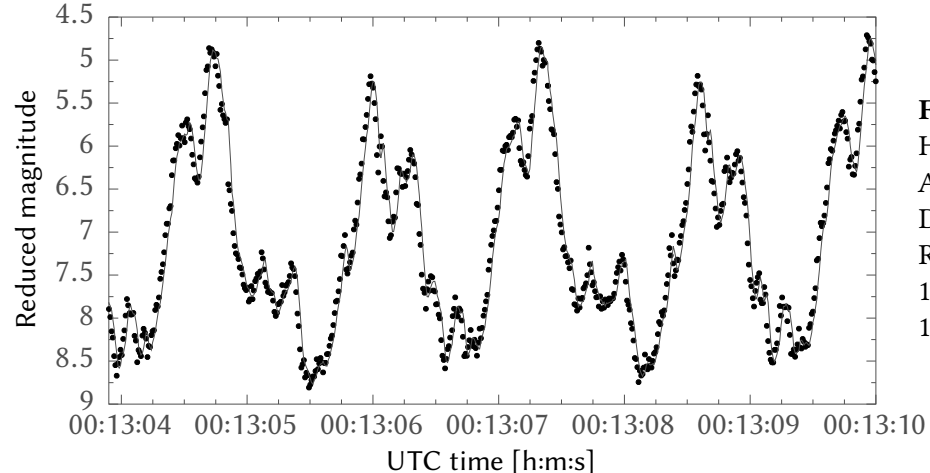


**Figure 6.6:**  
Hitomi main  
April 4, 2016  
Daytona Beach, FL  
RASA/G-235  
10 ms  
100 fps

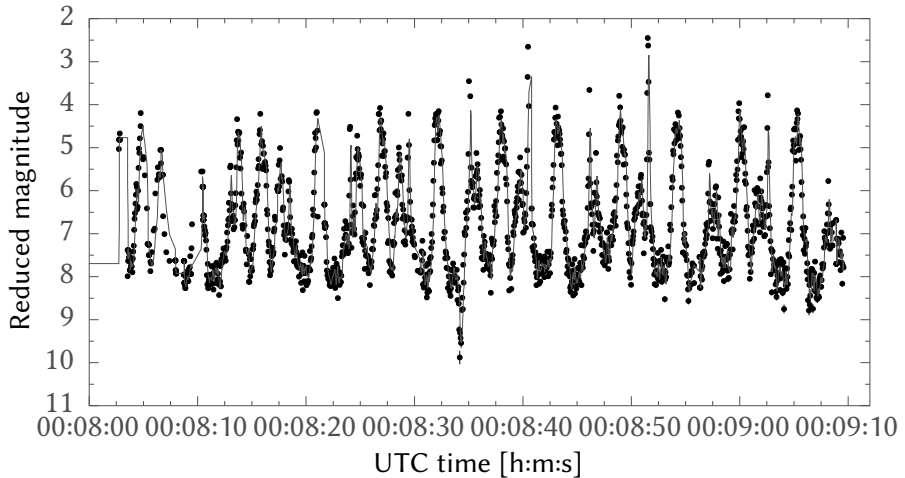


**Figure 6.7:**  
Hitomi debris L  
SATID 41442  
March 31, 2016  
Daytona Beach, FL  
RASA/G-235  
30 ms

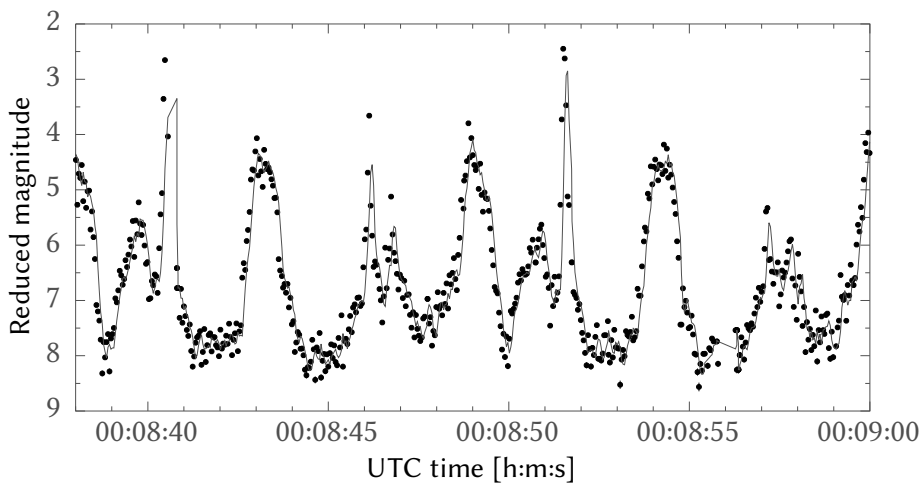


**Figure 6.8:** A crop of the above light curve reveals a flash pattern with a complete period of about 11 s. The pattern includes a very sudden and bright glint which saturates the detector.

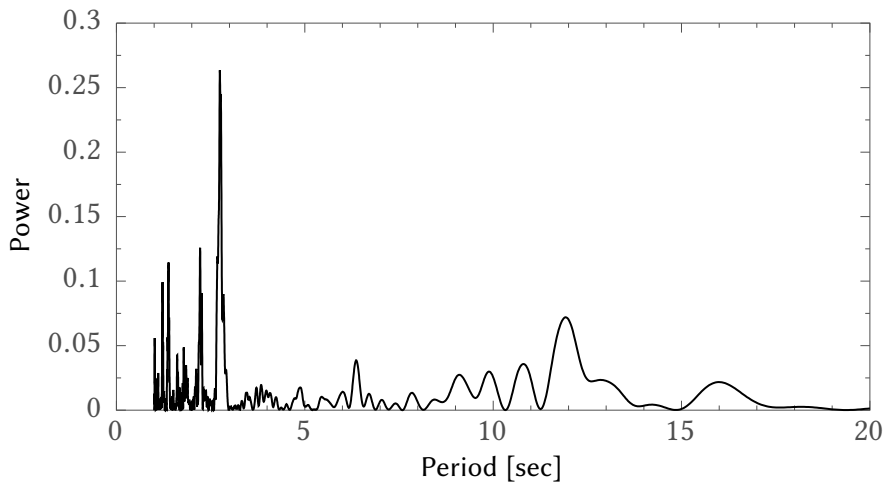


**Figure 6.9:** The peak period is 2.7 s. A 1.4 s period is also identified. The flash period may have changed slightly over the pass, which is why the period seen above does not match exactly with the result of the periodogram.

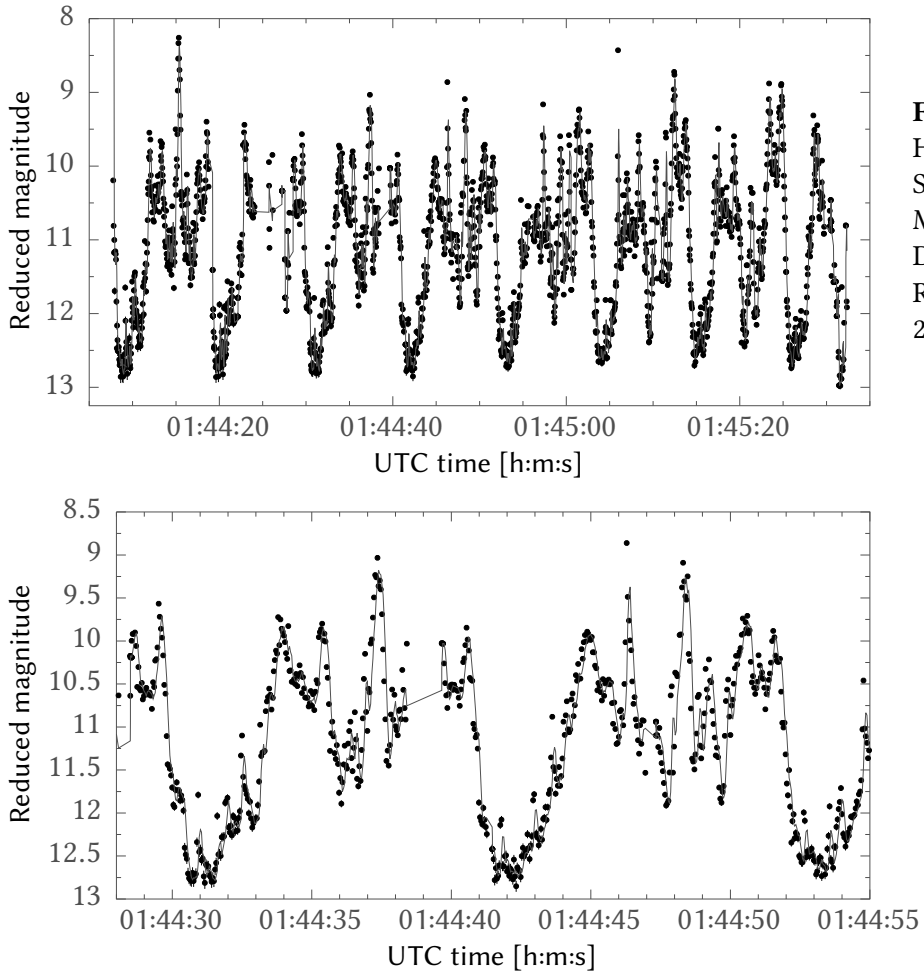


**Figure 6.10:**  
Hitomi debris L  
SATID 41442  
March 31, 2016  
Daytona Beach, FL  
RASA/G-235  
20 ms

**Figure 6.11:** Different lighting conditions during the next pass of Hitomi debris L about 90 minutes later create a dramatically changed light curve than Figure 6.8.

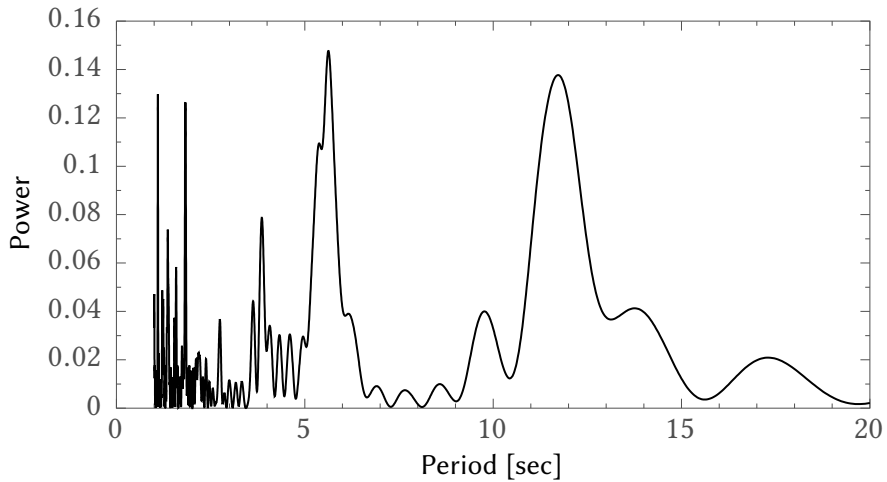


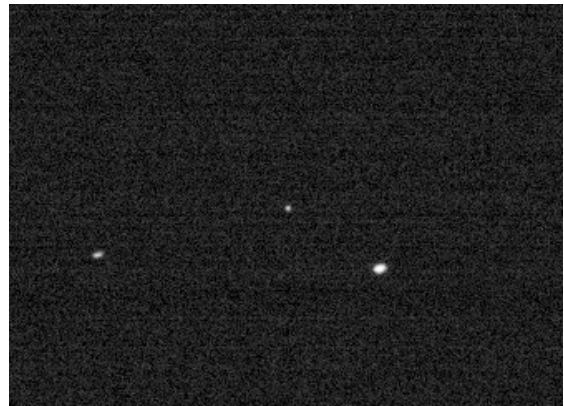
**Figure 6.12:** Although the light curve appears different, it has similar periodicity, including a strong 1.8 s and 11.7 s period identified by the LS periodogram.

## **6.2 Small Satellites**

Small satellites have a wet mass between 100 and 500 kg and are launched either as a secondary payload or on a small launch vehicle.

## KMS 3-2 (North Korean)

KMS 3-2 is the first satellite successfully launched and orbited by North Korea. Although it is purportedly an Earth observation satellite, its size and shape is not known. The satellite appears to be slowly tumbling in orbit with a major flash period of 12.4 s.



KMS 3-2 (centered) through the RASA/G-235.

Name	Launch	EOL	Orbit [km]	Size [m]	Mag
KMS 3-2	Dec 2012	Dec 2012	493 × 585	?	7

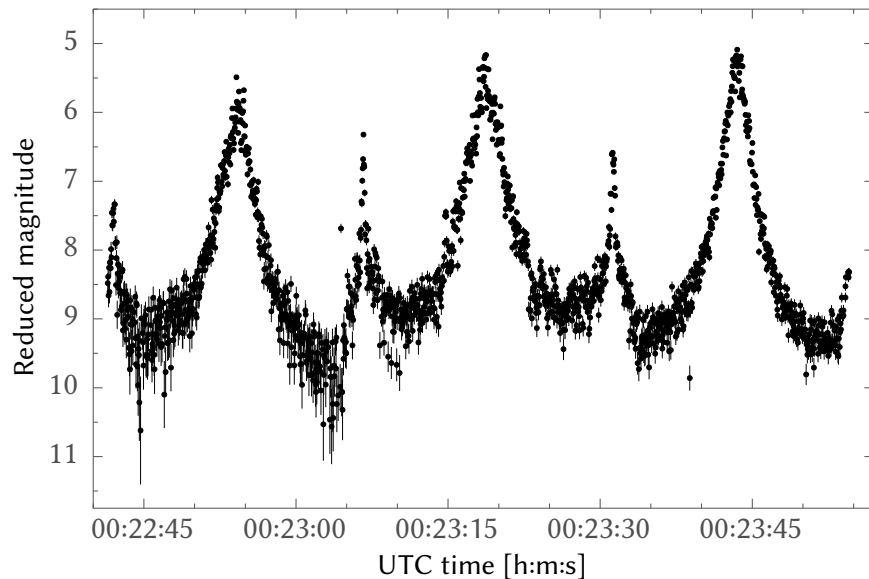


**Figure 6.13:**  
KMS 3-2  
February 2, 2016  
Daytona Beach, FL  
RASA/G-235  
15 ms  
0.61 e<sup>-</sup>/ADU

### **6.3 Microsatellites**

Microsatellites have a wet mass between 10 and 100 kg.

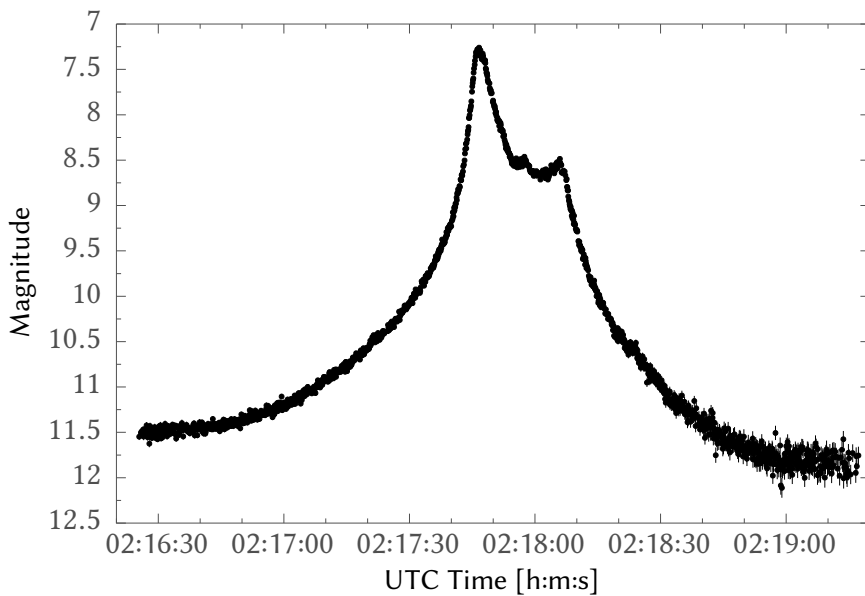
## OPAL

The Orbiting Picosat Automatic Launcher (OPAL) was the second Satellite QUick Research Testbed (SQUIRT) satellite developed by the Space Systems Development Laboratory (SSDL) at Stanford University. This program would eventually create the CubeSat concept used today. OPAL successfully deployed six picosatellites and remained fully operational for 29 months. Although OPAL does not have an attitude control system, the light curve does not show rapid tumbling.



FROM directory.eoportal.org

Name	Launch	EOL	Orbit [km]	Length [m]	Mag
OPAL	Jan 2000	Jun 2002	750	0.42	8



## DANDE

The Drag and Atmospheric Neutral Density Explorer (DANDE) is a sphere covered with small flat solar cells. DANDE's primary mission is to provide a better understanding of the satellite drag environment in the lower-thermosphere. DANDE is spin stabilized around the orbit normal vector, perpendicular to the equator of the sphere, at a nominal rate of 10 rpm. Two observations produced very different light curves that are filled with features likely created by the flat solar cells.



FROM directory.eoportal.org

Name	Launch	EOL	Orbit [km]	Diameter [m]	Mag
DANDE	Sep 2013		320 × 1375	0.46	9

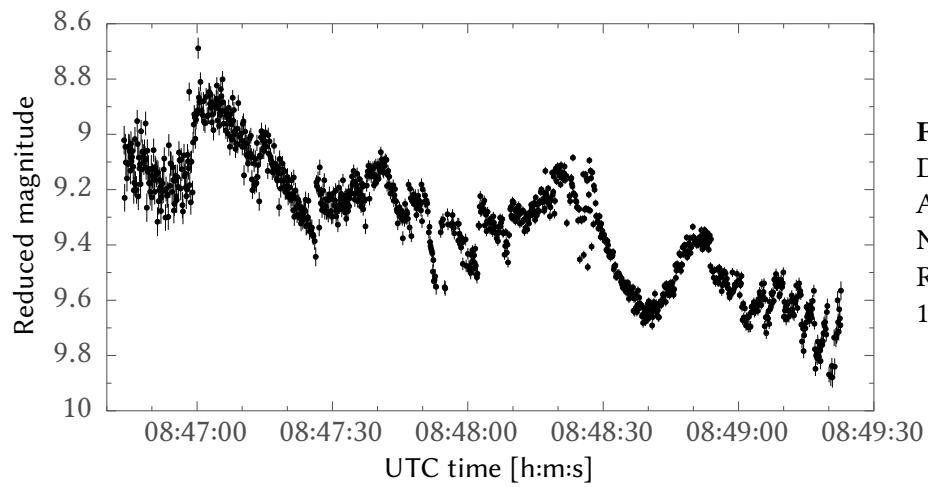


**Figure 6.15:**  
DANDE  
August 2, 2015  
Needham, MA  
RASA/G-235  
125 ms

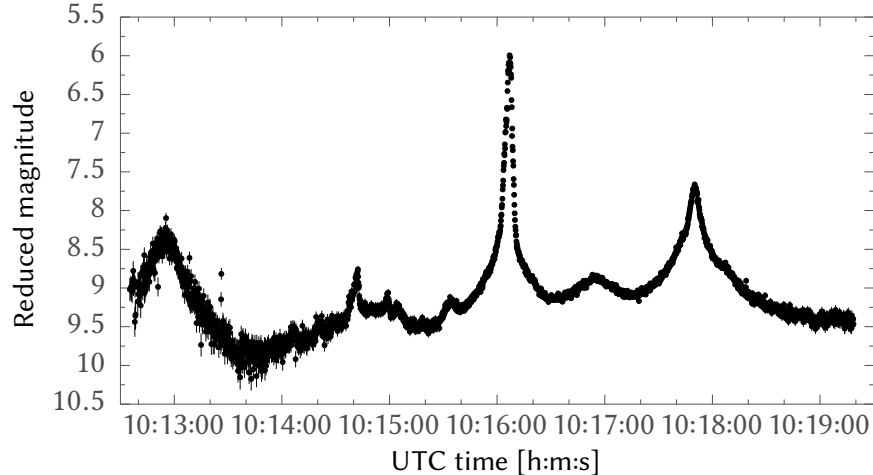
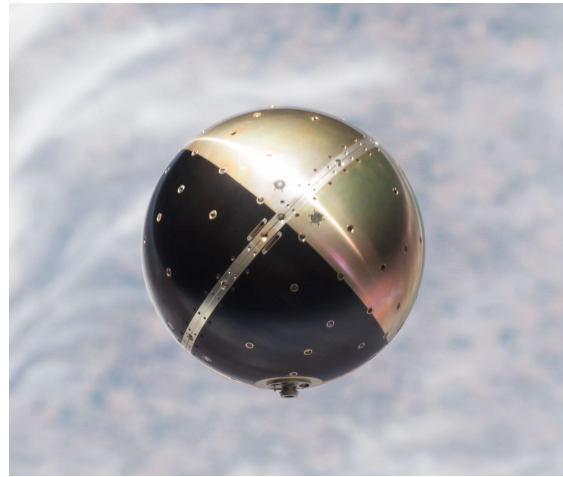


**Figure 6.16:**  
DANDE  
January 18, 2016  
Daytona Beach, FL  
RASA/G-235  
150 ms  
0.18 e<sup>-</sup>/ADU

## SpinSat

The Special Purpose Inexpensive Satellite (SpinSat) is a gold and black anodized sphere. SpinSat's mission goals include performance characterization of experimental thrusters and calibrated atmospheric drag measurement. SpinSat is covered with small retroreflectors so it can be tracked by laser ranging stations. Despite the large color contrast, specular reflection off the anodized aluminum dominates the photometry. Occasional glints can be seen from retroreflectors or antennae.



FROM www.nasa.gov

Name	Launch	EOL	Orbit [km]	Diameter [m]	Mag
SpinSat	Sep 2014	—	345	0.56	9

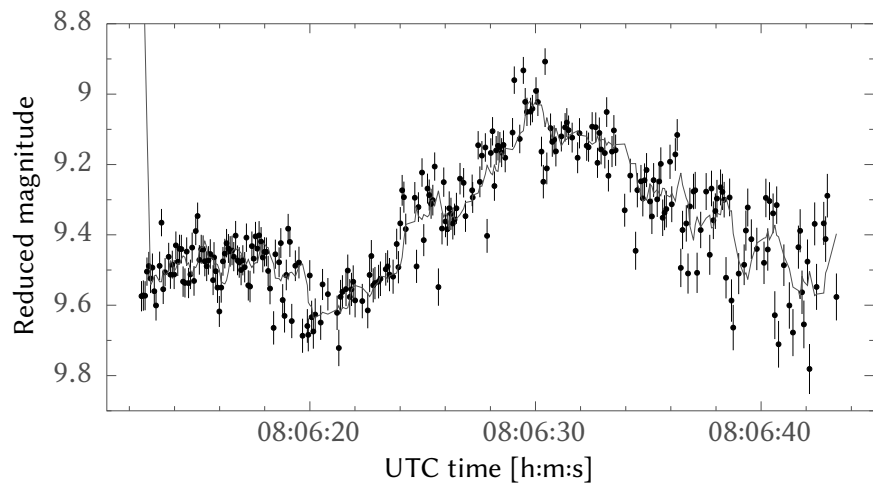


**Figure 6.17:**  
SpinSat  
July 30, 2015  
Needham, MA  
RASA/G-235  
80 ms

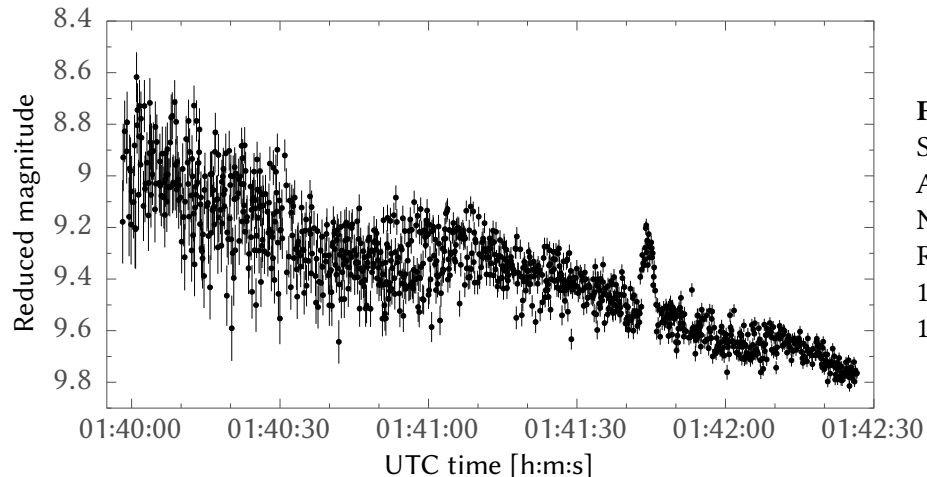


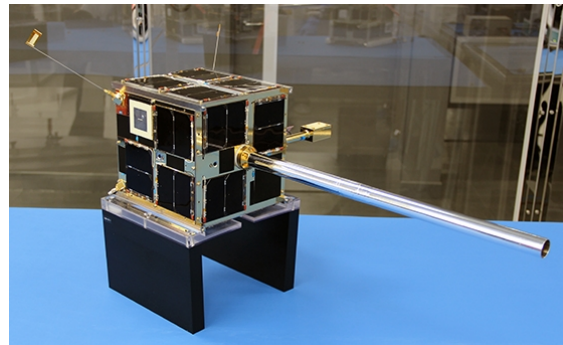
**Figure 6.18:**  
SpinSat  
August 15, 2015  
Needham, MA  
RASA/G-235  
100 ms  
1.26 e<sup>-</sup>/ADU

## **6.4 Nanosatellites and CubeSats**

Nanosatellites have a wet mass between 1 and 10 kg and are almost exclusively launched as secondary payloads.

## AISSat-2

The Automatic Identification System Satellite (AISSat) monitors ships fitted with AIS transponders for increased navigational safety even when ships are far from shore stations. AISSat is fitted with a pre-deployed VHF monopole antenna, possibly the source of the bright glint observed on August 1. AISSat also has a 3-axis attitude determination and control system that allows arbitrary inertial or orbit-frame alignment.



FROM utias-sfl.net

Name	Launch	EOL	Orbit [km]	Length [m]	Mag
AISSat-2	Jul 2014	—	622	0.2	9

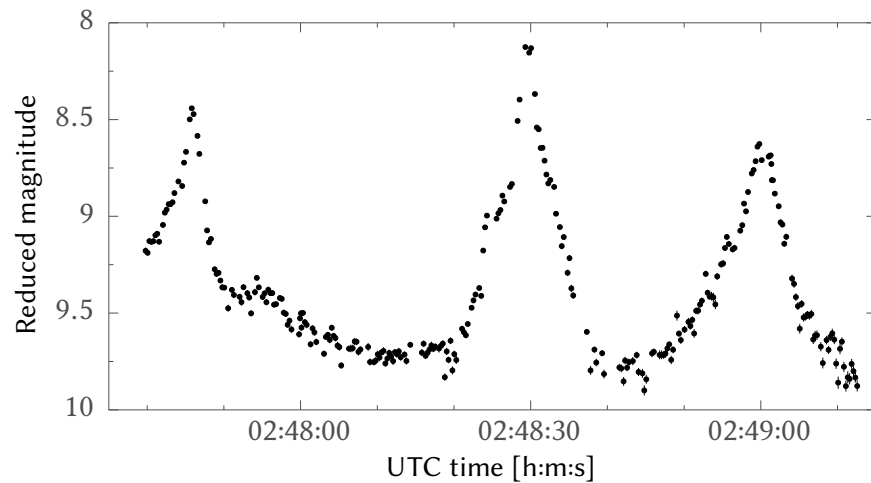


**Figure 6.19:**  
AISSat-2  
July 11, 2015  
Wellesley, MA  
RASA/G-235  
250 ms

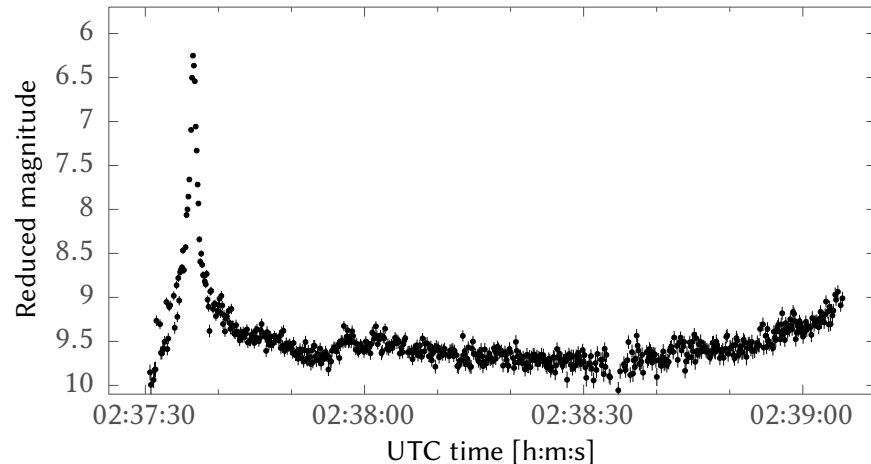
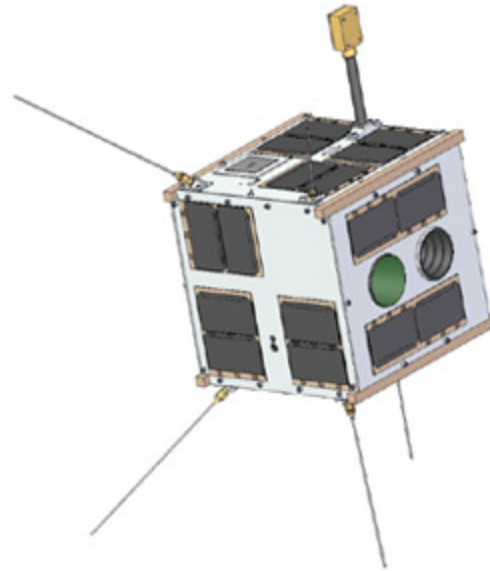


**Figure 6.20:**  
AISSat-2  
August 1, 2015  
Needham, MA  
RASA/G-235  
125 ms

## CanX-3a

CanX-3a, also known as the BRIGht Target Explorer (UniBRITE), is a Canadian nanosatellite design to make photometric observations of bright stars. CanX is a program at the University of Toronto Space Flight Laboratory with goals similar to the CubeSat design, but using slightly larger 20 cm cube satellites. CanX-3a has 4 wire UHF antennas and a small magnetometer and is 3-axis stabilized.



FROM space.skyrocket.de

Name	Launch	EOL	Orbit [km]	Length [m]	Mag
CanX-3a	Feb 2013	—	775	0.2	10

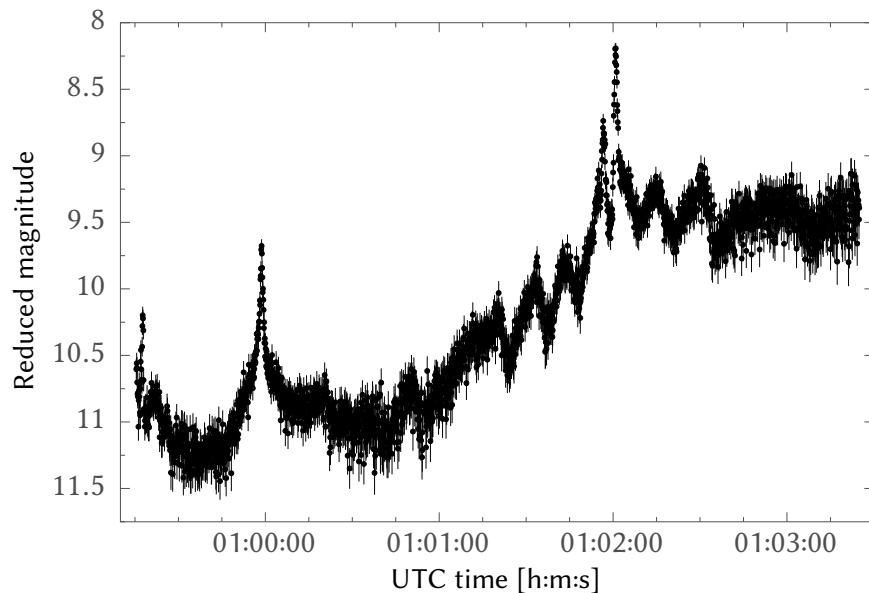


**Figure 6.21:**  
CanX-3a  
January 18, 2016  
Daytona Beach, FL  
RASA/G-235  
100 ms  
 $1.26 \text{ e}^-/\text{ADU}$

## DICE

The Dynamic Ionosphere CubeSat Experiment (DICE) is a pair of 1.5U CubeSats with the mission to map the geomagnetic storm enhanced density plasma bulge and plume formations in Earth's ionosphere. DICE has several expandable booms and antennae and is supposed to be spin stabilized at about 12 RPM. Observations of both satellites have been made which show a rapid flash period of just over 1 s due to the large number of deployable instruments and antennae. The flash pattern appears to show 4 stepped intensities before repeating.



FROM directory.eoportal.org

Name	Launch	EOL	Orbit [km]	Length [m]	Mag
DICE-1	Oct 2011		436 × 705	0.15	11
DICE-2			438 × 686		

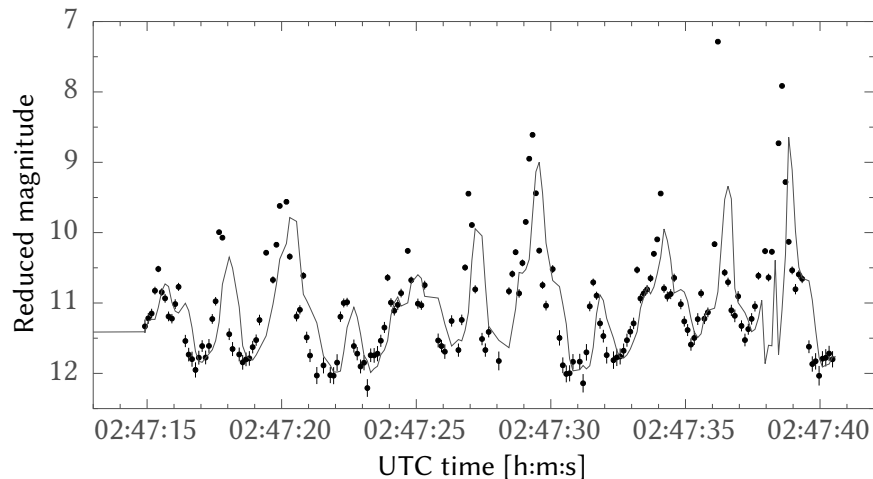


**Figure 6.22:**  
DICE-1  
August 1, 2015  
Needham, MA  
RASA/G-235  
125 ms

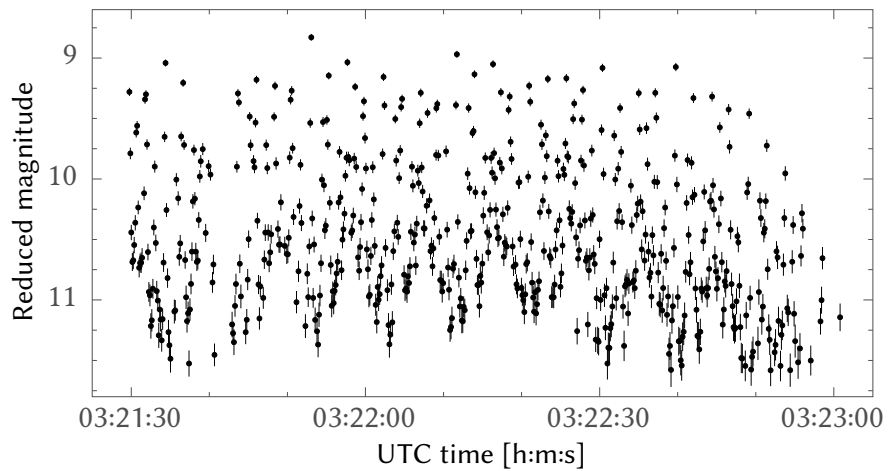


**Figure 6.23:**  
DICE-2  
August 1, 2015  
Needham, MA  
RASA/G-235  
125 ms

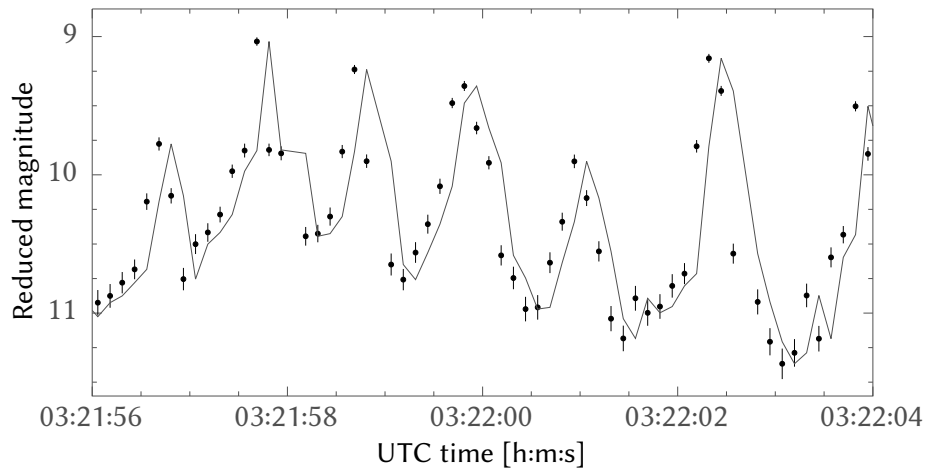


**Figure 6.24:** Higher frequency flash periods are visible when rescaling data from Figure 6.23.

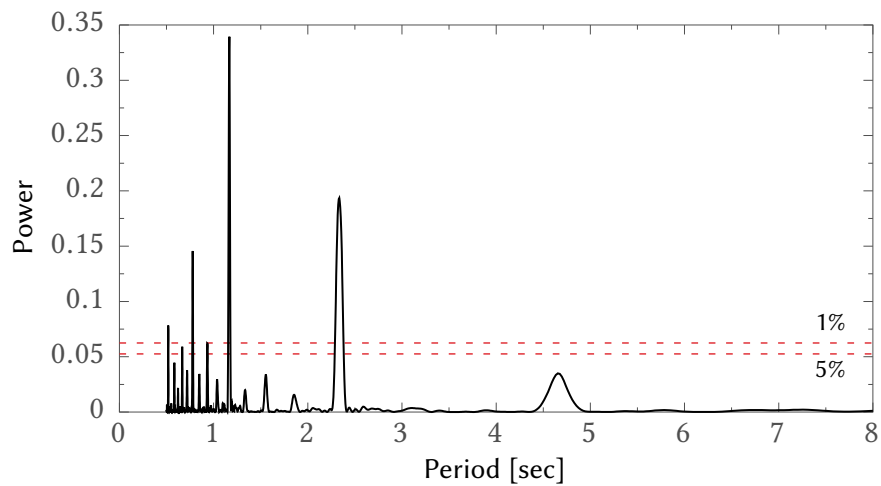
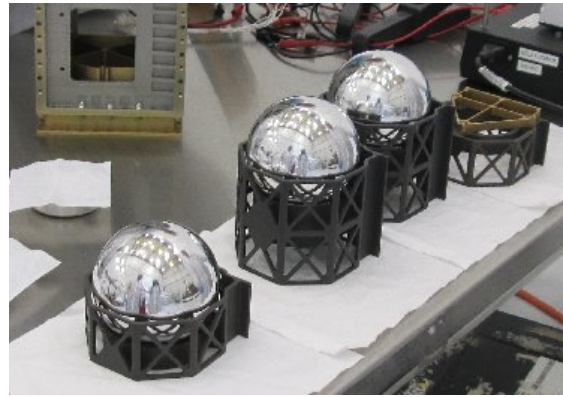


**Figure 6.25:** A Lomb-Scargle periodogram identifies the primary flash period as 1.17 s.

## POPACS

The Polar Orbiting Passive Atmospheric Calibration Sphere (POPACS) is a set of three 10 cm aluminum spheres used for measuring changes in density of the upper atmosphere. Each of the spheres are filled with sand and bismuth shot so that they have different ballistic coefficients. Although they began as highly specular spheres, oxidation may be responsible for variation seen in recent observations of each of the spheres.



FROM sites.google.com/site/usupopacs/

Name	Launch	EOL	Orbit [km]	Diameter [m]	Mag
POPACS-1	Sep 2013	—	322 × 1291	0.1	12
POPACS-2			320 × 1355		
POPACS-3			324 × 1389		

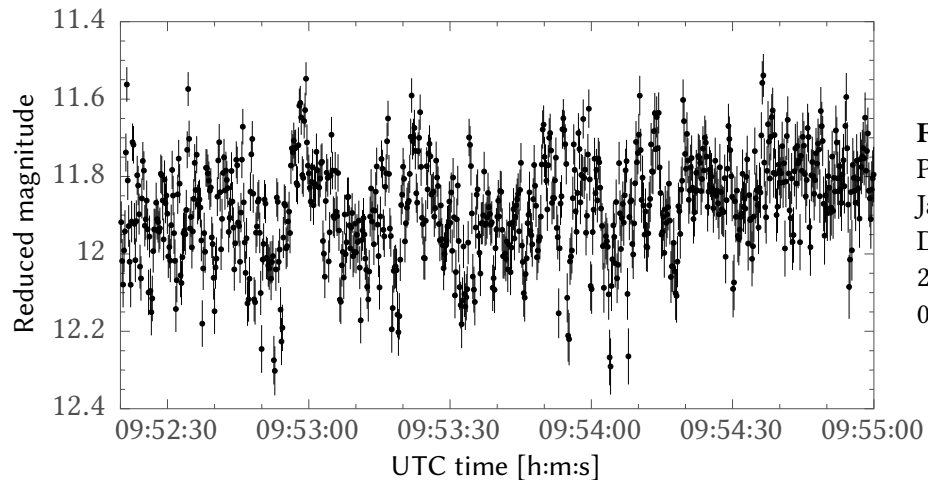


**Figure 6.26:**  
POPACS-1  
January 18, 2016  
Daytona Beach, FL  
200 ms  
0.18 e<sup>-</sup>/ADU

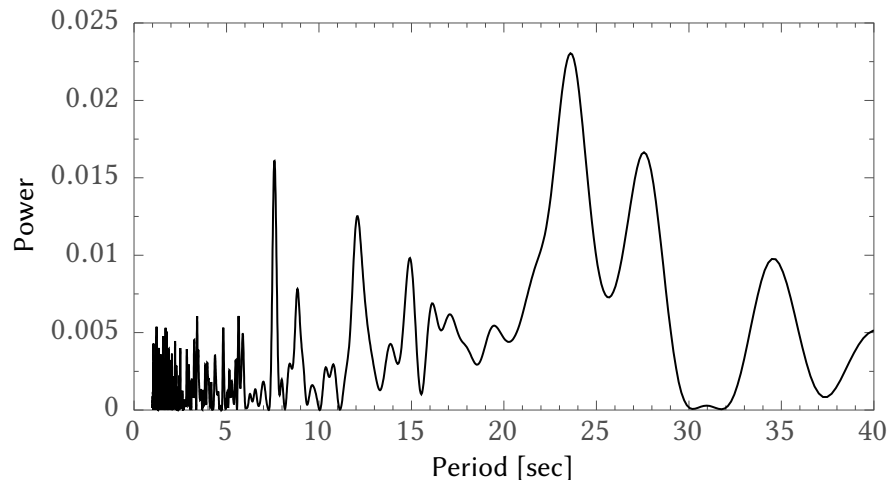


**Figure 6.27:** The major flash periods from the Lomb-Scargle periodogram are 23.6 s and 7.6 s

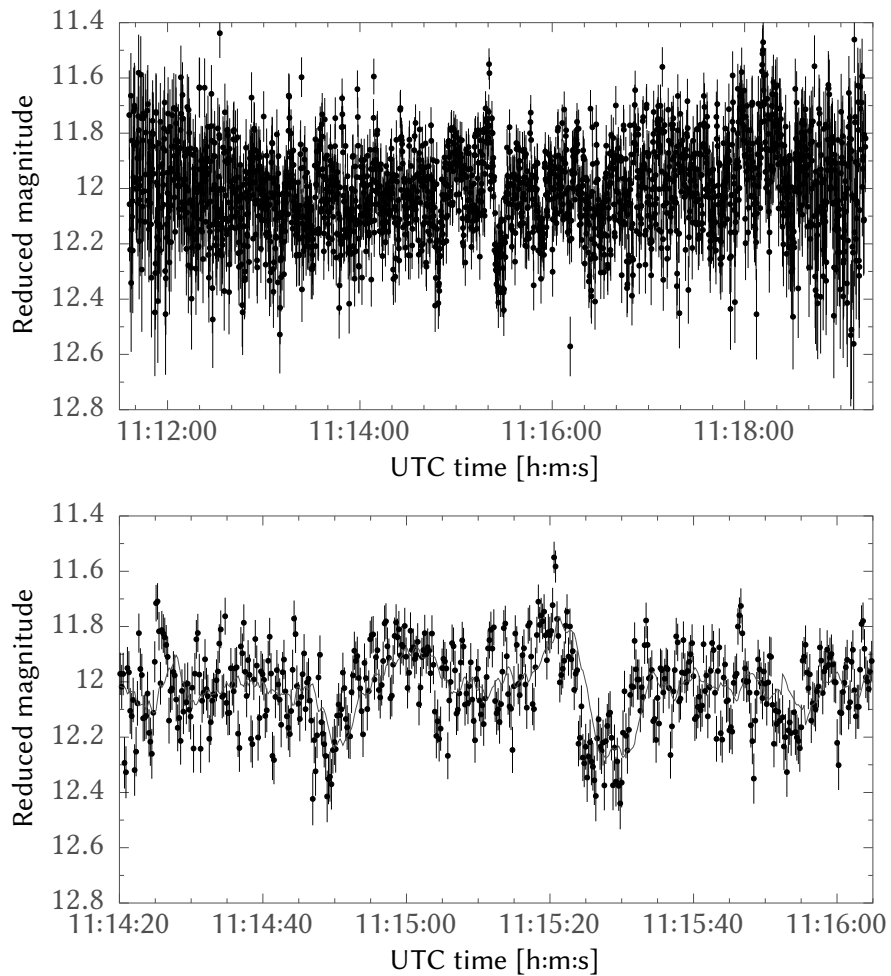


**Figure 6.28:**  
POPACS-2  
January 18, 2016  
Daytona Beach, FL  
200 ms  
 $0.18 \text{ e}^-/\text{ADU}$

**Figure 6.29:** A zoomed section of the center of Figure 6.28 shows significant photometric variation over about 10 s.

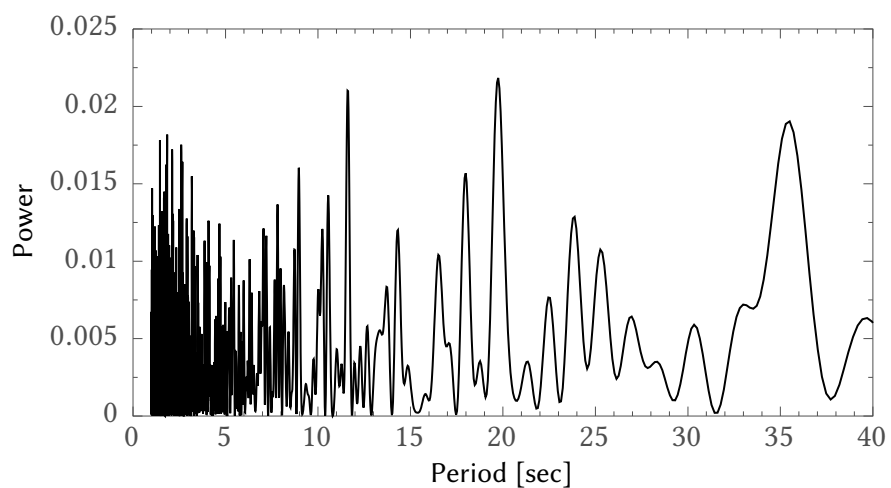


**Figure 6.30:** A Lomb-Scargle periodogram shows major flash periods of 19.7 s and 11.6 s.

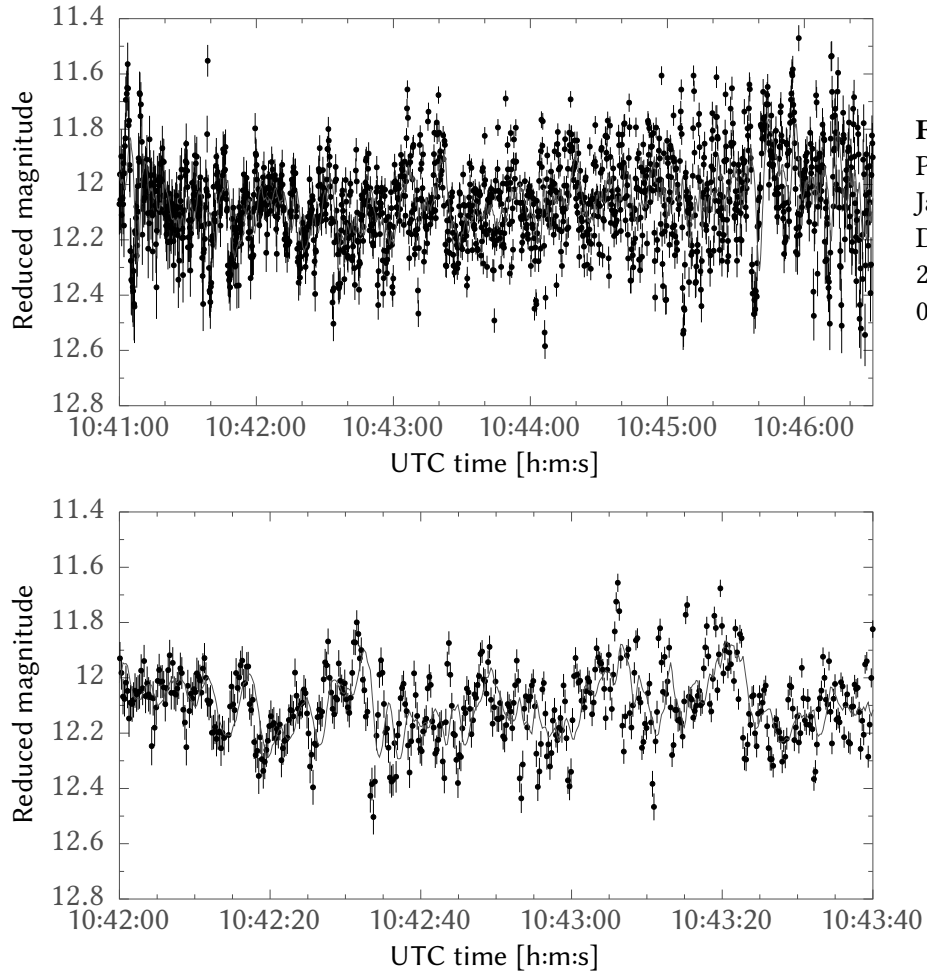


**Figure 6.31:**  
POPACS-3  
January 18, 2016  
Daytona Beach, FL  
200 ms  
 $0.18 \text{ e}^-/\text{ADU}$

**Figure 6.32:** A cropped portion of the plot above showing photometric variation after 10:42:00 UTC.

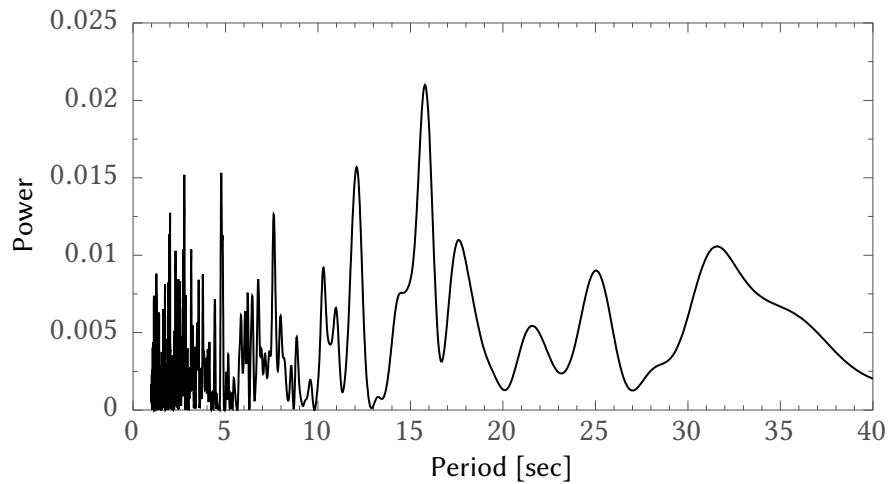


**Figure 6.33:** Major flash periods are 15.8 s, 12.1 s and 4.8 s.

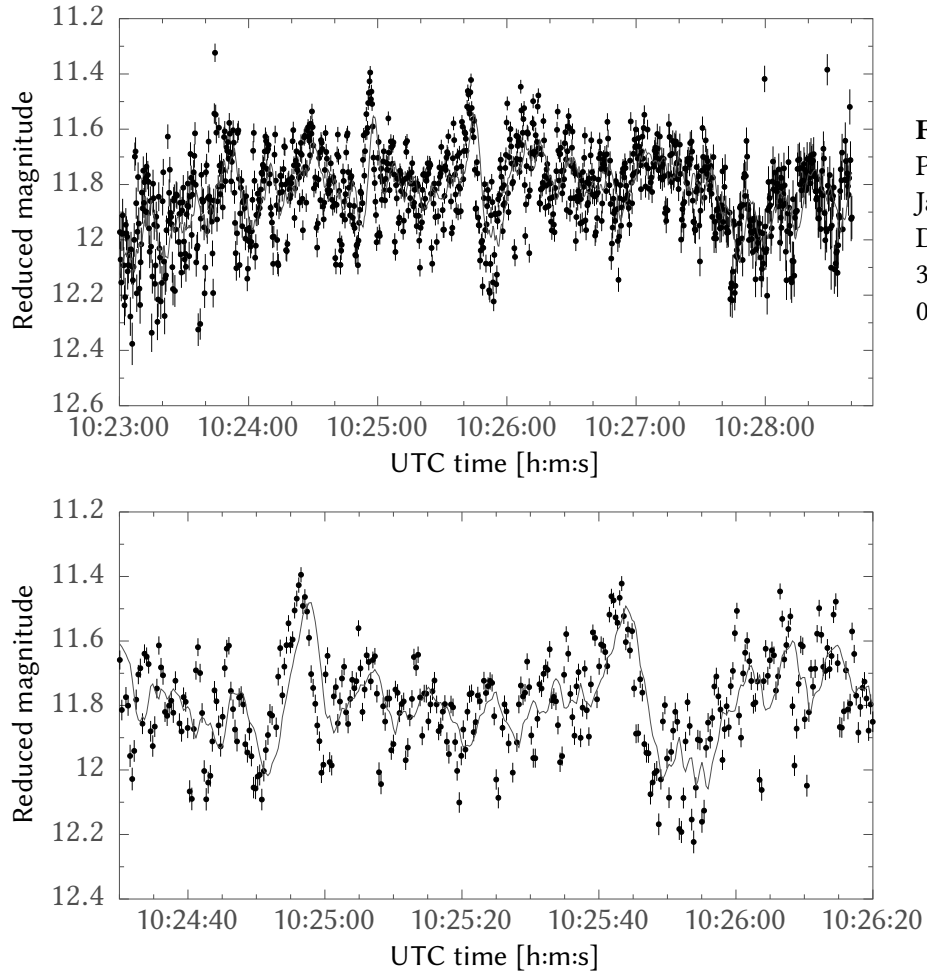


**Figure 6.34:**  
POPACS-3  
January 20, 2016  
Daytona Beach, FL  
300 ms  
 $0.055 \text{ e}^-/\text{ADU}$ .

**Figure 6.35:** Significant variations are apparent in this zoomed portion of Figure 6.34.

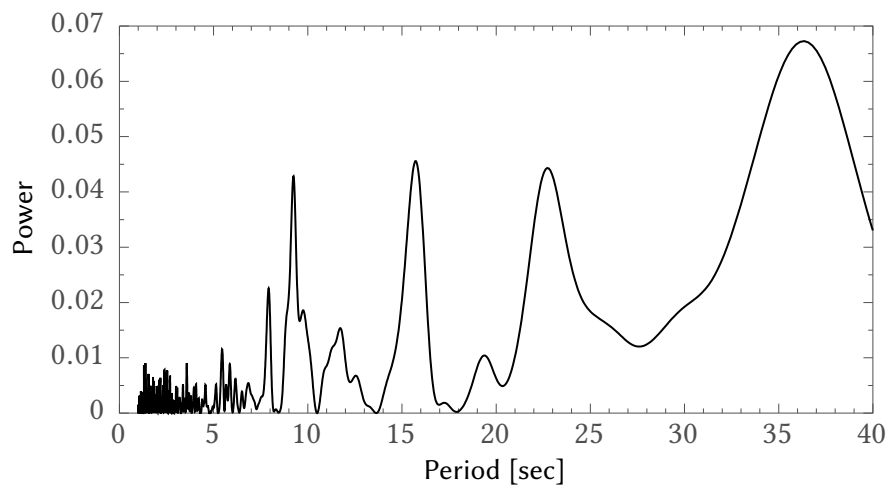


**Figure 6.36:** Major flash periods include 15.7 s and 9.2 s. The 15 s period was also observed in the same satellite two days earlier (Figure 6.33). Much longer periods in the periodogram are less likely to be true RSO behavior because fewer long period samples are captured.

# Chapter 7

## Future Efforts and Conclusions

The OSCOM system has demonstrated the ability to regularly track and optically observe small satellites and CubeSats using commercially available and amateur-class equipment. This thesis has reviewed many of the elements required for satellite observations, both hardware and software, and addresses the specific approaches taken by OSCOM. These observations and their derived data products can be used to characterize physical traits of resident space objects.

OSCOM has proven its feasibility, but can implement several changes to improve its efficiency and accuracy. One of the primary limitations in the time between observation and completed photometry is organizing and reducing image data. In just an hour, several satellites can be observed with the detector at different exposure times and gain levels that all need their own calibration frames. Although OSCOM is flexible in how these images are saved and stored, a standardized image capture routine would greatly reduce image reduction time and require less human interaction.

Several minor steps of the photometry and analysis process could also be automated, but are currently performed by an analyst. Statistical routines can automatically make decisions on aperture radii and data filtering. Most importantly, however, OSCOM should implement a relative photometry technique using the background field stars

visible in every frame. This helps reduce frame-to-frame system variability and results in magnitudes calibrated with the stellar magnitude system.

As more and more optical space object data is collected, it can be organized and mined using machine learning techniques. Change detection algorithms are the simplest to implement, but can alert satellite operators to unexpected or unintended changes to a satellite. Database mining also enables unknown space object identification or classification based on the characteristics of current objects. These tools provide new capabilities for satellite operators and space situational awareness analysts alike.

# Bibliography

- Ackermann, M., Zimmer, P., McGraw, J., & Kopit, E. (2015). COTS Options for Low-Cost SSA. In *Proceedings of the Advanced Maui Optical and Space Surveillance Technologies Conference*. Maui, Hawaii.
- Africano, J., Kervin, P., Hall, D., Sydney, P., Ross, J., Payne, T., ... Barker, E. (2005, April 18). Understanding Photometric Phase Angle Corrections. In D. Danesy (Ed.), *Proceedings of the 4th European Conference on Space Debris* (p. 141). Darmstadt, Germany. Retrieved from <http://adsabs.harvard.edu/full/2005ESASP.587..141A>
- Allied Vision. (2015, November 2). *Manta Technical Manual*. Version 7.3.0. Retrieved from [https://www.alliedvision.com/fileadmin/content/documents/products/cameras/Manta/techman/Manta\\_TechMan.pdf](https://www.alliedvision.com/fileadmin/content/documents/products/cameras/Manta/techman/Manta_TechMan.pdf)
- Astropy Collaboration, Robitaille, T. P., Tollerud, E. J., Greenfield, P., Droettboom, M., Bray, E., ... Streicher, O. (2013, October). Astropy: A community Python package for astronomy. *Astronomy & Astrophysics*, 558, A33. doi:10.1051/0004-6361/201322068. arXiv: 1307.6212 [astro-ph.IM]
- Azari, D. M. & Ehrhorn, B. (2007, September 12). Autonomous Low Earth Orbit Satellite and Orbital Debris Tracking using Mid Aperture COTS Optical Trackers. In S. Ryan (Ed.), *Proceedings of the Advanced Maui Optical and Space Surveillance Technologies Conference* (E10). Maui, Hawaii.
- Baker, M. (2011, November). Faster frames, clearer pictures. *Nature Methods*, 8(12), 1005–1009. doi:10.1038/nmeth.1777
- Belskaya, I. & Shevchenko, V. (2014). *Asteroid photometry: Phase-angle effects*. Asteroids, Comets, and Meteors, Helsinki, Finland. Retrieved from <http://www.helsinki.fi/acm2014/pdf-material/Day-2/Session-3/Room-4/BELSKAYA-6060.pdf>
- Bessell, M. S. (1990, October). UBVRI passbands. *PASP*, 102, 1181. doi:10.1086/132749
- Boller & Chivens. (2011). Baker Nunn Satellite Tracking Cameras. Retrieved from <http://bollerandchivens.com/?p=561>
- Buton, C., Copin, Y., Aldering, G., Antilogus, P., Aragon, C., Bailey, S., ... Wu, C. (2012, December). Atmospheric extinction properties above Mauna Kea from the Nearby

- SuperNova Factory spectro-photometric data set. *Astronomy & Astrophysics*, 549, A8. doi:10.1051/0004-6361/201219834
- Calef, B., Africano, J., Birge, B., Hall, D., & Kervin, P. (2006, August). Photometric signature inversion. In V. L. Gamiz, P. S. Idell, & M. S. Strojnik (Eds.), *Unconventional Imaging II*. SPIE-Intl Soc Optical Eng. doi:10.1117/12.683015
- Chaudhary, A. B., Payne, T. E., Lucas, K., Mutschler, S., Vincent, T., Dao, P., & Murray-Krezan, J. (2013, September 10). Point Pairing Method Based on the Principle of Material Frame Indifference for the Characterization of Unknown Space Objects using Non-Resolved Photometry Data. In R. S. (Ed.), *Proceedings of the Advanced Maui Optical and Space Surveillance Technologies Conference* (E53). Maui, Hawaii.
- Coder, R. D. & Holzinger, M. J. (2013, September 10). Sizing of a Raven-class telescope using performance sensitivities. In *Proceedings of the Advanced Maui Optical and Space Surveillance Technologies Conference*. Maui, Hawaii.
- Cook, R. L. & Torrance, K. E. (1982, January). A Reflectance Model for Computer Graphics. *TOG*, 1(1), 7–24. doi:10.1145/357290.357293
- Cowardin, H., Seitzer, P., Abercromby, K., Barker, E., Buckalew, B., Cardona, T., ... Lederer, S. (2013, September 10). Observations of Titan IIIC Transtage fragmentation debris. In *Proceedings of the Advanced Maui Optical and Space Surveillance Technologies Conference*. Maui, Hawaii.
- CubeSat. (2016). Retrieved from <http://wwqw.cubesat.org/index.php/about-us>
- Dearborn, M. E., Chun, F. K., Liu, J., & Tippets, R. D. (2011, September 13). USAF Academy Center for Space Situational Awareness. In S. Ryan (Ed.), *Proceedings of the Advanced Maui Optical and Space Surveillance Technologies Conference* (E17). Maui, Hawaii.
- Frith, J., Gibson, B., Knox, R., & Kuluhiva, K. (2008, September 17). Simultaneous Single Site Color Photometry of LEO Satellites. In S. Ryan (Ed.), *Proceedings of the Advanced Maui Optical and Space Surveillance Technologies Conference* (E59). Maui, Hawaii. Retrieved from [www.amostech.com/TechnicalPapers/2008/Posters/Frith.pdf](http://www.amostech.com/TechnicalPapers/2008/Posters/Frith.pdf)
- Fukugita, M., Ichikawa, T., Gunn, J. E., Doi, M., Shimasaku, K., & Schneider, D. P. (1996, April). The Sloan Digital Sky Survey Photometric System. *The Astronomical Journal*, 111, 1748. doi:10.1086/117915
- Gibson, D. M., Pearce, E. C., Blythe, M. S., & Trujillo, P. J. (1993, September). Orbital debris characterization: ETS staring survey. In F. A. Allahdadi (Ed.), *Space Debris Detection and Mitigation*. SPIE-Intl Soc Optical Eng. doi:10.1117/12.156542

- Graff, M. E. (2010). *Development of a Remotely Operated Autonomous Satellite Tracking System* (Master's thesis, Air Force Institute of Technology). Retrieved from <http://www.dtic.mil/cgi-bin/GetTRDoc?Location=U2&doc=GetTRDoc.pdf&AD=ADA517531>
- Graversen, T., Frederiksen, M. K., & Vedstesen, S. V. (2002, June 6). *Attitude Control System for AAU CubeSat* (Master's thesis, Aalborg University).
- Gray, D. F. (1992, November). The inferred color index of the sun. *PASP*, 104, 1035. doi:10.1086/133086
- Hall, D. (2008). Optical CubeSat Discrimination. In *Proceedings of the Advanced Maui Optical and Space Surveillance Technologies Conference*. Maui, Hawaii. Retrieved from <http://www.amostech.com/TechnicalPapers/2008/NROC/Hall.pdf>
- Hall, D., Africano, J., Archambeault, D., Birge, B., Witte, D., & Kervin, P. (2006, September 10). AMOS Observations of NASA's IMAGE Satellite. In S. Ryan (Ed.), *Proceedings of the Advanced Maui Optical and Space Surveillance Technologies Conference* (E76). Maui, Hawaii.
- Hall, D., Calef, B., Knox, K., Bolden, M., & Kervin, P. (2007, September 12). Separating Attitude and Shape Effects for Non-resolved Objects. In R. S. (Ed.), *Proceedings of the Advanced Maui Optical and Space Surveillance Technologies Conference* (E51). Maui, Hawaii.
- Hall, D. & Kervin, P. [Paul]. (2013, September 10). Analysis of Faint Glints from Stabilized GEO Satellites. In S. Ryan (Ed.), *Proceedings of the Advanced Maui Optical and Space Surveillance Technologies Conference* (E34). Maui, Hawaii.
- Hampf, D., Wagner, P., & Riede, W. (2015). *Optical technologies for the observation of low Earth orbit objects*. arXiv: 1501.05736. Retrieved from <http://arxiv.org/abs/1501.05736>
- Hejduk, M. (2011, September 13). Specular and Diffuse Components in Spherical Satellite Photometric Modeling. In S. Ryan (Ed.), *Proceedings of the Advanced Maui Optical and Space Surveillance Technologies Conference* (E15). Maui, Hawaii. Retrieved from <http://www.amostech.com/TechnicalPapers/2011/NROC/HEJDUK.pdf>
- Hejduk, M., Cowardin, M., & Stansbery, E. (2012). Satellite Material Type and Phase Function Determination in Support of Orbital Debris Size Estimation. In *Proceedings of the Advanced Maui Optical and Space Surveillance Technologies Conference*. Maui, Hawaii.
- Henize, K. G., O'Neill, C. A., Mulrooney, M. K., & Anz-Meador, P. (1994, July). Optical properties of orbital debris. *Journal of Spacecraft and Rockets*, 31(4), 671–677. doi:10.2514/3.26494

- Hoffmann, W. F., Krotkov, R., & Dicke, R. H. (1960, January). Precision Optical Tracking of Artificial Satellites. *IRE Trans. Mil. Electron. MIL-4*(1), 28–37. doi:10.1109/iretmil.1960.5008190
- Hoots, F. R. & Roehrich, R. L. (1980). *Spacetrack Report No. 3: Models for Propagation of NORAD Element Sets* (No. 3). United States Air Force Aerospace Defense Command. Retrieved from <http://www.dtic.mil/cgi/tr/fulltext/u2/a093554.pdf>
- Hope, D. A. (2014, September 9). A new approach to computing information in measurements of non-resolved space objects by the Falcon Telescope Network. In S. Ryan (Ed.), *Proceedings of the Advanced Maui Optical and Space Surveillance Technologies Conference* (E74). Maui, Hawaii.
- JSpOC. (2016, February 18). Satellite Catalog Box Score. Retrieved from <https://www.space-track.org/#/boxscore>
- Kervin, P. W., Nishimoto, D. L., Sydney, P. F., Africano, J. L., Hoo, V. S., Talent, D. L., ... Africano, B. M. (1998, July). Raven concept applied to asteroid and satellite surveillance. In S. D'Odorico (Ed.), *Optical Astronomical Instrumentation*. SPIE-Intl Soc Optical Eng. doi:10.1117/12.316839
- Kervin, P. [Paul], Hall, D., Bolden, M., & Toth, J. (2010). Phase Angle: What is it Good For? In *Proceedings of the Advanced Maui Optical and Space Surveillance Technologies Conference*. Maui, Hawaii. Retrieved from <http://www.amostech.com/technicalpapers/2010/nroc/kervin.pdf>
- Kervin, P. [Paul], Hall, D., Toth, J., & Lambert, J. (2014, July 10). Anomaly Resolution Using Optical Signatures. In *Defense Applications of Signal Processing Workshop*. Queensland, Australia.
- Kervin, P. [P.W.], Africano, J., Sydney, P., & Hall, D. (2005, January). Small satellite characterization technologies applied to orbital debris. *Advances in Space Research*, 35(7), 1214–1225. doi:10.1016/j.asr.2004.11.038
- Lambert, J. V. (1971). *Measurement of the Visible Reflectance Spectra of Orbiting Satellites* (Master's thesis, Air Force Institute of Technology School of Engineering). Retrieved from <http://www.dtic.mil/cgi/tr/doc/pdf?AD=AD0726988>
- Lambert, J. V., Osteen, T. J., & Kraszewski, B. (1993, September). Determination of debris albedo from visible and infrared brightnesses. In F. A. Allahdadi (Ed.), *Space Debris Detection and Mitigation*. SPIE-Intl Soc Optical Eng. doi:10.1117/12.156557
- Landolt, A. U. (1992, July). UBVRI photometric standard stars in the magnitude range 11.5-16.0 around the celestial equator. *The Astronomical Journal*, 104, 340. doi:10.1086/116242

- Lederer, S. M., Seitzer, P., Cowardin, H. M., Barker, E. S., Abercromby, K. J., & Burkhardt, A. (2012, September 11). Preliminary Characterization of IDCSP Spacecrafts through a Multi-Analytical Approach. In *Proceedings of the Advanced Maui Optical and Space Surveillance Technologies Conference*. Maui, Hawaii.
- Linares, R., Shoemaker, M., Walker, A., Mehta, P. M., Palmer, D. M., Thompson, D. C., ... Crassidis, J. L. (2013). Photometric Data from Non-Resolved Objects for Space Object Characterization and Improved Atmospheric Modeling. In *Proceedings of the Advanced Maui Optical and Space Surveillance Technologies Conference* (pp. 1–15). Maui, Hawaii.
- Lomb, N. R. (1976, February). Least-squares frequency analysis of unequally spaced data. *Astrophys Space Sci*, 39(2), 447–462. doi:10.1007/bf00648343
- McCue, G., Williams, J., & Morford, J. (1971). Optical characteristics of artificial satellites. *Planetary and Space Science*. Retrieved from <http://www.sciencedirect.com/science/article/pii/0032063371901371>
- McGraw, J. T., Zimmer, P. C., & Ackermann, M. R. (2014, September 15). The fundamental role of wide-field imaging in Space Situational Awareness. In S. Ryan (Ed.), *Proceedings of the Advanced Maui Optical and Space Surveillance Technologies Conference*. Maui, Hawaii.
- McKerns, M. M., Strand, L., Sullivan, T., Fang, A., & Aivazis, M. A. G. (2012). Building a Framework for Predictive Science. *CoRR*, *abs/1202.1056*. Retrieved from <http://arxiv.org/abs/1202.1056>
- NanoRacks. (2013). *NanoRacks CubeSat Deployer (NRCSD) Interface Control Document*. NanoRacks, LLC.
- Nishimoto, D. L., Africano, J. L., Sydney, P. F., Hamada, K. M., Hoo, V. S., Kervin, P. W., & Stansbery, E. G. (2001, December). Spectroscopic observations of space objects and phenomena using Spica and Kala at AMOS. In A. R. Pirich, P. L. Repak, P. S. Idell, & S. R. Czyzak (Eds.), *Multifrequency Electronic/Photonic Devices and Systems for Dual-Use Applications*. SPIE-Intl Soc Optical Eng. doi:10.1117/12.455428
- NSSDCA. (2016). Sputnik 1. Retrieved from <http://nssdc.gsfc.nasa.gov/nmc/spacecraftDisplay.do?id=1957-001B>
- O'Keefe, J. (1955). The geodetic significance of an artificial satellite. *Jet propulsion*, 25, 75–76.
- Oltrogge, D. L. & Ramrath, J. (2014, September 9). Parametric Characterization of SGP4 Theory and TLE Positional Accuracy. In S. Ryan (Ed.), *Proceedings of the Advanced Maui Optical and Space Surveillance Technologies Conference* (E87). Maui, Hawaii.

- Payne, T. E. [Tamara E], Gregory, S. a., Tombasco, J., Luu, K., Durr, L., Desm, A., & Des, A. (2007). Satellite Monitoring, Change Detection, and Characterization Using Non- Resolved Electro-Optical Data From a Small Aperture Telescope. In *Proceedings of the Advanced Maui Optical and Space Surveillance Technologies Conference* (pp. 450–463). Maui, Hawaii.
- Payne, T. E. [Tamara E.], Lucas, K., Chaudhary, A., Mutschler, S., Dao, P., & Murray-Krezan, J. (2013, September 10). A Derivation of the Analytical Relationship between the Projected Albedo-Area Product of a Space Object and its Aggregate Photometric Measurements. In R. S. (Ed.), *Proceedings of the Advanced Maui Optical and Space Surveillance Technologies Conference* (E33). Maui, Hawaii.
- Payne, T. E. [Tamara E.] & Shine, N. T. (2013). *Analytical Analysis of Photometry of Three-axis Stabilized Geosynchronous Satellites*. Applied Optimization Inc. Retrieved from <http://aero.tamu.edu/sites/default/files/images/Alfriend/S4.2%20PaynePaper.pdf>
- Pickering, K. A. (2002). The Southern Limits of the Ancient Star Catalog: The Commentary of Hipparchos. *DIO The International Journal of Scientific History*, 12, 3–27. Retrieved from <http://www.dioi.org/vols/wc0.pdf>
- Rask, J. D. (1982). *Modeling of Diffuse Photometric Signatures of Satellites for Space Object Identification* (Master's Thesis, Air Force Institute of Technology).
- Ricklefs, R. L. (2006, February 17). *Consolidated Laser Ranging Prediction Format*. ILRS Data Format and Procedures Working Group.
- Roh, D.-G., Choi, J., Jo, J. H., Yim, H.-S., Park, S.-Y., Park, M., ... Park, J.-H. (2015, December). *Journal of Astronomy and Space Sciences*, 32(4), 349–355. doi:10.5140/jass.2015.32.4.349
- Royce, R. F. (n.d.). A Better Method of Measuring Optical Performance. Retrieved 2016, from <http://www.rfroyce.com/standards.htm>
- Sacek, V. (2015). Notes on Amateur Telescope Optics. Retrieved from <http://www.telescope-optics.net/>
- Scargle, J. D. (1982, December). Studies in astronomical time series analysis. II - Statistical aspects of spectral analysis of unevenly spaced data. *ApJ*, 263, 835. doi:10.1086/160554
- Schmalzel, B. (2013). *The Feasibility and Application of Observing Small LEO Satellites with Amateur Telescopes* (Master's thesis, California Polytechnic State University). Retrieved from <http://digitalcommons.calpoly.edu/theses/1068/>
- Scott, R. L. & Wallace, B. (2008). Satellite characterization using small aperture instruments at DRDC Ottawa. In *Proceedings of the Advanced Maui Optical and Space*

- Surveillance Technologies Conference* (pp. 337–347). Maui, Hawaii. Retrieved from <http://www.amostech.com/technicalpapers/2008/nroc/scottwallace.pdf>
- Shell, J. R. (2010, September 14). Optimizing orbital debris monitoring with optical telescopes. In S. Ryan (Ed.), *Proceedings of the Advanced Maui Optical and Space Surveillance Technologies Conference* (E42). Maui, Hawaii.
- Snyder, G., Hurst, S., Grafinger, A., & Halsey, H. (1965). Satellite laser ranging experiment. *Proceedings of the IEEE*, 53(3), 298–299. doi:10.1109/proc.1965.3691
- Stetson, P. B. (1987, March). DAOPHOT - A computer program for crowded-field stellar photometry. *PASP*, 99, 191. doi:10.1086/131977
- Swartwout, M. (2013). The first one hundred cubesats: A statistical look. *Journal of Small Satellites*, 2(2), 213–233.
- Swartwout, M. (2014). *The First 272 CubeSats*. NASA Goddard Space Flight Center.
- Swartwout, M. (2016). CubeSat Database. Retrieved from <https://sites.google.com/a/slu.edu/swartwout/home/cubesat-database>
- Sydney, P. F., Africano, J. L., Fredericks, A., Hamada, K. M., Hoo, V. S., Nishimoto, D. L., ... Bisque, M. (2000, October). Raven automated small telescope systems. In J. W. Bilbro, J. B. Breckinridge, R. A. Carreras, S. R. Czyzak, M. J. Eckart, R. D. Fiete, & P. S. Idell (Eds.), *Imaging Technology and Telescopes*. SPIE-Intl Soc Optical Eng. doi:10.1117/12.405780
- The CubeSat Program. (2014). *Poly Picosatellite Orbital Deployer Mk. III Rev. E User Guide*. California Polytechnic State University.
- UCS. (2015). UCS Satellite Database. Retrieved from <http://www.ucsusa.org/nuclear-weapons/space-weapons/satellite-database>
- USAFA Center for Space Situational Awareness Research. (2013). Falcon Telescope Network Slideshow: Otero Junior College Falcon Telescope. Retrieved from <http://www.usafa.edu/df/dfe/dfer/centers/acssar/FTNSlideshow/Falcon%20Telescope%20Network/index.html>
- USSTRATCOM. (2014). USSTRATCOM Space Control and Space Surveillance. Retrieved from <http://www.stratcom.mil/f11>
- Vallado, D., Crawford, P., Hujasak, R., & Kelso, T. (2006, August). Revisiting Spacetrack Report #3. In *AIAA/AAS Astrodynamics Specialist Conference and Exhibit*. American Institute of Aeronautics and Astronautics (AIAA). doi:10.2514/6.2006-6753
- Vanderplas, J., Connolly, A., Ivezić, Ž., & Gray, A. (2012, October). Introduction to astroML: Machine learning for astrophysics. In *Conference on Intelligent Data Understanding (CIDU)* (pp. 47–54). doi:10.1109/CIDU.2012.6382200

- Veis, G. (1963, August). Optical tracking of artificial satellites. *Space Science Reviews*, 2(2), 250–296. doi:10.1007/bf00216781
- Wellems, D. & Bowers, D. (2007, September 12). Laboratory imaging of satellites and orbital appearance estimation. In S. Ryan (Ed.), *Proceedings of the Advanced Maui Optical and Space Surveillance Technologies Conference* (E61). Maui, Hawaii. Retrieved from <http://www.amostech.com/TechnicalPapers/2007/Imaging/Wellems.pdf>
- Whipple, F. L. & Hynek, J. A. (1958). Optical and Visual Tracking of Artificial Satellites. In *VIIIth International Astronautical Congress Barcelona 1957* (pp. 429–435). Springer Science + Business Media. doi:10.1007/978-3-662-39990-3\_34
- Zhao, C. (2009). *Towards Efficient Surveillance Using Visual Tracking and Camera Control* (Doctoral dissertation, Christ Church College, University of Oxford).
- Zirker, J., Whipple, F., & Davis, R. (1956). *Time available for the optical observation of an earth satellite*. In J. A. V. Allen (Ed.), *Scientific Uses of Earth Satellites* (pp. 23–28). Chapman and Hall Limited.